NOTE TO USERS

PHOTOEMISSION APPLIED TO ION MOBILITY SPECTROMETRY TO DETECT EXPLOSIVES AT AMBIENT PRESSURE AND ROOM TEMPERATURE

A Dissertation
Submitted to the Graduate Faculty
of the
North Dakota State University
of Agriculture and Applied Science

By

Feng Hong

In Partial Fulfillment of the Requirements
for the Degree of
DOCTOR OF PHILOSOPHY

Major Department:
Physics

May 2004

Fargo, North Dakota

North Dakota State University
Graduate School

Title

Photoemission Applied Ion Mobility Spectrometry to Detect Explosives at Ambient Pressure and Room Temperature

By

Feng Hong

The Supervisory Committee certifies that this ***disquisition*** complies with North Dakota State University's regulations and meets the accepted standards for the degree of

DOCTOR OF PHILOSOPHY

SUPERVISORY COMMITTEE:

Owen T. Svenson
Chair

Charles A. Lawrence

Cela Denton

David C. Rogers

Approved by Department Chair:

6/21/04
Date

Charles A. Lawrence
Signature

ABSTRACT

Hong, Feng, Ph.D., Department of Physics, College of Science and Mathematics, North Dakota State University, May 2004. Photoemission Applied to Ion Mobility Spectrometry to Detect Explosives at Ambient Pressure and Room Temperature. Major Professor: Dr. Orven F. Swenson.

This work demonstrated a photoemissive ionization source to be a stable, sensitive, selective, and reliable ionization source for ion mobility spectrometry (IMS) detection of electronegative vapor samples, such as explosives at ambient pressure and room temperature in air. One photon-like photoemission from a 20-nm thick gold film sputter-coating on a fused silica prism was found when a 266 nm laser beam irradiated the gold film. The photoemitted electron signals were enhanced about five times for angles of incidence beyond the critical angle. This enhancement was not due to resonant excitation of the surface plasmons because 266 nm light cannot satisfy the resonant condition of surface plasmons. Furthermore, beyond the critical angle, the 266 nm light cannot be transmitted into the ionization region of the IMS because of total internal reflection. Thus, this feature removes the possibility of photo-dissociative fragmentation of the analyte molecules. This feature is very important to improve detection limits of IMS by limiting fragmentation of ions.

As demonstrated in this study, IMS equipped with a photoemissive ionization source had the capability to rapidly detect gaseous-phase nitro-organic and chlorinated compounds, such as 2,4-DNT; 2,6-DNT; p-nitrotoluene; trichloroethylene (TCE); and methylene chloride, at atmospheric pressure and room temperature in air. While these studies were limited to three nitro-organic molecules, the analytical principles

demonstrated in this study are expected to be applicable to a wide range of electronegative compounds, in particular common explosives such as TNT and RDX.

Theoretical and experimental results indicated that 632.8 nm and 532 nm light excites surface plasmons resonantly for gold films' thicknesses in the range from 20 nm to 50 nm. Moreover, we have found that 266 nm light was unable to excite surface plasmons.

The surface plasmon resonance (SPR) was anticipated to enhance two photoemissions from the gold films; however, the 532 nm Nd:YAG laser was used to illuminate the 20-nm thick gold film, and no photoelectron signal was detected with either s- or p-polarized laser. Although the incidence angle for 532 nm was adjusted to resonantly excite the surface plasmons at the air-gold interface, no signal was observed.

ACKNOWLEDGMENTS

I would like to thank my adviser, Orven F. Swenson, for his guidance throughout my six years at North Dakota State University. He has prepared me well for a career as a physics academic and has worked hard to promote my work. I was greatly influenced by him; he supervised both my master's and Ph.D. work. Dr. Swenson's ability to rapidly assess the worth of ideas, insightful comments and assistance on theoretical as well as experimental matters, and technical issues are amazing. I would spend a week or two on an approach to a problem, and Dr. Swenson could understand it and tell me (correctly) that it would not work in about a minute.

I would like to thank Jeremy Brodersen and Nathan Schoenack. Together we have spent many enjoyable hours at NDSU talking about our research. Jeremy, in particular, has always been very quick to understand my ideas about what I was doing for my Ph.D. degree. He has helped me to figure out where my experimental setups were wrong and then attempted to fix them. I am also very grateful to Harlan Isensee, who is a research specialist in the Chemistry Department, for his invaluable help with design and realization of the equipment.

In particular, I would like to thank David Rogers, Charles Sawicki, and Allan Denton for being on my defense committee and for their very useful and helpful feedback. They were all interested in what I was doing and improved the quality of what I eventually wrote. They gave very detailed comments on all aspects of the dissertation and made sure that I did a good job understanding what I have done for my research.

It is not possible to summarize Yimei Zhu, my wife, and her influence on me in one paragraph, but I will try. Her love, intelligence, honesty, goodness, healthiness, humor, taste, liveliness, and beauty have given me something for which to live. She is the most balanced and well-adjusted person I have ever known. The fact of her existence is a continual miracle to me. She has supported me in hundreds of ways throughout the development and writing of this dissertation.

My parents are also very special people. They have given their unconditional support, knowing that doing so contributed greatly to my absence these last six years. They were strong enough to let me go easily, to believe in me, and to let slip away all those years during which we could have been geographically closer and undoubtedly driving each other crazy.

Finally, I have made many friends along the way. They have helped me, one way or another, in my struggle to complete a Ph.D. Many thanks to Patty Hartsoch and all professors as well as graduate students in the Physics Department at North Dakota State University. Special thanks are also given to my host family, Paul Connelley and Rosalinda Connelley, for invaluable advice and help in a new culture, making me so welcome during the time of my stay in Stanley.

TABLE OF CONTENTS

LIST OF TABLES

LIST OF FIGURES

CHAPTER 1

INTRODUCTION

This work examines photoemissive ionization as a stable, sensitive, selective, and reliable ionization source in ion mobility spectrometry. Results of the detection of trace amounts of chlorinated molecules and nitro-organics (a family of explosives) at room temperature in ambient air via electron attachment ionization are presented. The results presented demonstrate that an ion mobility spectrometer (IMS) equipped with the photoemissive ionization source (PE-IMS) developed during this research provides a unique feature. The ultraviolet (UV) light incident at an angle of incidence greater than the critical angle not only increases the sensitivity of the IMS five times over normally incident light, but no light is transmitted through the IMS drift tube. Since UV light photo-dissociates explosive molecules,[1-5] this characteristic, no light transmitted through the drift tube, is crucial in detecting explosives.

This work is organized as follows. First, the background of Ion Mobility Spectrometry will be briefly introduced, and the different ionization approaches used in IMS will be presented in Chapter 1. Next, the typical methods of desorbing samples and then ionizing sample vapors will be discussed. Subsequently, photoemission in air will be discussed, followed by the history of PE-IMS. In Chapter 2, the deposition of photoemissive films and measurement of the thickness of gold thin films will be introduced. In Chapter 3, we will review the theoretical background in the bulk (volume) plasma in noble metals and study the surface plasmons at the semi-infinite interface between the gold metal and the air. In addition, the incident angle of light at which the surface plasmons will be resonantly

excited will be calculated. In this work, we will primarily focus on carrying out the experiments by measuring electron emission from Au coating on a fused silica prism irradiated with the second or fourth harmonics of Nd:YAG as well as microchip lasers capable of delivering 5.0 ns pulses at the wavelengths of 532 nm and 266 nm. In Chapter 4, the atmospheric pressure photoemissive ion source will be employed in ion mobility spectrometry to detect a family of chlorinated samples and nitro-organic compounds, such as trichloroethylene (TCE), methylene chloride, 2, 4-dinitrotoluene (2, 4-DNT); 2, 6-dinitrotoluene (DNT); and p-nitrotoluene (p-MNT), at atmospheric pressure. In Chapter 5, the Conclusion and suggestions for Future Work will also be given.

1.1. Ion Mobility Spectrometry (IMS)

IMS is a standard analytical tool for detecting trace amounts of explosives.[6-14] Major advantages of IMS are its sensitivity in the ppb or pg range, its continuous real-time monitoring capability, its relatively low cost ($40,000-$60,000 for a typical ion mobility spectrometry detection system[15]), and its portability due to instrumental simplicity and easy automation.[16-17] If the application requires quantifying or identifying very low concentrations, IMS is likely the most effective technique.

The basic idea behind IMS is that a sample is vaporized into the gas phase and directly introduced to the ionization chamber by a carrier gas, dry air, or nitrogen gas. Figure 1.1 shows that the typical IMS consists of a drift tube in which an electrical field is created in one direction and a drift gas flows counter to the electric field. An ionization source is depicted on the left side of Figure 1.1. In traditional IMS systems, this ionization source is a radioactive (^{63}Ni) source[18] that produces both negative and positive ions from the air or nitrogen drift gas. These ions react with dopant gases, such as ammonia, acetone,

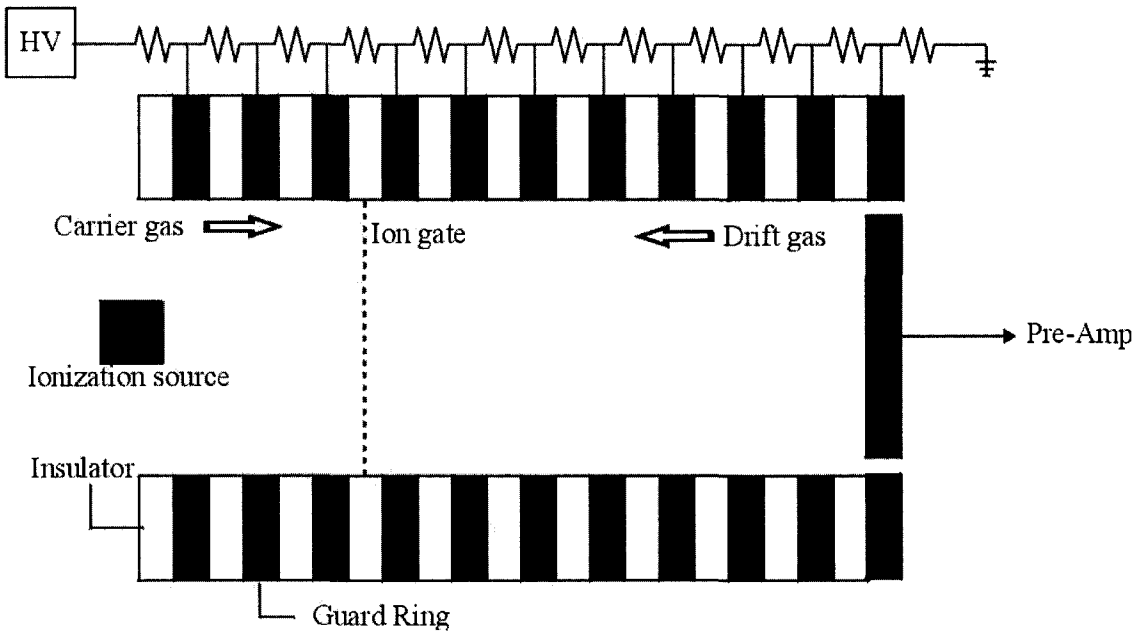

Figure 1.1. Schematic diagram of ion mobility spectrometry (IMS).

methylene chloride, etc.,[7-9,19-23] that are added to the carrier gas to produce reactant ions.[19] In the presence of a mixture of compounds, these reactant ions undergo ion-molecule reactions to produce product ions. Figure 1.1 also shows the ion gate with which a pulse of ions is permitted to pass through the gate into the ion separation region.

The term ion mobility spectrometry (IMS) refers to the method of characterizing chemical substances using gas-phase mobilities of ions in weak electric fields. Normally, mobilities are determined from the time of drift for ions across a fixed length in a constant electric field where time is referenced to the initial injection of ions from the source region to the drift region. Ion mobilities are characteristic of substances and can provide a rapid means for detecting and identifying vapors. Once ions traverse the drift tube, they induce current flow from the collector, producing a time-dependent current signal known as the ion mobility spectrum.

1.2. Ion Sources for Ion Mobility Spectrometry (IMS)

After introduction of the sample vapor into the IMS, the neutral molecules in the sample are ionized. This ionization occurs in the gas phase by electron- or proton-transfer from reactant ions available in the ionization chamber to sample molecules.[23] The ionization process plays a key role in IMS sensitivity and selectivity because the mobility spectrum is dependent upon the method for creating ions. For example, photodischarge lamps add selectivity to IMS through ionization of only analytes with ionization energies lower than the photon energy of the lamp, and a photoemissive ionization source has selectivity via only electronegative analytes.

Ionization sources that are known today as suitable for IMS include radioactive sources (alpha and beta radiation), UV lamps,[24,25] lasers,[26] different kinds of discharges (e.g.,

corona or partial discharges[27,28]), photoionization,[29] and electrospray ionization.[30] However, radioactive nickel (^{63}Ni) has been the favored ionization source in IMS due to advantages including output stability, mechanical integrity, noiseless operation, and lack of external power requirements. With a ^{63}Ni - source, the ionization process starts with the emission of high-energy ß-particles (high-energy electrons). One electron reacts with a vapor sample to form unstable cations and energetic secondary electrons. The cations initiate a sequence of ion-molecule reactions while the secondary electrons generate additional ion pairs in the gas as long as energetically possible. The cycle of electron impact ionization allows a single β-particle to produce up to several hundred pairs of ions in the gas.

Photoionization[29] has been used in IMS to extract single electrons from molecules to generate a pair of positive and negative ions. Photoionization sources include gas discharge lamps and lasers. If the energy of the photons is greater than the ionization energy of analyte molecules, the analyte molecules are excited by absorbing a single photon or multiple photons, and then are ionized by releasing single electrons. Conversely, a photoemissive ionization source[24] creates product ions by means of electron attachment.

With the exception of photoemissive sources, these sources are bipolar, generating reservoirs of positive and negative reactant ions. However, photoemissive electron sources are unipolar, so only negative reactant ions are produced through direct, low-energy electron attachment by analyte molecules.

1.3. Standard Ways of Detecting Explosives and Disadvantages of Using These Approaches

The ionization source and the method to vaporize a liquid or solid explosive sample in a conventional IMS are radioactive ^{63}Ni and thermal vaporization, respectively. Although

such ionization sources and thermal desorption have been used successfully, there are some real problems associated with them.

1.3.1. Thermal Desorption

Thermal desorption is used to vaporize a solid or liquid sample into gas-phase molecules in ion mobility spectrometry. Typically, the desorption temperature is from 200 to 300° C.[31] The main disadvantage of thermal desorption is that nitro-organic explosives are thermally labile compounds; that is, they can be fragmented at the elevated temperature. Additionally, the desorber vaporizes a solid or liquid sample continuously, so the density of molecules is not high. The continuity of the sample desorption may affect the sensitivity of detection.

1.3.2. Radioactive Ionization Source

In a conventional ion mobility spectrometer, ionization is produced using a ^{63}Ni-radioactive foil. The radioactive foil emits β-particles (high-energy electrons up to 67 keV) continuously and ionizes almost every molecule in the reaction region. Ionized molecules are introduced into the drift region (electric field), and due to the electric field, they drift continuously; that is, the current created at the collector is constant. It is obvious that identification of species is impossible; consequently, an ion gate (shutter grid) is placed in front of the drift region to generate pulsed ions. When the grid is "on," the ions are attracted to the grid and lose their charge. For a brief amount of time when the grid is "off," the ions are transmitted into the drift region. This process results in a pulse of ions, but, at the same time, there is a great loss of ions passing through the shutter grid. (Roughly 80% of ions are lost.) There are several disadvantages of using ^{63}Ni as the ionization source in IMS:

(a) Relatively lower sensitivity: A loss of product ions resulting from the shutter grid (roughly 80% of the ions lost) affects the sensitivity. Besides production ions lost, since ^{63}Ni generates pairs of positive and negative ions, they can recombine into neutrals by collisions.

(b) Relatively lower selectivity: Ideally, we do not want to ionize molecules that we are not interested in detecting. Any additional ions must have enough difference in their ion mobilities from the target molecular ions so that the drift tube can separate them from target molecules; however, ^{63}Ni can ionize every molecule in a gas mixture. The ionization of every molecule increases the possibility of generating some ion that has an ion mobility close enough so that the drift tube cannot separate ionized molecules, resulting in overlap in the IMS spectrum. Therefore, the target molecules might not be identified.

(c) The danger of handling radioactive materials.

(d) Nickel is oxidized in the atmosphere, so a ^{63}Ni source must be periodically wipe-tested following Nuclear Regulatory Commission (NRC) procedures. Furthermore, manufacturing, transporting, storing, operating, and disposing hardware containing a ^{63}Ni radioactive source must follow the NRC regulation.[14,18]

Because of these disadvantages of the conventional ionization source (^{63}Ni), a nonradioactive ionization source for IMS that can replace the ^{63}Ni ionization source is highly desirable. Successful examples of nonradioactive sources for IMS using thermionic ionization,[32] photoionization,[29] laser ionization,[26] coronaspray ionization,[27,28] and electrospray ionization[30] have been reported for a variety of applications. This dissertation will present the detection of trace analytes at ambient pressure in air by coupling a

photoemissive ionization (PE) source with ion mobility spectrometry (IMS). A PE-IMS system has unique features, compared to conventional radioactive ionization sources, as follows:

(a) The photoemissive source generates only negative ions (including low-energy free electrons), so it eliminates the possible loss mechanism involving both positive-negative ions and positive ion-electron recombination giving rise to a decrease of IMS sensitivity.

(b) It removes the danger of handling radioactive materials.

(c) The initial electron concentration can be controlled, in principle, over a wide range simply by changing the incident light intensity.

(d) When a pulsed light source is used, it offers the attractive design option of eliminating an ion gate (shutter grid) at the entrance to the drift tube that causes the loss of roughly 80% of the ions.[33]

The study of PE-IMS includes generation of free electrons by ultraviolet back-side illumination of a thin gold film deposited on a fused silica window and detection of chloride and nitro-organic ions created by low-energy electron attachment. In addition, the number of electrons is optimized by means of changing the incident angle of the ultraviolet light as well as the thickness of the thin gold films. Furthermore, the capability of the PE source is examined as a stable, selective, sensitive, and reliable ionization source in an IMS system.

1.4. Photoemission

Photoemission, or photoelectric emission, is both a surface and a volume effect of metals. The process of photoemission from metals is approximated as a sequence of three

steps: 1) absorption of photons by thermal electrons in the metal, 2) migration of excited electrons to the surface of the metal, and 3) escape of electrons from the metal surface. The energy barrier to electron emission from a metal surface is the work function of that metal. This section begins with an overview of the photoelectric effect.

1.4.1. Photoelectric Effect History

The photoelectric effect was discovered in 1887 by a German physicist, Heinrich Rudolf Hertz,[34] who observed that ultraviolet light changed the lowest voltage at which sparking took place between metal electrodes. Within a few years after the first discovery of the photoelectric effect, a number of phenomena were observed by Hallwachs, Elster and Geitel, P. Lenard, J. J. Thompson, and others.[34] Their observations indicated that the electrical charges were liberated from the metal surface when it was illuminated; that the yield was greater for shorter wavelengths, particularly the ultraviolet (UV); and that the presence of gases was found to have marked effects with respect to making a surface more or less sensitive to radiation. It was further discovered that the photoelectric yield is directly proportional to the intensity of light. In 1902, it was proven that the maximum kinetic energy of an electron in the photoelectric effect is independent of the intensity of the light ray and depends on its frequency. The search for an explanation led, in 1905, to Albert Einstein's fundamental theory[34] that light can be regarded alternatively as composed of discrete particles (photons). The energy of emission of photoelectrons follows the Einstein relationship

$$h\nu = W_a + \frac{1}{2}mv^2_{max} = W_a + K_{max}, \qquad (2.1)$$

where K_{max} is the maximum kinetic energy of the photoelectrons, h is Planck's constant, ν is the frequency, and W_a is the work function.

1.4.2. Photoelectric Effect in Air

The photoelectric effect has been extensively studied in a vacuum due to the chemical phenomenon of oxidation.[35] It has been discovered that the work function at the surface of a metal is strongly dependent on the binding energy of the electron to the solid. This binding energy is much different for an electron on a pure metal surface than for a metal oxide.[35] In order to obtain reproducible results for the work function of a metal, the experiment must be carried out in an ultrahigh vacuum so that the surface qualities do not change with time.

As far as the effect on the metal itself, atmospheric pressure has no significant impact on the electronic structure of the metal, so in that sense, the work function would not be changed in air except for the case in which a pure metal is oxidized, resulting in the change of the work function of the metal. In addition, molecules near the surface of the plate may present an additional barrier to the departing electron and, thus, increase the work function by a small amount.[35]

Studying the photoelectric effect in air instead of a vacuum is an extremely complicated issue.[35] Besides the fact that metal's oxidization in air affects the photoelectric effect, the photoemission is also influenced by the adsorption of water vapor and other adsorbates to the metal oxide. The pronounced effect of surface impurities and gas layers on photoelectric emission was known even to the earliest investigators.[36–39] The effect of certain gases on the work function of metals was established early in various thermionic emission studies that have been well summarized by Dushman.[40] Kingdon,[41] for instance,

showed that whereas the work function of clean tungsten was 4.50 eV, an oxygen layer changed the work function to 9.2 eV. Hales[42] work on mercury showed that none of H_2, N_2, He, and Ar had any effect on its threshold, while O_2 and dry air both decreased the photoelectric yield and increased the threshold frequency.

In later work, many investigators have also demonstrated the strong influence of adsorbed or dissolved gases on photoemission and work function.[43] Kei Inumaru and his group[44] investigated photoemission from the thin gold films in ambient atmosphere with the presence of different types of organic vapors using 254-nm ultraviolet light. They found that cyclohexene resulted in a large increase of photoelectron current with oxygen molecules in air while acetone reduced the photoelectron current to near zero. In addition, they observed that ethanol and water had an increase of photoelectron current with the presence or absence of oxygen molecules. It is possible to study the changes in electronic structure of surfaces caused by the interaction of water vapor and metal ions.[45] However, such calculations have not been able to model the important details of metal oxide-water reactions.

1.5. Photoemissive Ionization Source Coupled with Ion Mobility Spectrometry

The main objective of this work is to study the ability of the photoemissive ionization source to serve as a stable, selective, sensitive, and reliable ionization source in ion mobility spectrometry. Photoemission results from the absorption of photons by thermal electrons in a metal. If the electrons attain energies greater than the work function of that metal, they escape from the metal. The photoemissive ionization source produces (low-energy) electrons (several eV) photoelectrically emitted by the surface of a metal at

ambient pressure in air. Since the emitted low-energy electrons collide with a very large number of molecules in air, the free electrons produced by PE are rapidly thermalized at atmospheric pressure. [46] These thermal electrons attach to electronegative species, such as the oxygen molecule, nitro-based compounds (a family of explosives), and so on, very near to the surface of the metal to form negative ions.

Although photoemissive sources have existed for over a century for the measurement of the electron capture rate used in understanding electron-molecule interactions in the gas phase, only one ion mobility spectrometer equipped with a photoemissive source has been reported. [24,25] Simmonds and his group [24,25] coupled a photoemissive ionization source to an ion mobility spectrometry for trace analysis at atmospheric pressure. No follow-up work has been published, and no data were presented for the two most obvious applications, detection of chlorinated solvents and nitro-organic compounds (i.e., explosives).

The basic idea behind Simmonds' experiment was that a pulsed UV light generated by a xenon flash-lamp was used as the illumination source at pulse repetition rates of 50 Hz and 30 Hz. A drift gas, either air or nitrogen gas, was maintained through the inlet in the collector region. When the pulsed UV flash-lamp was applied to a thin gold film with a 4.5 eV work function, electrons escaped from the gold foil and were attached to target molecules, such as benzoylacetone, acetylacetone, and oxygen molecules in air, to produce negative ions. Simmonds' group experimental results showed that the separation of benzoylacetone and acetylacetone ions from oxygen ions was very good.

In addition, Simmonds and his group [24,25] investigated how the pulse width affected the resolution of ion mobility spectra for a 3.7-cm drift tube, photoemission efficiency as a function of wavelength, and the effect of the photoemissive window diameter on the

detector's performance. They also compared the performance of the detector with the photoemission source to conventional designs employing radioactive ionization sources. Their work suggested that the detector with the photoemission source had a higher sensitivity than that employing a radioactive ionization source and demonstrated that photoemission can be exploited as a viable ionization technique for use in ion mobility detectors.

CHAPTER 2

EXPERIMENTAL PHOTOEMISSION

2.1. Coating a Metal on a Fused Silica Substrate

2.1.1. Preparation of Surface

Cleaning surfaces of substrates is a very important step to achieve strong bonds to the fused silica substrates. Fused silica substrates used for this work were cleaned by first washing in 2% diluted Mico-90 to remove the insoluble polishing compounds. The substrates were rinsed in deionized water, and then subsequently washed in alcohol and acetone to remove surface contamination and to dissolve water from the surface. Finally, the substrates were blown dry with dry air or nitrogen gas. Because recontamination occurred from air exposure in the form of water vapor, hydrocarbons, and other atmospheric pollutants, a final cleaning was provided before coating began; that is, the surfaces of the fused silica windows were re-cleaned by using the acetone and alcohol just before those windows were placed in the vacuum chamber of the SCD 030 sputtering coater.

2.1.2. Coating Metals on Fused Silica Substrates by the Means of Sputtering Coating[47]

The basic idea of sputter coating is that a glow discharge is produced in argon gas at a pressure of about 0.05 mbar between an anode (specimen-substrate) and cathode (target). The argon molecules become positive ions because of the glow discharge. Under the influence of an electric field, the positive argon ions are accelerated and move toward the cathode (target such as gold), knocking metal atoms off the target as they hit it. The metal atoms undergo multiple collisions with molecules in the chamber as they approach the

anode (specimen), resulting in a "cloud" of metal atoms that are deposited on the surfaces in the chamber. The homogeneity of this deposit is particularly high at the anode on which the specimen is placed.

The sputter coater used, SCD 030, was located in the Northern Crop Science Laboratory at North Dakota State University. The vacuum chamber was evacuated to about 0.049 mbar. Flushing the chamber several times with argon made it easier to pump out undesired gases, particularly water vapor. After this flushing process, the pressure of argon gas was brought up to about 0.05 mbar. The sputtering current, the distance between the target and sample, and the sputtering time were chosen as 90 mA; 50 mm; and varying times, for instance, 10 seconds, 20 seconds, 30 seconds, etc. Those three parameters determined the fine-grained structure and thickness of the sputtered film.

2.1.2.1. Uniformity of the Gold Coatings

The uniformity of film thickness was determined from absorbance measurements as a function of position in increments of 0.2 mm both horizontally and vertically. In Figure 2.1, the transmittance through thin films of two different thicknesses can be seen. From Figure 2.1, it is clear that the intensity of laser light transmitted through these thin gold films at a normal incident angle is weakly dependent on the scanning position; therefore, the thickness of the thin films is sufficiently uniform for our application. However, Figure 2.2 shows that the transmittance of films that varies with the scanning position along both the horizontal and vertical directions is not satisfactory.

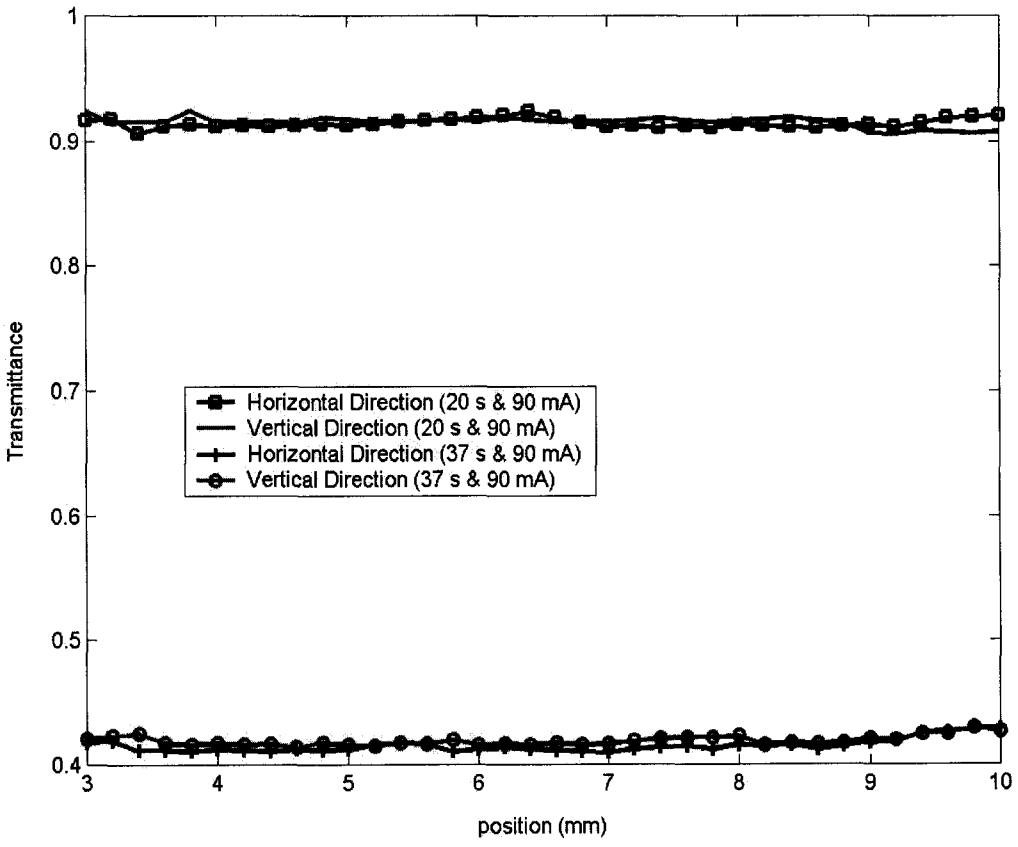

Figure 2.1. Transmittance through thin gold films measured at 0.2 mm increments.

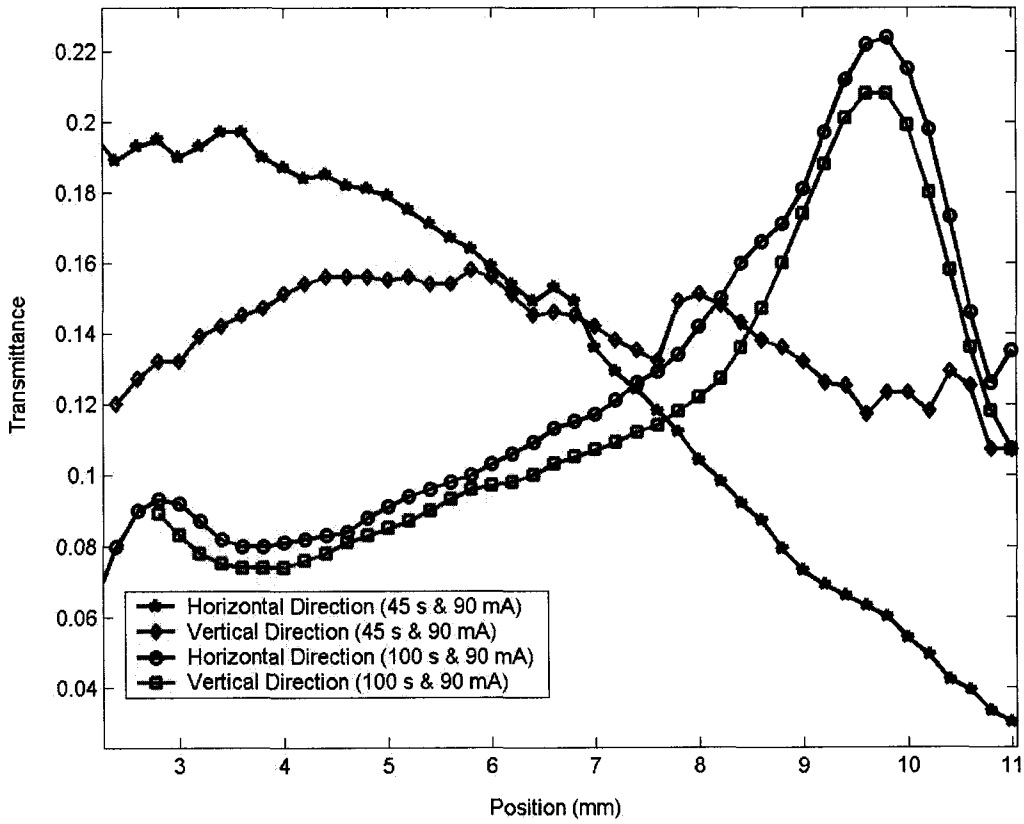

Figure 2.2. Transmittance through thin gold films measured at 0.2 mm increments showing large variations in thickness.

2.1.2.2. Adhesion Problem

Some coating materials require a precursor layer to promote bonding to a substrate. Inert metals, gold being an extreme example, do not form strong bonds with substrate materials and, therefore, present adhesion problems. [48-50] The well-known method of depositing a precursor layer promotes adhesion for difficult cases. A thin layer of chromium, tin oxide, bismuth oxide, and magnesium fluoride can promote adhesion. The metals form oxides that bond to both the substrate surface and to the gold layer. The adhesion layer can have a thickness between about 2 nm and 30 nm, depending on whether transmission or other properties are affected. Attempts to sputter precursor coatings of chromium or titanium were unsuccessful because the SCD 030 sputter coater used for this study could not pump the vacuum chamber down to 0.001 mbar (7.5×10^{-4} torr) that was suggested by the manufacturer for this coating. However, the gold coating adhesion to the fused silica substrate was adequate without a precursor layer for the measurements made.

2.2. Film-Thickness Measurement by Michelson Interferometer

Various methods are available for measuring the thickness of thin films. [51] In this section, we describe a laser interferometer and report the results of measurements of thin film thickness.

2.2.1. Principle of the Method

Fringes of equal thickness offer a sensitive optical means for measuring thin films. Suppose that the film to be measured has thickness d on the fused silica substrate (circular flat window). The He-Ne laser beam passes through a right-angle beam-splitting prism that reflects one beam to a flat mirror, M, and transmits the other to the film surface shown in Figure 2.3. After reflections from the mirror and substrate, the two beams are combined by

the beam splitter into the CCD camera to measure the interference. When the mirror, M, and the film surface are not precisely parallel, the usual Fizeau fringes due to the wedge are seen through the CCD camera as shown in Figure 2.4. These patterns are generated by the substrate without and with film. Two patterns of interference are taken into account for the measurement of film thickness.

Figure 2.4 shows the patterns of these two fringes. For normal incidence, bright fringes satisfy

$$2nd = \Delta m\lambda \quad , \qquad (2.2)$$

where n is the index of refraction of air ($n = 1$), d is the film thickness, λ is the wavelength of light, and Δm represents the difference in the order of two successive fringes. Increasing the thickness by $\lambda/2$, for example, changes the order of any fringe by $\Delta m = 1$; that is, the fringe pattern translates by one whole fringe. For a fringe shift of magnitude Δx, shown in Figure 2.4, the change in m is given by $\Delta m = \Delta x/x$, resulting in

$$d = \left(\frac{\Delta x}{x}\right)\left(\frac{\lambda}{2}\right) \quad . \qquad (2.3)$$

Both the fringe spacing, x, and the fringe shift, Δx, are measured with digital images taken by the CCD camera and analyzed using Matlab software.

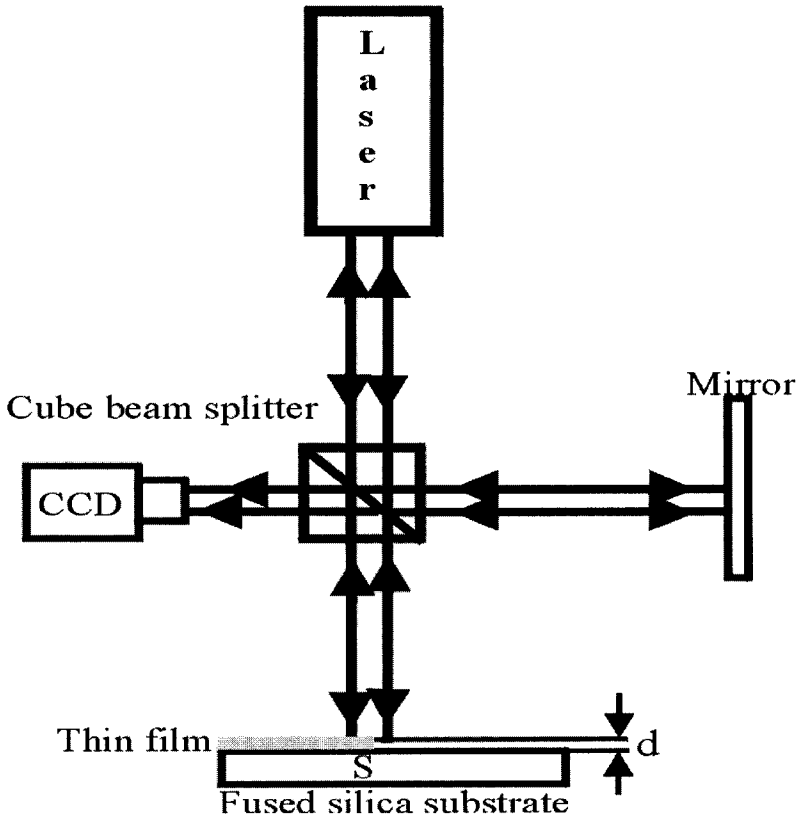

Figure 2.3. A schematic of film-thickness measurement. Interference fringes generated by light reflected from the film surface and substrate allow a determination of the film thickness, d.

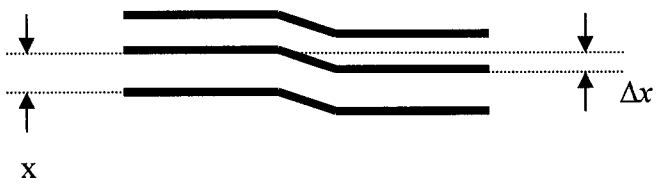

Figure 2.4. Sketch of interference fringes produced by the light reflected from the film surface and substrate.

2.2.2. Measurement Setup

A beam-expanded helium-neon (JDS Uniphase, Model 1100) laser with a wavelength of 632.8 nm was used as the source of radiation. The optical system applied to measure the thickness of the films used a Michelson interferometer with even arms shown in Figure 2.5. In the interferometer, one of the two mirrors was substituted by a fused silica plate, with a thin film deposited on half the surface of the substrate, in such a way that a step was formed. Because the fused silica substrate without a gold coating had poor reflection, and thus the fringes produced by the uncoated surface of the substrate were not clear, the entire surface of the flat fused silica substrate was coated with a thick background coating, making the plate work as a mirror with a step. This step was formed by coating a thin gold film of interest on the fused silica substrate masked by a standard microscope slide. Figures 2.6 and 2.7 show images for interference patterns of two different films. Film thicknesses were calculated from the fringe shifts as observed in Figure 2.6.

2.2.3. Results

Table 2.1 shows data obtained from 11 thin gold film samples, where a denotes the shift between interference fringes and b represents the fringe width, as shown in Figure 2.6. A Matlab program was used to measure the shift between interference fringes. Using Eq. 2.3 for the thickness:

$$d = \left(\frac{b}{a}\right)\left(\frac{\lambda}{2}\right) , \qquad (2.4)$$

where λ is the laser wavelength and d denotes the film thickness. The thickness of the layer can be measured as a function of distance as well as shift between fringes and wavelength. The calculated values determined using Eq. 2.4 are given in Table 2.1.

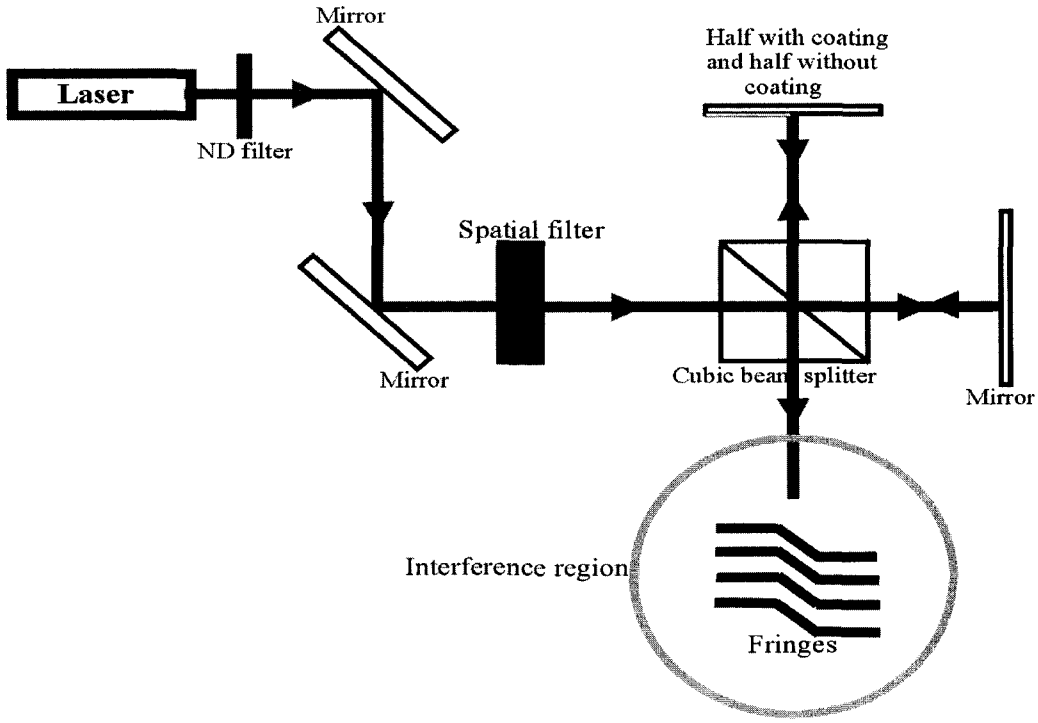

Figure 2.5. Experimental setup for measuring the thickness of a thin film.

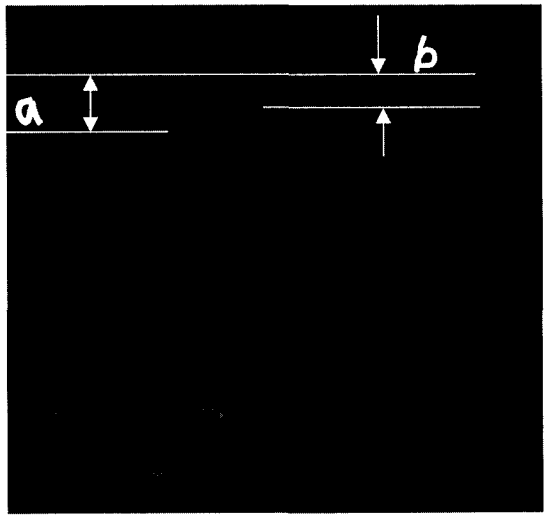

Figure 2.6. Digital image of the thin gold film with a sputtering time of 180 seconds, sputtering current of 90 mA, and target distance of 50 mm.

Table 2.1. Results of film-thickness measurement by Michelson Interferometer

Sputter time (s)	Sputter current (mA)	Pressure of argon gas (mbar)	a	b	Thickness (nm)
8	90	0.058	6.12	7.04	Undetermined
30	90	0.050	23.0	27.6	21.70
35	90	0.056	28.9	32.7	26.60
40	90	0.055	35.0	35.4	31.31
45	90	0.055	43.8	36.3	45.60
50	90	0.054	41.6	45.6	54.25
60	90	0.056	60.3	62.5	63.01
80	90	0.058	80.2	84.2	81.37
100	90	0.055	115.3	104.6	109.21

Accuracy limits of this method depend directly on the radiation source wavelength that is being used. For this wavelength (632.8 nm), differences between interference patterns are no longer evident for films with a small thickness compared with the wavelength of the source. For this work, the lowest resolution limit to analyze thin films is of the order of 20 nm. The thin film with sputtering time of 8 seconds has an undetermined thickness shown in the Table 2.1 since interference patterns appear as a continuum without a detectable step presence as shown in Figure 2.7. As long as there is a noticeable shift in the interference fringes, thicknesses of thin metallic layers can be measured. Figure 2.8 shows that the film thickness is linearly increasing with sputtering time. This experimental result is in agreement with plots in the instruction manual provided by Technotrade International, Inc.

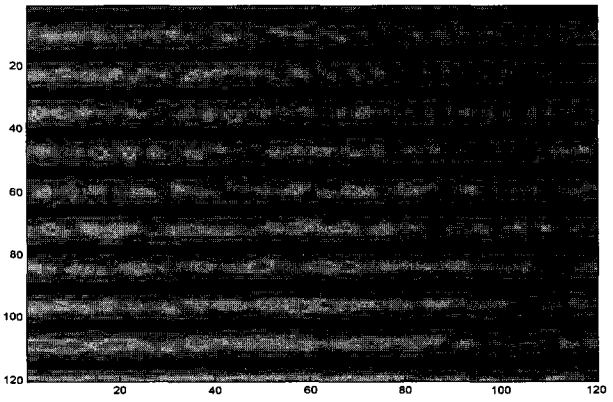

Figure 2.7. Digital image of the thin gold film with a sputtering time of 8 seconds, sputtering current of 90 mA, and target distance of 50 mm. The interference patterns appear as a continuum without a detectable step.

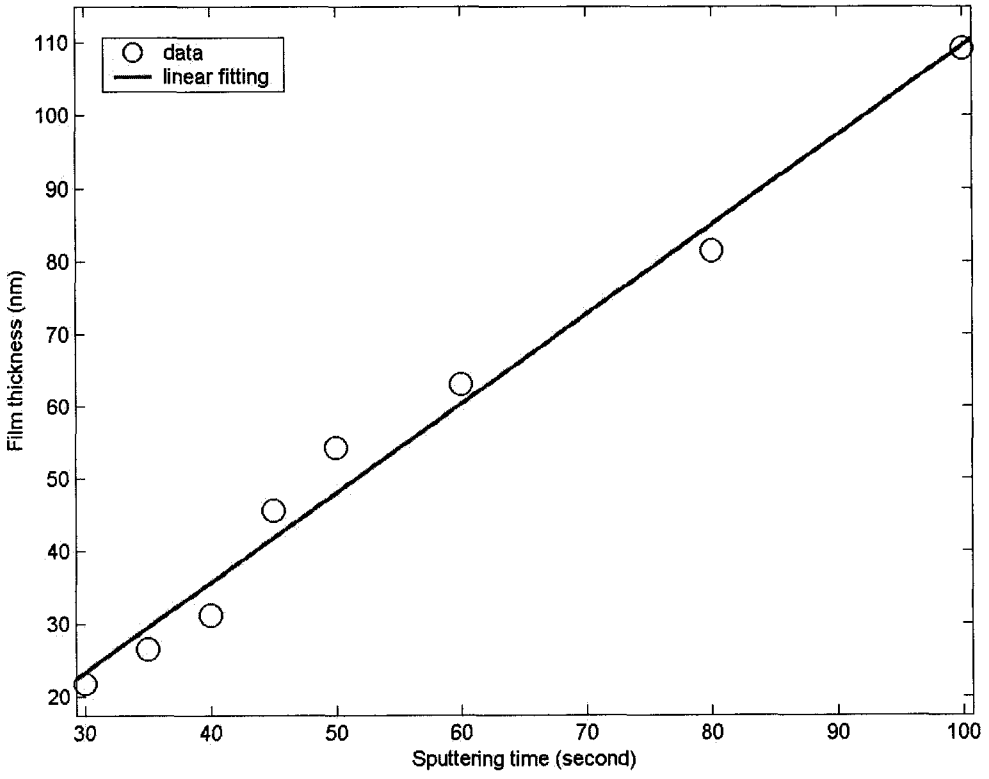

Figure 2.8. Experimental relationship between the sputtering time and the film thickness.

2.3. Optimization of Photoemission Yield

In this section, we investigate how the photoemissive yield, generated from a thin gold film by back-side illumination at the 266 nm wavelength at ambient pressure in air, changes with the thickness of thin gold films in order to obtain the optimum thickness of the thin gold film. P. Lukirsky and S. Prilezaev studied the distributions for Ag films on glass of 3 different thicknesses at the wavelength of 253.7 nm and found that the electron current increased with decreasing layer thickness in a vacuum.[52] The thicknesses of Ag films were 10 nm, 30 nm, and 40 nm thick. The electron current increasing with decreased layer thickness was confirmed by similar studies on thin films of Pt, Al, Cu, and Pd.

2.3.1. Oxygen Molecular Ion Formation by Electron Capture in Air

Electron capture (EC), or electron attachment,[53,54] is a process whereby a free electron is incorporated into an orbital of an atom or molecule. As the electrons approach thermal energy, EC can occur. Under EC conditions, there are three different mechanisms of ion formation:[55,56]

$$M + e^- \rightarrow M^{-*} , \qquad (2.5)$$

$$M + e^- \rightarrow (M-A)^- + A^* , \qquad (2.6)$$

$$M + e^- \rightarrow (M-B)^- + B^+ + e^- , \qquad (2.7)$$

where e^- represents an electron, M is a ground state molecule, M^{-*} is a molecular anion intermediate, and an asterisk indicates a possible increase in internal energy. Eq. 2.5 represents associative electron capture; Eq. 2.6 portrays dissociative electron capture to a neutral fragment and a stable negative ion fragment; and Eq. 2.7 represents ion-pair formation. Associative electron capture directly yields the negative molecular ion, M^{-*}, whereas fragment ions are formed by dissociative electron capture and ion-pair formation.

Molecular ions are generated by capturing electrons with kinetic energies of 0 eV to 2 eV while fragment ions are generated by capturing electrons from 0 eV to 15 eV. Ion-pair formation tends to occur when electron energies exceed 10 eV. [57]

Thermionic emission from a heated metal filament is the standard source of free electrons. However, those electrons usually are significantly above thermal energy and need to be decelerated for EC. Buffer gases such as methane, isobutane, or carbon dioxide serve well for that purpose, but others, such as nitrogen gas, have also been used. [58–60] In this experiment, the free electrons were created by photoemission from a thin gold film. These emitted photoelectrons had a large number of collisions with molecules in air, so the energies of these photoelectrons were low. Extensive investigation has shown that oxygen molecules in air then captured slow electrons associatively, generating molecular oxygen anion O_2^-. [61]

Due to high abundance, oxygen molecules attach nearly all photoemitted electrons within a relatively small volume of air near the surface of the photoemissive film. While the resulting swarm of molecular oxygen anions drifts toward the ion anode, the anions continuously participate in numerous reversible clustering reactions with neutral molecules available in the drift gas, including water, carbon dioxide, and oxygen. Thus, a mixed swarm of various clustered oxygen anion species arrives at the collector more or less as a single anion signature. The anions cannot be identified solely from drift time or mobility, but the drift time of the signature approximates that of some average anion species produced during ion drift. The temporal width of the signature, to some extent, represents complexity of clustering attained within the drift volume.

2.3.2. Experimental Setup for Measuring Photocurrent

The photoemissive ionization source was a gold-coated, 12.7-mm diameter, and 3.18-mm thick fused silica circular flat window (ESCO Products, Oak Ridge, NJ) mounted within a 4.8-cm o.d. oxygen-free high conductivity (OFHC) copper holder. The gold coating had a thickness of approximately 25 nm. The copper disk and the gold coating were in electrical contact by means of indium (Indium Corporation of America) soldering. The 2.75-inch stainless steel conflat flange 4-way cross housed the holder of the gold-coated fused silica window and the parallel copper collecting electrode. The flange held the PE source against the front end of the cell housing with the gold-coated side of the window facing inward as shown in Figure 2.9. The distance between the thin gold film and collecting electrode was about 26.0 mm. The combination of a Hamamatsu L4646 xenon flashlamp and two plano-convex fused silica lenses was used to deliver ultraviolet radiation onto the thin gold film for back-side illumination as shown in Figure 2.9. The flashlamp was usually operated at a 25-Hz repetition rate to generate pulses of approximately 1 μs in duration. The 2.5-cm focal length lens collimated the light from the lamp discharge with pulse energy of about 25 μJ (total flashlamp spectrum including visible light). The second lens was normally positioned such that the focused image lay near or within the photoemissive thin gold film. To reduce electrical noise, the flashlamp and power supply were housed within an aluminum shielding box. The current induced by ions traveling between the thin gold film and the collecting electrode was amplified by a home-built, low-noise, 10^8 V/A pre-amplifier and fed into a Tektronix 540 digital storage oscilloscope as shown in Figure 2.10.

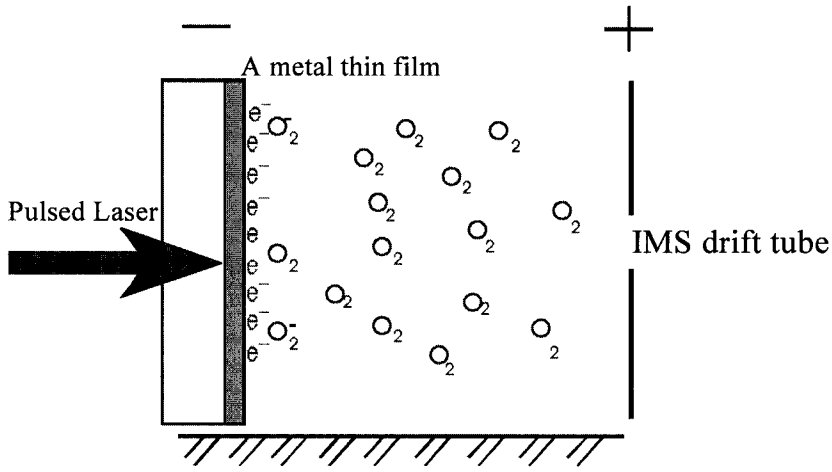

Figure 2.9. Photoemissive electrons from back-illuminated film of Au and electron attachment to oxygen ions in laboratory air.

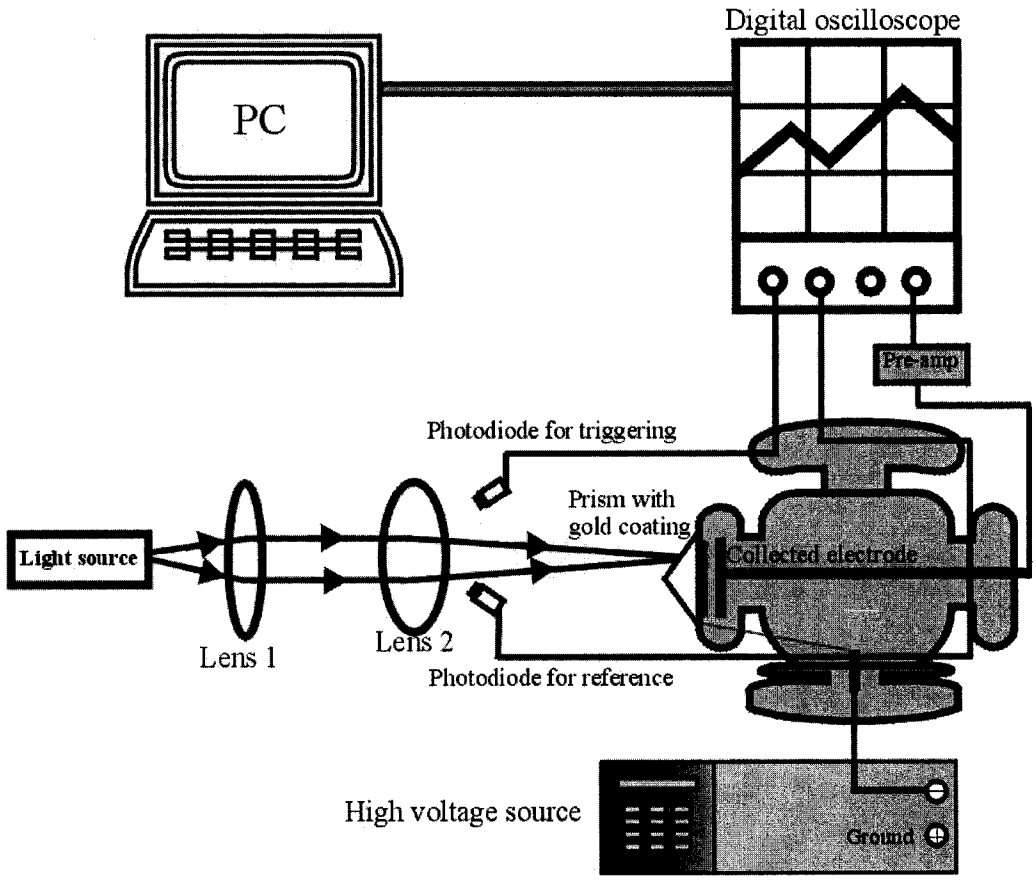

Figure 2.10. Experimental setup for detecting the oxygen ion signal due to electron attachment to oxygen molecules in air.

A program was written in the C++ language to download data from the digital oscilloscope to a personal computer through a GPIB card. A series of experiments measured the influence of bias voltage and film thickness on the oxygen anions resulting from photoemitted free electron attachment to oxygen molecules in air.

2.3.3. Results

2.3.3.1. Relationship Between Oxygen Anion Signal and Bias Voltage

Five 140 pulse-averaged waveforms were acquired at voltage settings of - 26.3 V, - 47.7 V, - 66.5 V, - 84.2 V, and - 101.6 V. Voltages were measured with a digital multimeter (Micronta). A 70 mL/min air flow rate was used. Figure 2.11 shows that the photocurrent induced by oxygen ions generated from associative electron attachment to oxygen molecules is a function of the bias voltage. The gold film thickness was approximately 20 nm based on the coating sputter time and film thickness as shown in Figure 2.8. The number of oxygen anions calculated from the charge in Figure 2.11 appears in Figure 2.12. Figure 2.12 reveals that the oxygen anion signal increases with bias voltage.

2.3.3.2. Relationship Between Oxygen Anion Signal and Film Thickness

It is seen in Figure 2.13 that the signal attenuation is exponentially dependent on the thickness of the thin gold film coated on the fused silica window for a fixed voltage of - 106 V, which was applied between the thin gold film and collecting electrode. The thin film reduces the UV light reaching the photoemitting side of the thin film exponentially because the thin gold film absorbs the UV light. Since the intensity of UV light absorbed by a metal film is an exponential function of the thickness of the metal film ($I = I_0 e^{-\alpha x}$), the reduction of the intensity of UV light may result in an exponential

decrease in the number of photoemitted electrons with the thickness of a thin gold film, and the number of oxygen anions exponentially decreases with the thickness of a film.

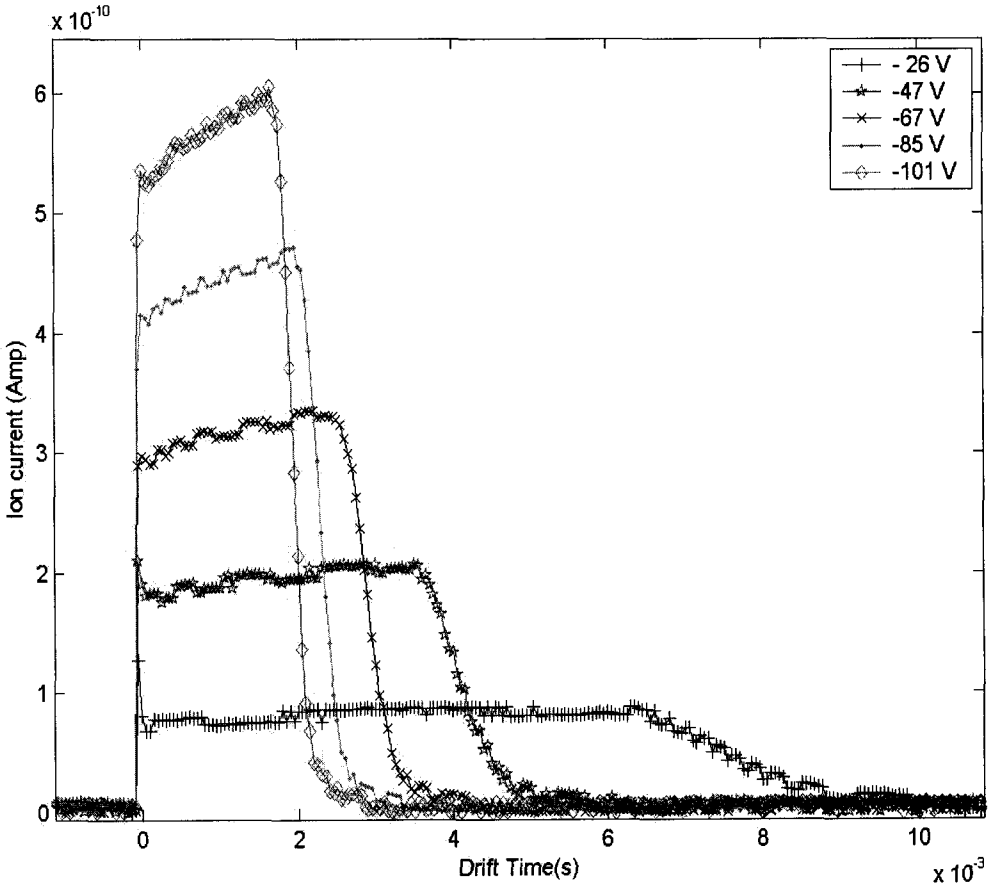

Figure 2.11. The photocurrent waveforms produced by the 20-nm gold film for different bias voltages.

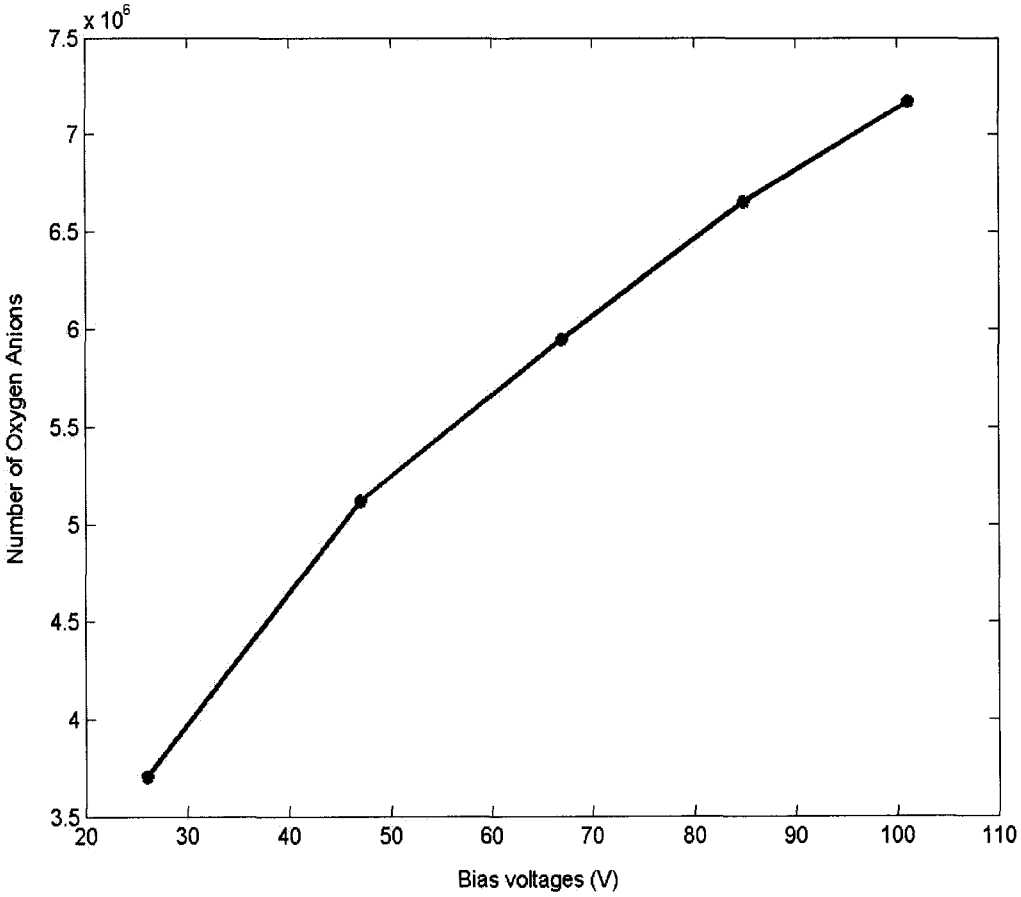

Figure 2.12. Number of anions collected versus the bias voltage.

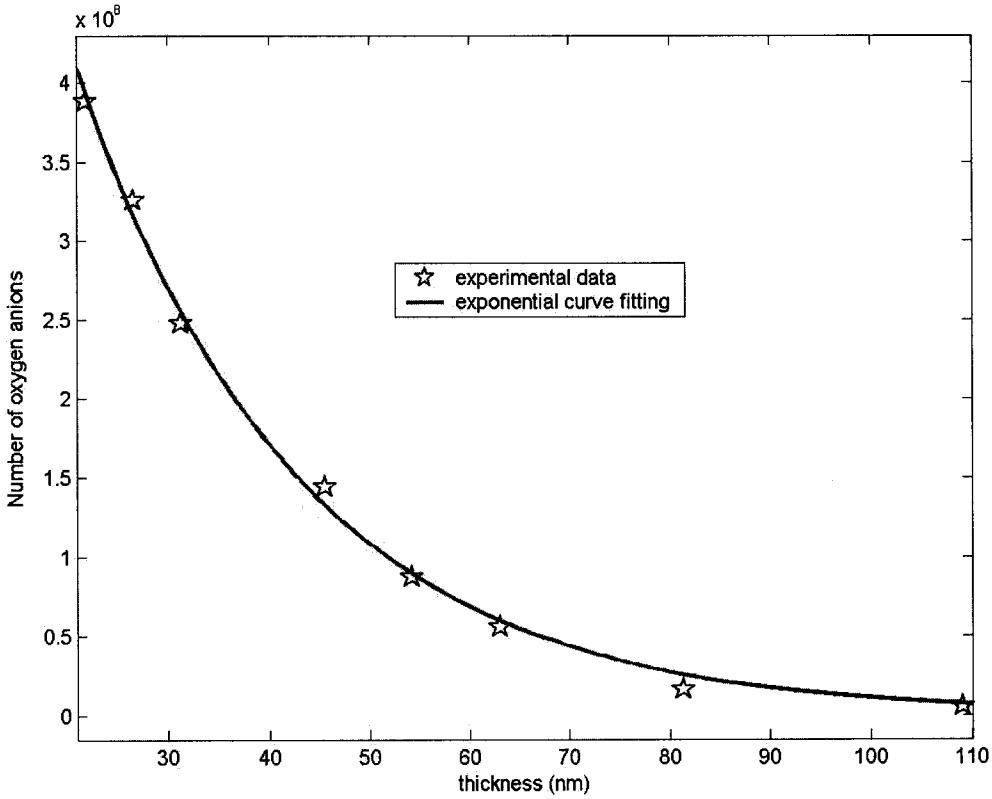

Figure 2.13. Number of oxygen anions versus thicknesses of the thin gold films.

CHAPTER 3

SURFACE-PLASMON ASSISTED PHOTOEMISSIVE ION SOURCE

A surface plasmon is an electromagnetic wave that propagates along the interface of two materials, one of which has a negative dielectric constant. Surface plasmons are oscillations of electrons that occur on the surfaces of solid materials that contain free electrons. Experimental studies have revealed that visible or infrared light can be substantially absorbed by metallic surfaces when surface plasmons are resonantly excited, resulting in a large enhancement of the number of electrons emitted by the surface of a metal.

3.1. Theory

3.1.1. Plasma Oscillation in a Metal [62–64]

It is impossible to deal theoretically with 10^{23} electrons in a typical metal individually, for instance, calculating the Coulomb potentials between all pairs of electrons. [65,66] A better way to study the optical properties considers the electrons in a metal as a whole system. In a metal, electron density fluctuates due to both Coulomb interactions and random thermal motion. In noble metals, the collective behavior due to Coulomb interactions among the free electrons dominates over random thermal motion. [66] The collective behavior, called plasma oscillation, is one we study as a whole system rather than a single charged particle, and it responds collectively to an external excitation such as light.

Researchers have investigated plasma oscillations in metals both theoretically and experimentally. [67,68] In solid state physics, many simple models to describe the behavior of electrons in a metal have been used. For example, in the jellium model, [69] the ionic lattice

is replaced by a uniform positive background where density is equal to the mean electronic density but of opposite sign. This simplification is adequate for the treatment of electron behavior in those metals in which the effects of the lattice periodicity are not important.

When an external excitation such as light is applied to the metal, the electron density is changed locally by the electric field of the electromagnetic wave. Electrons move to a region and accumulate with a density greater than necessary to obtain charge neutrality, leaving another region with a reduced electron density. The Coulomb repulsion between the electrons now produces motion in the opposite direction. This process continues causing longitudinal oscillations, called a plasma oscillation, in a metal.

Let us assume that the initial mean electron density is n_0. Due to an external electrical field (incident light), the electron number density changes slightly from n_0 to $n(r,t)$ at time t. $n(r,t)$ can be represented as

$$n(r,t) = n_0 + n_1 \ , \qquad (3.1)$$

where n_1 is a small quantity. As a result of a change in the electron density, an electric field is induced, which is determined from Maxwell's equation,

$$\nabla \cdot E = -4\pi e n_1 = -4\pi e (n - n_0) \ , \qquad (3.2)$$

where we dropped the arguments r and t in n for simplicity. For simplicity, we assume that the mean electron velocity, v_0, is equal to zero and that the actual velocity at time t is

$$\vec{v} = \vec{v}_0 + \vec{v}_1 = \vec{v}_1 \ , \qquad (3.3)$$

where $\vec{v}_1$ is the velocity due to the external electric field. Similarly, we assume that no electric field exists in the equilibrium state (no external influence); that is,

$$\vec{E}_0 = 0 \ , \qquad (3.4)$$

where $\vec{E}_0$ is the electric field in the equilibrium state. Then,

$$\vec{E} = \vec{E}_0 + \vec{E}_1 = \vec{E}_1 . \qquad (3.5)$$

Now we use the continuity equation,

$$\nabla \cdot \vec{J} + \frac{\partial \rho}{\partial t} = 0 , \qquad (3.6)$$

where $\vec{J} = -ne\vec{v} = -ne\vec{v}_1$ and $\rho = -en = -e(n_0 + n_1)$. By substituting the current density and the electron number density into the continuity equation (Eq. 3.6), we have the following relation:

$$\nabla \cdot \left(n\vec{v} \right) + \frac{\partial n}{\partial t} = 0 \qquad (3.7)$$

or

$$\nabla \cdot \left(n_0 \vec{v}_1 \right) + \nabla \cdot \left(n_1 \vec{v}_1 \right) + \frac{\partial n_1}{\partial t} = 0 . \qquad (3.8)$$

Because n_1 and $\vec{v}_1$ are small quantities and $\frac{\partial n_0}{\partial t} = 0$, the term, $n_1 \vec{v}_1$ can be neglected; we can obtain

$$\nabla \cdot \left(n_0 \vec{v}_1 \right) + \frac{\partial n_1}{\partial t} = 0 \qquad (3.9)$$

and

$$\nabla \cdot \vec{E} = \nabla \cdot \vec{E}_1 = -4\pi e n_1 . \qquad (3.10)$$

Recalling Newton's equation of motion

$$\frac{\partial \vec{v}_1}{\partial t} = -\frac{e\vec{E}_1}{m_e} . \qquad (3.11)$$

Differentiating Eq. 3.9 with respect to time yields

$$\frac{\partial^2 n_1}{\partial t^2} + n_0 \nabla \cdot \frac{\partial \vec{v}_1}{\partial t} = \frac{\partial^2 n_1}{\partial t^2} - n_0 \frac{e}{m_e} \nabla \cdot \vec{E}_1 = \frac{\partial^2 n_1}{\partial t^2} + \frac{4\pi e^2 n_0}{m_e} n_1 = 0 \qquad (3.12)$$

or

$$\frac{\partial^2 n_1}{\partial t^2} + \omega_p^2 n_1 = 0 , \qquad (3.13)$$

where $\omega_p^2 = \frac{4\pi e^2 n_0}{m_e}$. Eq. 3.13 describes the motion of a simple harmonic oscillator of frequency ω_p, showing that the electron density oscillates at the plasma frequency. This plasma oscillation is a collective excitation of the free electron inside a metal. The plasmon is the quantum of the plasma oscillation. The quantum energy of the plasmon in a free-electron-like metal with equilibrium electron number density, n_0, is

$$\hbar\omega_p = \hbar\left[\frac{4\pi n_0 e^2}{m_e}\right]^{\frac{1}{2}} , \qquad (3.14)$$

where ω_p is the resonant frequency. Plasmons can be excited by high-energy electrons passing through a thin metal film, by x-rays, or by light. The incoming electrons or photons of light lose some energy, equal to integer multiples of the plasmon energy, to excite the plasmons inside a metal (volume plasmons) resonantly.

3.1.2. Surface Plasmons

In addition to the possibility of optically exciting volume plasmons, the presence of a surface or interface between a medium with a positive dielectric constant (In this case, it is air.) and a medium with negative dielectric constant (such as metals) can result in special propagating electromagnetic waves called surface plasma waves which stay confined near

the interface.[67,70-72] Such surface waves have a component of the electric field decreasing exponentially away from the interface in the directions $\pm z$ shown in Figures 3.1 and 3.2.

3.1.2.1. Condition for Surface Plasmon Modes

The solutions of Maxwell's equations for a surface plasma wave propagating along the x axis (interface between medium 1 and 2) with frequency ω and wave vector k_{sp} are of the form[70,73,74]

$$\vec{E}_1 = (E_{1x}, 0, E_{1z}) e^{i(k_{sp}x - \omega t)} e^{-\alpha_1 z} \quad , \qquad (3.15)$$

or $z>0$

$$\vec{H}_1 = (0, H_{1y}, 0) e^{i(k_{sp}x - \omega t)} e^{-\alpha_1 z} \quad , \qquad (3.16)$$

and

$$\vec{E}_2 = (E_{2x}, 0, E_{2z}) e^{i(k_{sp}x - \omega t)} e^{\alpha_2 z} \quad , \qquad (3.17)$$

or $z<0$

$$\vec{H}_2 = (0, H_{2y}, 0) e^{i(k_{sp}x - \omega t)} e^{\alpha_2 z} \quad . \qquad (3.18)$$

The boundary conditions that need to be satisfied at the interface are that the tangential components of $\vec{E}$ and $\vec{H}$ must be continuous across the interface; that is,

$$\begin{cases} E_x|_{z=0} = \text{continuous} \\ H_y|_{z=0} = \text{continuous} \end{cases} . \qquad (3.19)$$

The first boundary condition gives

$$E_{1x} = E_{2x} \qquad (3.20)$$

and

$$H_{1y} = H_{2y} \quad . \qquad (3.21)$$

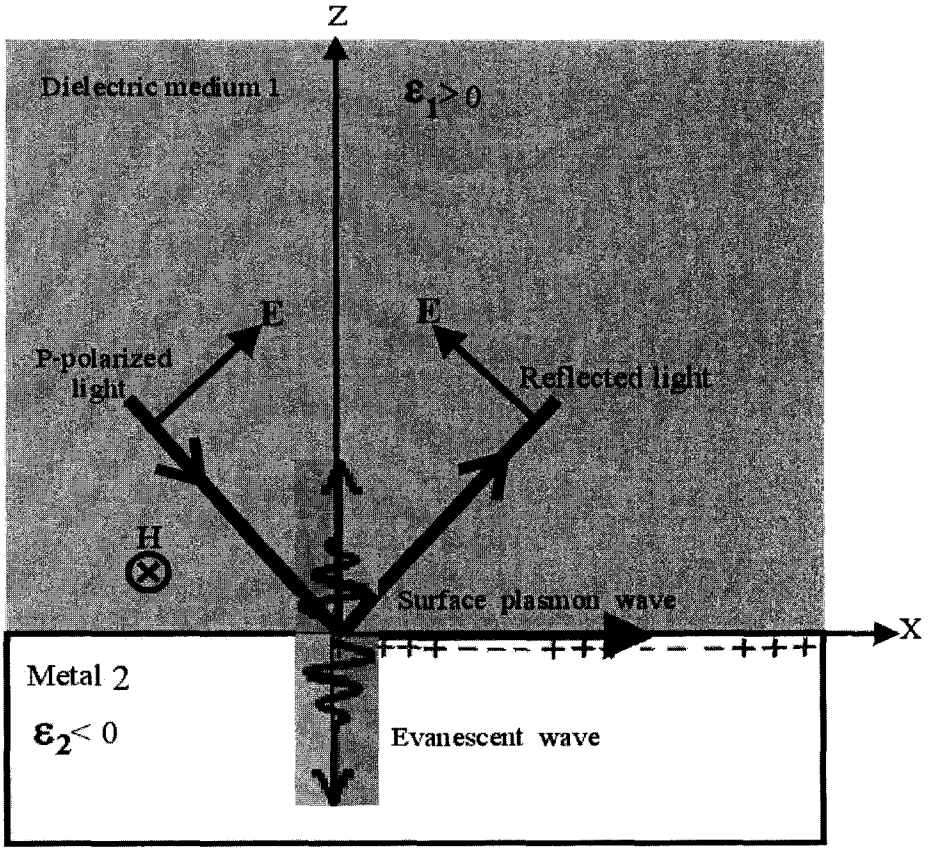

Figure 3.1. Excitation of a surface plasma wave at the interface between a metal (2) with dielectric constant ($\varepsilon_2 = \varepsilon_2' + i\varepsilon_2''$) and a dielectric medium (1) with dielectric constant (ε_1).

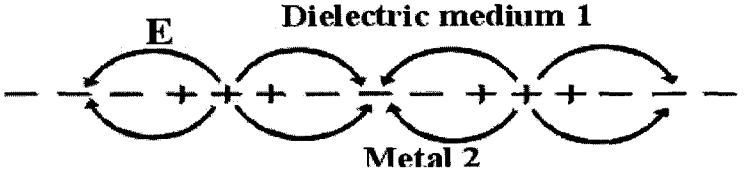

Figure 3.2. The charges and electromagnetic field of SPs on the medium-metal (1/2) interface.

Recall that one of Maxwell's equations [70] in the absence of external charges in Gaussian units is

$$\nabla \times \vec{H} = \frac{1}{c}\frac{\partial \vec{D}}{\partial t} = \frac{\varepsilon}{c}\frac{\partial \vec{E}}{\partial t} \quad . \tag{3.22}$$

By substituting Eqs. 3.15, 3.16, 3.17, and 3.18 into Eq. 3.22, we obtain

$$\begin{cases} -\alpha_1 H_{1y} = \dfrac{i\varepsilon_1}{c} E_{1x} & z > 0 \\ \alpha_2 H_{2y} = \dfrac{i\varepsilon_2}{c} E_{2x} & z < 0 \end{cases} . \tag{3.23}$$

Dividing these two equations gives rise to the condition for existence of the surface plasmon modes,

$$\frac{\alpha_1}{\alpha_2} = -\frac{\varepsilon_1}{\varepsilon_2} \quad . \tag{3.24}$$

Eq. 3.24 indicates that, if medium 1 has $\varepsilon_1 > 0$, then medium 2 must have a negative dielectric function, $\varepsilon_2 < 0$. Metals have negative dielectric functions. Thus, the interface between a metal and vacuum (or air) could support a surface plasmon wave. It should be pointed out that only p-polarized light can satisfy Maxwell equations together with the boundary conditions while s-polarized light cannot satisfy the boundary conditions. In other words, p-polarized light can excite surface plasmons resonantly, but s-polarized light cannot. [70,72]

By solving Maxwell's equations [20] for nonmagnetic, isotropic materials, the dispersion relation for a surface plasmon (SP) at a semi-infinite interface can be obtained. From Maxwell's equations, the wave equation without external charges in Guassian units is as follows:

$$\nabla^2(E_x, E_y, E_z) = \frac{\varepsilon}{c^2}\frac{\partial^2}{\partial t^2}(E_x, E_y, E_z) \ . \tag{3.25}$$

Substitution of Eqs. 3.15, 3.17, and 3.20 into Eq. 3.25 results in

$$\begin{cases} \left(-k_{sp}^2 + \alpha_1^2\right)(E_{1x}, 0, E_{1z}) = -\frac{\varepsilon_1}{c^2}\omega^2(E_{1x}, 0, E_{1z}) & z > 0 \\ \left(-k_{sp}^2 + \alpha_2^2\right)(E_{1x}, 0, E_{2z}) = -\frac{\varepsilon_2}{c^2}\omega^2(E_{1x}, 0, E_{2z}) & z < 0 \end{cases} . \tag{3.26}$$

From Eq. 3.26, we obtain

$$\begin{cases} \left(-k_{sp}^2 + \alpha_1^2\right) = -\frac{\varepsilon_1}{c^2}\omega^2 \\ \left(-k_{sp}^2 + \alpha_2^2\right) = -\frac{\varepsilon_2}{c^2}\omega^2 \end{cases} \tag{3.27}$$

or

$$\begin{cases} \alpha_1^2 = k_{sp}^2 - \frac{\varepsilon_1}{c^2}\omega^2 \\ \alpha_2^2 = k_{sp}^2 - \frac{\varepsilon_2}{c^2}\omega^2 \end{cases} . \tag{3.28}$$

By dividing the two equations in Eq. 3.28, we obtain

$$\frac{\alpha_1^2}{\alpha_2^2} = \frac{k_{sp}^2 - \frac{\varepsilon_1}{c^2}\omega^2}{k_{sp}^2 - \frac{\varepsilon_2}{c^2}\omega^2} = \frac{\varepsilon_1^2}{\varepsilon_2^2} \ . \tag{3.29}$$

We can simplify Eq. 3.29 to

$$k_{sp}^2 = \frac{\omega^2}{c^2}\frac{\varepsilon_1\varepsilon_2(\omega)}{\varepsilon_1 + \varepsilon_2(\omega)} \ . \tag{3.30}$$

By inserting ε_1 and ε_2 into Eq. 3.30, we obtain

$$k_{sp} = \frac{\omega}{c}\sqrt{\frac{\varepsilon_1\varepsilon_2(\omega)}{\varepsilon_1 + \varepsilon_2(\omega)}} = k_0\sqrt{\frac{\varepsilon_1\left(\varepsilon_2'(\omega) + i\varepsilon_2''(\omega)\right)}{\varepsilon_1 + \left(\varepsilon_2'(\omega) + i\varepsilon_2''(\omega)\right)}} \ , \tag{3.31}$$

or

$$k_{sp} = k_0 \sqrt{\frac{\varepsilon_1 \times \varepsilon_2'(\omega) + \varepsilon_1 \times \varepsilon_2''(\omega) \times i}{(\varepsilon_1 + \varepsilon_2'(\omega)) + \varepsilon_2''(\omega) \times i}} \quad , \tag{3.32}$$

where k_{sp} is the propagation constant of the surface plasmons traveling at the metal/medium (2/1) interface, ε_1 is the dielectric constant of medium 1, $\varepsilon_2(\omega)$ is the dielectric constant of the a metal, $\varepsilon_2'(\omega)$ is the real part of the dielectric function of the metal, and $\varepsilon_2''(\omega)$ is the imaginary part of the dielectric function of the metal. The factor, $k_0 = \frac{\omega}{c} = \frac{2\pi}{\lambda}$, is the propagation constant in free space (vacuum). $\varepsilon_2(\omega)$ is the frequency dependence of the dielectric function of medium 2 which is a metal. The propagation constant of the SP depends on the wavelength due to the wavelength dependence of $\varepsilon_2(\omega)$.

3.1.2.2. Penetration Depth in a Metal Film [70]

The surface plasmon is a wave confined at the metal-dielectric interface (surface-bound wave). It will propagate along one direction (in our case, the x direction) and create two evanescent fields perpendicular to the direction of the SP propagation (here the +z and –z directions). Generating two evanescent waves is the condition for the existence of SP. The SP is supported by evanescent fields on both sides of the interface, with certain penetration depths, that can be calculated. Recall Eqs. 3.15, 3.17, and 3.28 as follows:

$$\begin{cases} \vec{E}_1 = (E_{1x}, 0, E_{1z}) e^{i(k_{sp}x - \omega t)} e^{-\alpha_1 z} & z > 0 \\ \vec{E}_2 = (E_{2x}, 0, E_{2z}) e^{i(k_{sp}x - \omega t)} e^{-\alpha_2 z} & z < 0 \end{cases} \tag{3.33}$$

and

$$\begin{cases} \alpha_1^2 = k_{sp}^2 - \frac{\varepsilon_1}{c^2}\omega^2 \\ \alpha_2^2 = k_{sp}^2 - \frac{\varepsilon_2}{c^2}\omega^2 \end{cases} . \tag{3.34}$$

It is clear that the field amplitude of the surface plasmons decreases exponentially as $e^{-\alpha_1 z}$ and $e^{-\alpha_2 z}$, normal to the surface. The value of the (skin) depth at which the field falls to 1/e is

$$z_i = \frac{1}{\alpha_i} \quad i=1, 2 . \tag{3.35}$$

When $|\varepsilon_2^{''}| < |\varepsilon_2^{'}|$, Eq. 3.32 becomes (See details in Appendix A.)

$$\begin{cases} k_{sp}^{'} \approx \dfrac{\omega}{c}\sqrt{\dfrac{\varepsilon_1\varepsilon_2^{'}}{\varepsilon_2^{'}+\varepsilon_1}} \\ k_{sp}^{''} \approx \dfrac{\omega}{c}\left[\dfrac{\varepsilon_1\varepsilon_2^{'}}{\varepsilon_2^{'}+\varepsilon_1}\right]^{\frac{3}{2}} \dfrac{\varepsilon_2^{''}}{2(\varepsilon_2^{'})^2} \end{cases}, \tag{3.36}$$

where $k_0 = \omega/c = 2\pi/\lambda$ is the propagation constant in free space (vacuum). Since α_1 and α_1 are real numbers, we substitute the real part of k_{sp} into Eq. 3.30 to calculate α_1 and α_2:

$$\alpha_1^2 = \left|(k_{sp}^{'})^2 - \frac{\varepsilon_1}{c^2}\omega^2\right| = \frac{\omega^2}{c^2}\left(\varepsilon_1 - \frac{\varepsilon_2^{'}\varepsilon_1}{\varepsilon_2^{'}+\varepsilon_1}\right) = k_0^2\left(\frac{\varepsilon_1^2}{\varepsilon_2^{'}+\varepsilon_1}\right) \tag{3.37}$$

and

$$\alpha_2^2 = \left|(k_{sp}^{'})^2 - \frac{\varepsilon_2^{'}}{c^2}\omega^2\right| = \frac{\omega^2}{c^2}\left(\varepsilon_2^{'} - \frac{\varepsilon_2^{'}\varepsilon_1}{\varepsilon_2^{'}+\varepsilon_1}\right) = k_0^2\left(\frac{\varepsilon_2^{'2}}{\varepsilon_2^{'}+\varepsilon_1}\right) . \tag{3.38}$$

The value of the skin depth at which the field falls to 1/e becomes

$$z_1 = \frac{1}{\alpha_1} = \frac{1}{k_0}\left(\frac{\varepsilon_2^{'}+\varepsilon_1}{\varepsilon_1^2}\right)^{1/2}, \tag{3.39}$$

where z_1 is the skin depth in the dielectric medium 1.

$$z_2 = \frac{1}{\alpha_2} = \frac{1}{k_0}\left(\frac{\varepsilon_2^{'}+\varepsilon_1}{\varepsilon_2^{'2}}\right)^{1/2}, \tag{3.40}$$

where z_2 is the skin depth in the metal.

3.1.2.3. Propagation Length of the Surface Plasmons [70]

Since the dielectric function of the surface plasmons is a complex number and the imaginary part of this complex number is related to the absorption, the intensity of the surface plasmons along a smooth surface decreases as $e^{-2k''_{sp}x}$. The propagation length, L, defined by the 1/e decrease of the SP intensity is given by $L = \frac{1}{2k''_{sp}}$. Therefore, *L* is determined by the imaginary part of k''_{sp}, which accounts for internal damping processes.

3.1.2.4. Excitation of Surface Plasmons by Light [70]

It is well established that a flat metal-dielectric interface may support a surface plasmon which has a wave vector along the interface. The wave vector of a SP (Eq. 3.36), k'_{sp}, is greater than that of incident radiation in the adjacent dielectric. In order to excite the wave vector of a SP, the wave vector of SP must be equal to that of the incident light; therefore, it is generally expected that there has to be some mechanism for enhancing the wave vector of the incident light. Increasing the wave vector of the incident light is either achieved by prism-coupling or grating-coupling.

3.1.2.4.1. Grating Coupler

Figure 3.3 shows the grating-coupling configuration. If light ($k=\omega/c$) is incident on a grating with a grating constant, d, at angle θ, its component in the surface has the wave vector

$$k_x = \frac{\omega}{c}\sqrt{\varepsilon_1}\sin\theta + \frac{2\pi m}{d}, \qquad (3.41)$$

where ω is the frequency of the light incident on the grating, c is the speed of the light,

d is the period of the grating, and m is an integer. When the parallel component of the wave vector of the incident light matches the surface plasmon wave vector, the surface plasmon wave is resonantly excited. This condition is

$$k_x = k_{sp} \ . \qquad (3.42)$$

From Eqs. 3.36 and 3.41, Eq. 3.42 becomes

$$\frac{\omega}{c}\sqrt{\varepsilon_1}\sin\theta + \frac{2\pi m}{d} = \frac{\omega}{c}\sqrt{\frac{\varepsilon_2'}{\varepsilon_2'+1}} \ . \qquad (3.43)$$

3.1.2.4.2. Prism Coupler

In the late sixties, Kretschmann and Otto developed prism SP excitation schemes.[75,76] In the Kretschmann-Raether configuration, the optical substrate (prism) is coated with a thin metal layer as shown in Figure 3.4. The Otto configuration uses the method of attenuated total reflection where the evanescent wave is coupled from the prism into the metal through thin air spacing, while the evanescent wave is directly coupled from the prism into a thin metal film in the Kretschmann-Raether configuration. Raether showed that only p-polarized light was able to couple to the plasmon mode; that is, s-polarized light does not excite plasmons.[75] The p-polarized light electric field vector is in the plane of incidence oscillating perpendicular to the plane of the metal film while s-polarized light has its electric field vector oriented parallel to the metal film.

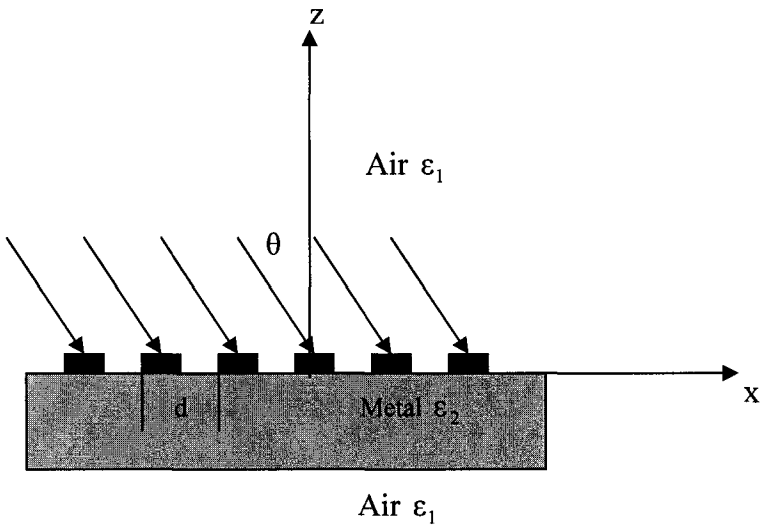

Figure 3.3. The grating-coupling configuration for excitation of surface plasmons.

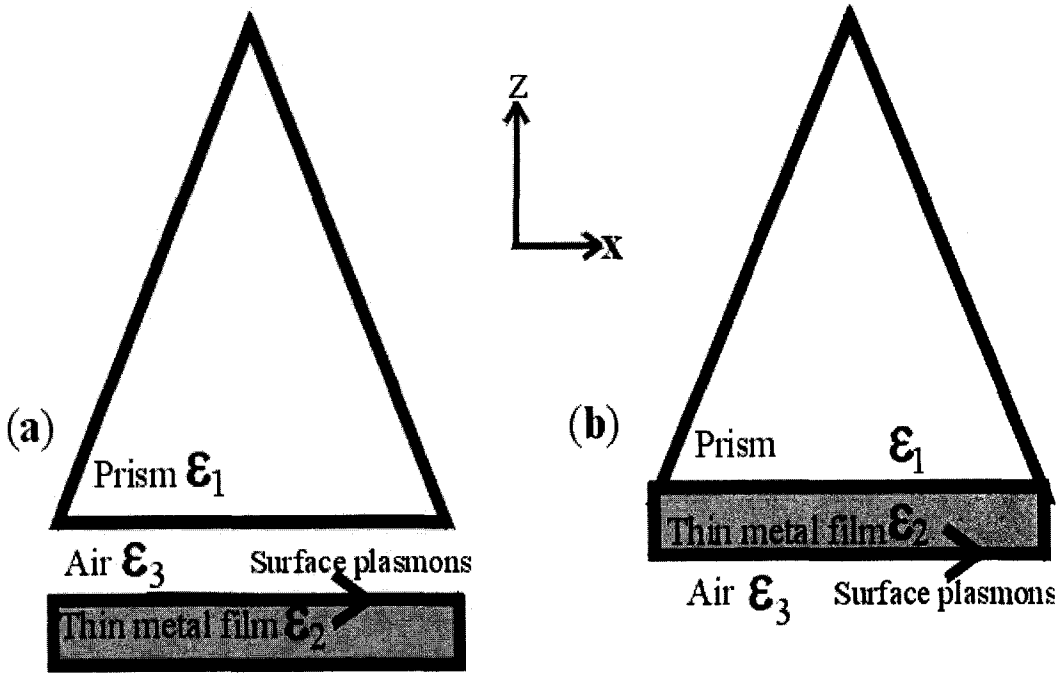

Figure 3.4. The prism-coupling configuration is shown. The first one (a) is the Otto configuration. The second (b) is the Kretschmann-Raether configuration.

In this work, the Kretschmann-Raether configuration was used to increase the wave vector of an incoming light, k_x, to excite the surface plasmons propagating on the interface $\varepsilon_2/\varepsilon_3$ (metal/air) as shown in Figure 3.4. A thin gold film with dielectric constant (2), ε_2, contacts the fused silica prism (1). The electromagnetic field decreases exponentially in the gold film and excites the surface plasmons on the metal/air (2/3) interface.[70] The resonance condition for surface plasmons at the metal/air interface is

$$k_x = k_{sp} \ , \tag{3.44}$$

where k_x is the x component of the wave vector of an incoming light that is incident on the prim/metal interface and equal to

$$k_x = \frac{\omega}{c}\sqrt{\varepsilon_1}\sin\theta \ . \tag{3.45}$$

From Eqs. 3.36 and 3.45, Eq. 3.44 becomes

$$\frac{\omega}{c}\sqrt{\varepsilon_1}\sin\theta = \frac{\omega}{c}\sqrt{\frac{\varepsilon_2'\varepsilon_3}{\varepsilon_2'+\varepsilon_3}} = \frac{\omega}{c}\sqrt{\frac{\varepsilon_2'}{\varepsilon_2'+1}} . \tag{3.46}$$

By changing the incident beam angle, θ, the surface plasmons on the meal/air (2/3) interface can be resonantly excited where the total internal reflection occurs. The incident angle at which the 532 nm and 632.8 nm wavelength lasers can excite the surface plasmons at the Au-air interface is calculated as follows:

$$\sin\theta_{532} = \sqrt{\frac{\varepsilon_2'}{\varepsilon_1(\varepsilon_2'+1)}} = 0.7424 \quad \text{or} \quad \theta_{532} = 47.9^\circ \tag{3.47}$$

and

$$\sin\theta_{633} = \sqrt{\frac{\varepsilon_2'}{\varepsilon_1(\varepsilon_2'+1)}} = 0.7274 \quad \text{or} \ \theta_{633} = 46.7^\circ \ . \tag{3.48}$$

3.1.3. Three-Layer Reflectance by Fresnel's Equation

Fresnel's reflectance[77] at the interface between air and metal provides a good starting point of an explanation of the nature of surface plasmons. The resonance condition of the p-polarized light in the prism with the surface plasmon at the metal (2)-air (3) interface shown in Figure 3.5 (Kretschmann-Raether configuration) is

$$\frac{\omega}{c}\sqrt{\varepsilon_1}\sin\theta = \frac{\omega}{c}\sqrt{\frac{\varepsilon_2'}{\varepsilon_2'+1}}. \qquad (3.49)$$

The three-layer (prism-metal-air shown in Figure 3.5) reflection coefficient, r_{123}, can be given by Fresnel's equations[77] in the form of

$$r_{123} \approx \frac{r_{12} + r_{23}e^{2ik_{z2}d}}{1 + r_{12}r_{23}e^{2ik_{z2}d}}, \qquad (3.50)$$

where $k_{z2}d = (k_2\cos\theta)d = \frac{\omega}{c}d\left(\varepsilon_2 - n_1^2\sin^2\theta\right)^{1/2}$ and

$$r_{ik} = \frac{\left(\frac{k_{zi}}{\varepsilon_i}\right) - \left(\frac{k_{zk}}{\varepsilon_k}\right)}{\left(\frac{k_{zi}}{\varepsilon_i}\right) + \left(\frac{k_{zk}}{\varepsilon_k}\right)} \quad (i,k = 1,2,3)\ .^{70} \qquad (3.51)$$

At resonance, the thin gold film absorbs the most energy of the incoming light, resulting in the lowest value of the reflectivity, r_{123}. In other words, the intensity of the electromagnetic field at the air/gold interface reaches its maximum, giving rise to enhancement of photoyields.[70,78-80]

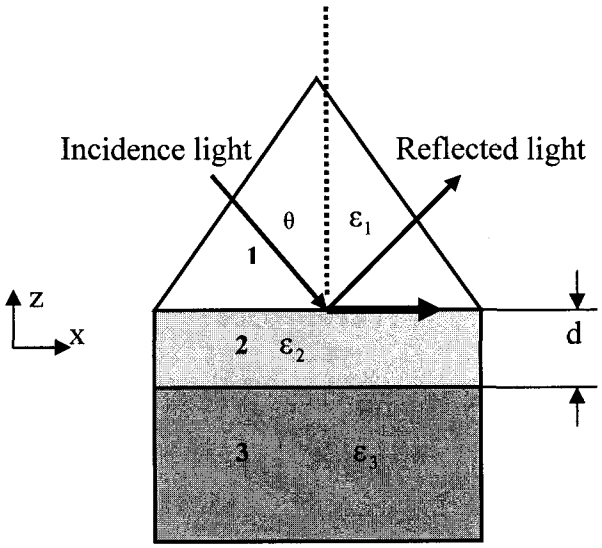

Figure 3.5. Schematic diagram of the prism coupler (Kretschmann-Raether configuration). 1, 2, and 3 represent a fused silica prism, thin metal film, and air, respectively.

3.1.4. Results

The permittivities of gold at 266 nm, 532 nm, and 632.8 nm are[81]

$$\begin{cases} \varepsilon_2 = -0.79 + 5.52\mathrm{i} \\ \varepsilon_2 = -6.29 + 2.04\mathrm{i} \\ \varepsilon_2 = -9.90 + 1.05\mathrm{i} \end{cases} . \qquad (3.52)$$

A program written in Matlab (See details in Appendix B.) plotted reflectance, $R = r_{ik}(r_{ik})^*$, versus incidence angle. The thickness of the thin gold film used for calculation was 45 nm. As shown in Figure 3.6, the dip in the computed plot is caused by the resonant excitation of a surface plasmon at the gold-air interface by the p-polarized laser at the 532 nm and 632.8 nm wavelengths. It is also seen in Figure 3.6 that the reflectance reaches a maximum value just after the critical angle is reached for 532 nm and 632.8 nm, but not for 266 nm. Since the surface plasmon excitation only exists at the surface of a metal for which $\mathrm{Re}(\varepsilon_2) = \varepsilon_2' < -1$,[78] where ε_2 is the dielectric function of the metal, and the real part of the dielectric function ($\mathrm{Re}(\varepsilon_2)$) of gold at a wavelength of 266 nm is greater than - 1, the p-polarized 266 nm ultraviolet light cannot excite the surface plasmons resonantly as shown in Figure 3.6.

Figure 3.7 indicates how the reflectance changes with thickness of a thin gold film using p-polarized light at the given wavelength of 632.8 nm. The thicknesses of the gold film are 25 nm, 45 nm, and 65 nm, respectively. The maximum value decreases as the thickness of the Au film increases as expected. The reflectance decreases from its maximum very rapidly to a minimum of which value also depends on the thickness of the Au film. At resonance, since the power of the SPs is lost by internal absorption in the metal and this loss is greatest, the intensity of the reflected light reaches a minimum, or a "dip."

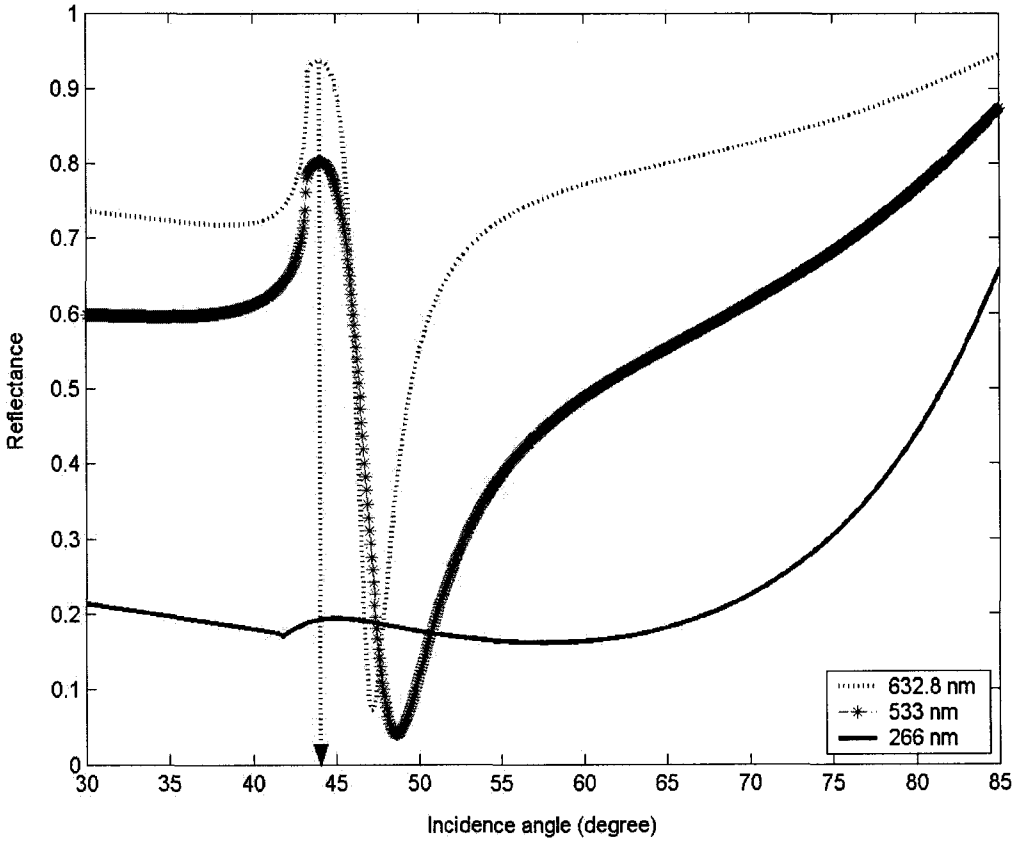

Figure 3.6. Reflectance of the surface plasmon mode versus the incident angle for fixed film thickness (45 nm) and varying the wavelengths of the p-polarized incident light (266 nm, 532 nm, and 632.8 nm). The arrow indicates the critical angle.

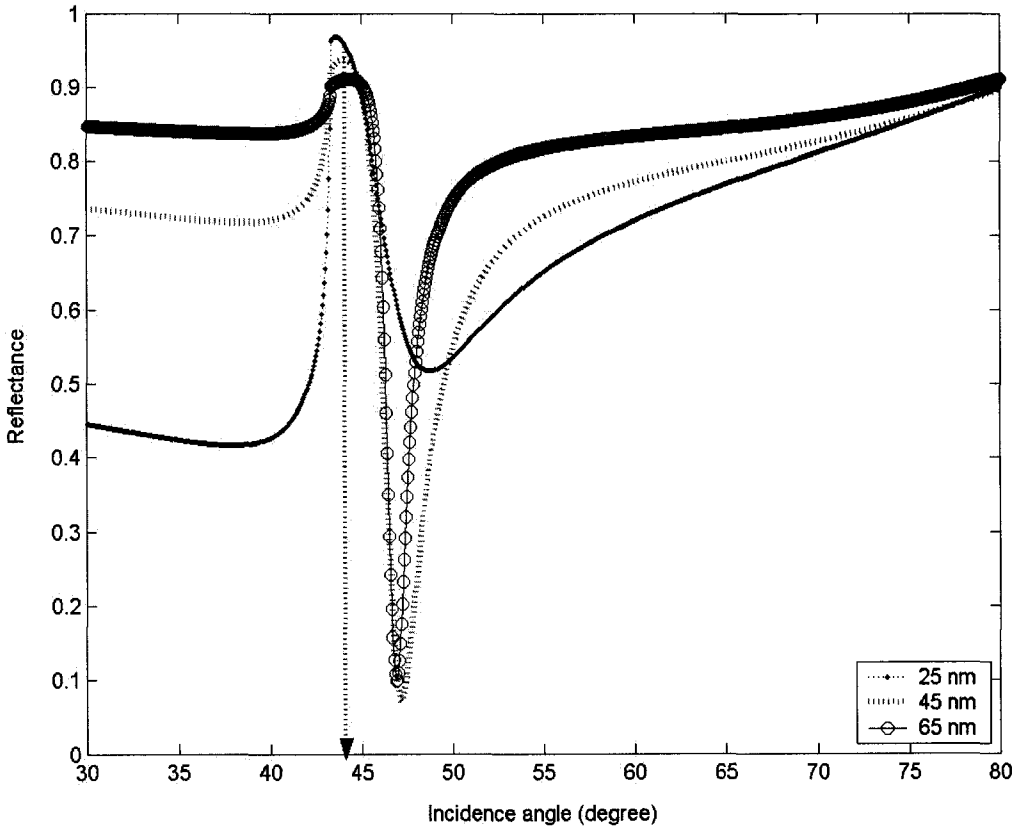

Figure 3.7. Reflectance of the surface plasmon mode versus the incident angle for varying thickness of gold films at the He-Ne laser wavelength 632.8 nm. The arrow indicates the critical angle.

As shown in Figure 3.7, for thinner films, the minimum broadens, and its value increases toward the value of 1 when the thickness is reduced.

3.2. Experimental Section

3.2.1. Instrumentation

Figure 3.8 shows a schematic illustration of the surface plasmon resonance detection system. A surface plasmon reflectance spectrum was measured by using a collimated (unfocused) and p- or s-polarized laser of wavelengths 266 nm, 532 nm, and 632.8 nm. The Nd:YAG laser had a repetition rate of 10 Hz with a pulse duration of 5 ns. The size of the laser beam was limited by using a 2.0-mm diameter aperture. After passing through a half-wave plate, the beam splitter split the incoming laser beam into two beams, one going to the reference detector and the other to a prism. The laser irradiated the metal film from the fused silica side and was reflected by the prism with back-side gold coating so that a theoretical fit to the experimental reflectance spectrum using Fresnel's equation (Eq. 3.50) could be performed. The reference detector was a photodiode. Another photodiode detector measured the reflected beam as the incident angle was varied. The fused silica prism was mounted on a rotational stage. The Kretschmann-Raether[75] configuration was used in order that the incident light (photons) phase-matched the surface plasmons (SPs), resulting in the resonant excitation of SPs at the gold/air interface. The half-wave plate varied the input polarization of the incidence light beam from p- to s-polarization.

The prism size was 12.7 mm × 12.7 mm × 12.7 mm (equilateral prism, I. S. P. Optics, Inc.). The photodiode detector (818 Series, Newport, Irvine, CA) for 632.8 nm, a photodiode detector or Molectron pyroelectric detector (J9LP-1, Molectron Detector, Inc., Portland, OR) for 532 nm, and the Melecron pyroelectric detector (J3S-10-1235, Molectron

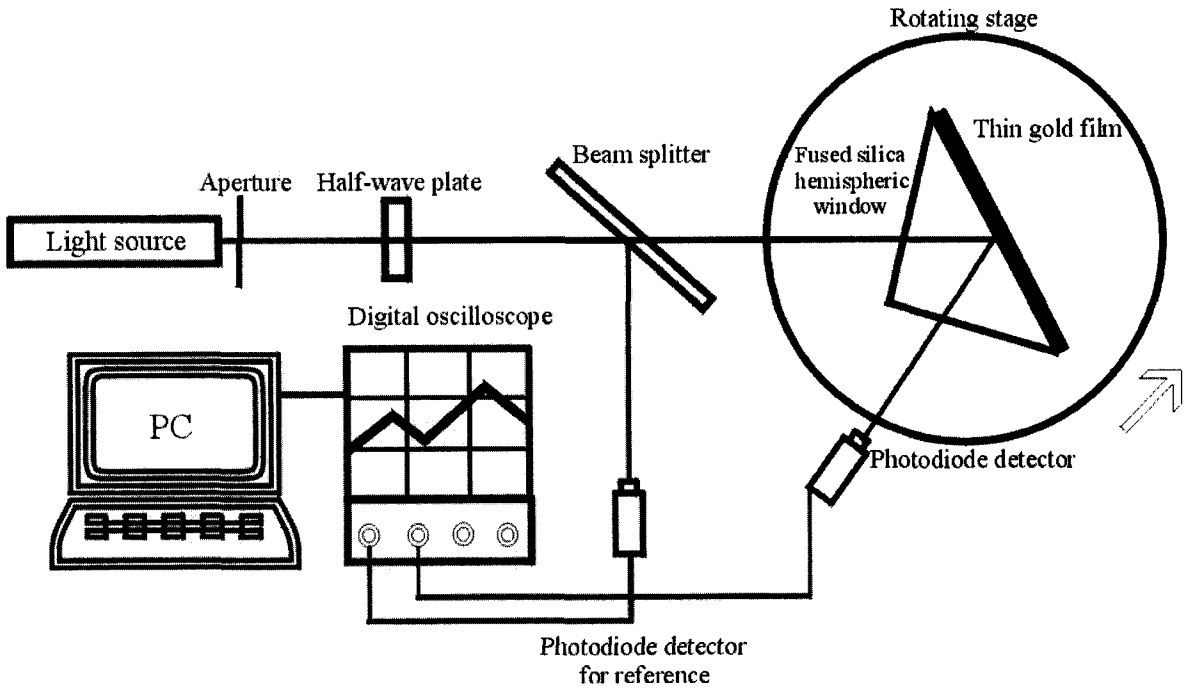

Figure 3.8. Experimental setup for the surface plasmon resonance.

Detector, Inc., Portland, OR) for 266 nm measured the reflected intensity of either s- or p-polarized light. The metal films used in this study were Au with thicknesses of 43.0 nm, 30.0 nm, and 20.0 nm. These thicknesses were measured using the Michelson interferometer discussed in Section 2.5.

3.2.2. Procedures

The experiments were carried out by measuring the intensity of reflected light from the Au coating surface irradiated with the Microchip laser and Nd:YAG laser (Continuum, Surelite II) capable of delivering 532 nm as well as 266 nm wavelength with pulse energies 100 nJ and 230 μJ, respectively. The 632.8-nm He-Ne laser (Uniphase, 1100) with output power of 3 mW was also used to illuminate the Au films. The s- or p-polarized light was split into 2 beams using a 50% beam splitter. One beam was measured as a reference for the power of the incident light, and the other was transmitted to a fused silica prism with back-side gold coating in the Kretschmann-Raether configuration. Rotating the half-wave plate changed the polarization direction of the incident laser. The reflectance as a function of incident angle was measured using a rotational stage.

3.2.3. Results and Discussion

3.2.3.1. Reflectance

It is seen in Figure 3.9 that the reflected intensity decreases very slowly until the intensity reaches the maximum at the critical angle. As the incident angle was increased, the reflectance was observed first to decrease sharply and then to increase again as expected. For 632.8 nm, the gold film thickness of 43 nm produces a shallow reflectance minimum corresponding to the surface plasmon resonance as shown in Figure 3.9.

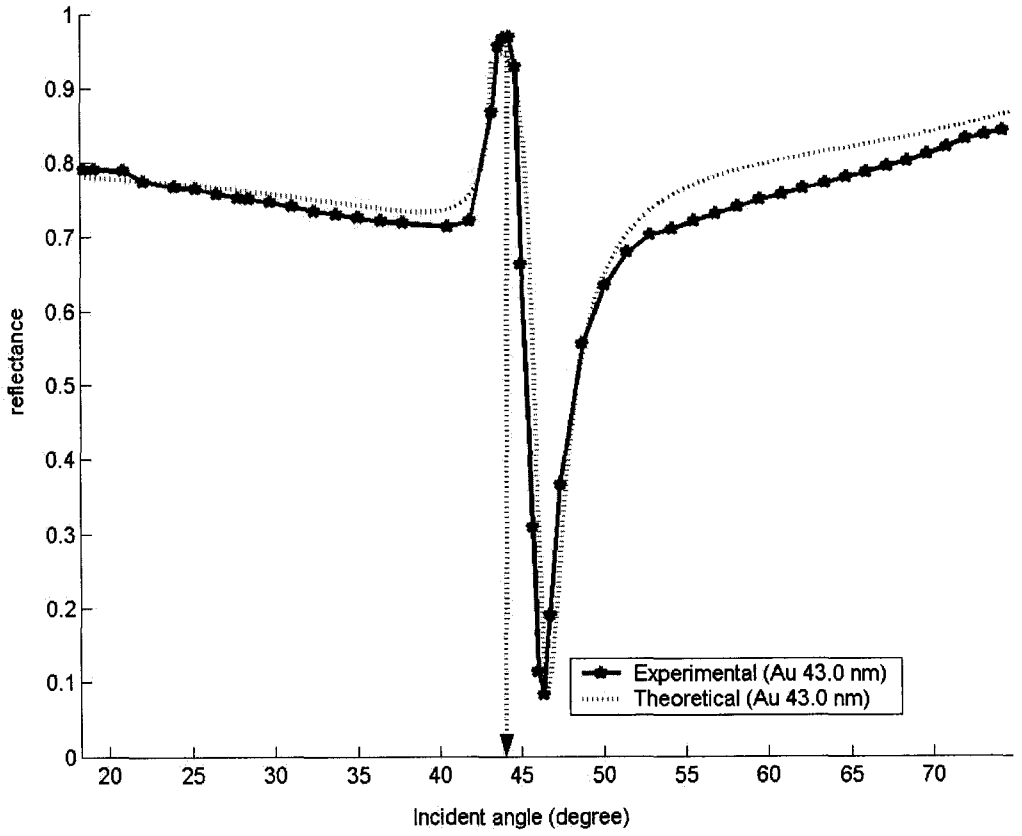

Figure 3.9. Comparing the reflectance as a function of incident angle computed theoretically by the three-layer Fresnel's equation to that measured with a right-angle fused silica prism coated with a 43.0-nm gold film at the wavelength of 632.8 nm. The arrow indicates the critical angle.

Figure 3.10 compares the calculated reflectance using Fresnel's equation to that measured at the 532 nm wavelength for both s- and p-polarized light. The reflectance at the surface plasmon resonance angle for a gold film of 30 nm thickness is 49°. From this result, it is clear that the absence of the surface plasmon reflectance dip with the s-polarized laser beam is distinctively noticeable because the s-polarized light is unable to excite the surface plasmons at the gold-air interface.

The s- and p-polarized reflectance spectra (two dotted-line curves) calculated using the three-layer Fresnel's equation are compared to experimental results measured with the same film thickness, 20 nm, at the wavelength of 266 nm in Figure 3.11. The reflectance of p-polarized light as a function of incident angle agrees with the experimental result while the theoretical reflectance is different from the measured reflectance with s-polarized light. This discrepancy is not presently understood. It is obvious that the experimental data are in good agreement with the theoretical results when using p-polarized laser at wavelengths of 632.8 nm, 532 nm, and 266 nm, respectively.

3.2.3.2. Enhancement of the Photoelectric Yield by P- and S-Polarized 266 nm Laser

The experimental setup is shown in Figure 2.10. The light source used for this experiment was the microchip laser that delivered 266 nm with a pulse energy and repetition rate of 100 nJ and 100 Hz, respectively. The collimated beam irradiated the 20-nm thick gold film from the fused silica side. The polarization direction of the light was varied by rotating a half-wave plate. A bias voltage of 100 V was applied to a copper anode disk (48.5 mm diameter and 6.7 mm thick) held 5 mm in front of the metal film.

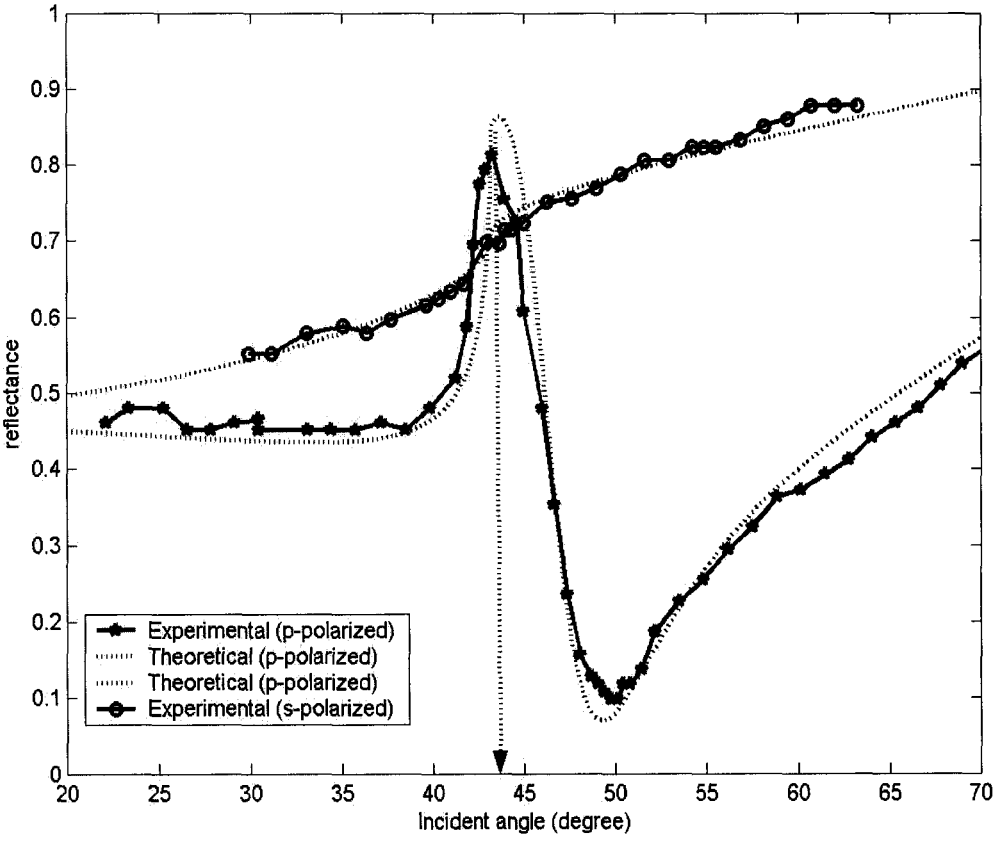

Figure 3.10. The reflectance versus the incident angle measured with a right-angle fused silica prism coated with a 30.0-nm gold film using both s-polarized and p-polarized laser at the 532 nm wavelength with the microchip laser and comparing to the theoretical results. The arrow indicates the critical angle.

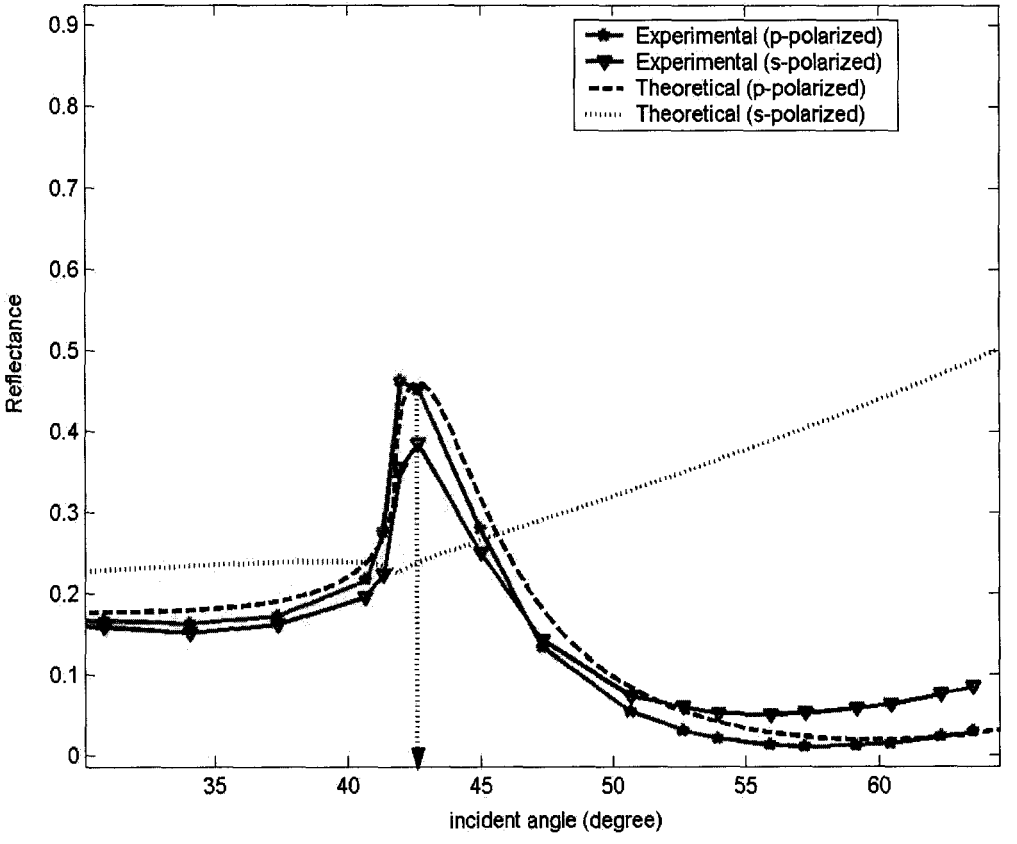

Figure 3.11. The reflectance as a function of incident angle calculated by the three-layer system Fresnel's equation with s-polarized and p-polarized 266-nm laser at a gold film (20-nm thick) compared to that measured from back-illuminated film of the 20-nm thick gold film as a function of the incident angle. The arrow indicates the critical angle.

The free electrons or oxygen ions leaving the gold-air interface were detected by a digital oscilloscope via a pre-amplifier while the flow rate of either ultra pure nitrogen or breathing-grade air drift gas was constant. The data were then stored in a computer for further analysis through a GPIB cable. The ion current signals (free electron emission or oxygen ion current) were measured as the incident angle of the laser beam was varied using a rotating stage.

Figure 3.12 shows the variation of the electron signal (lower plot) and reflectance (upper plot) as a function of the incidence angle for an Au coating thickness of 20 nm and with pulse energy of 100 nJ. At an angle of 40° (less than the critical angle by about 2°), the reflectance and the number of emitted electrons start increasing almost simultaneously. The reflectance reaches a maximum at the critical angle of 42° while the number of electrons reaches a maximum at the angle of 47.3°, which is greater than the critical angle by 5.3°, and then remains approximately the same. The same experiment with an s-polarized laser beam gives an electronic signal of about the same order in magnitude. Furthermore, both the reflectance and electron signal spectra with an s-polarized laser light follow a very similar trend to those of p-polarization shown in Figure 3.12.

As discussed before, the 266-nm laser beam coupling to the surface plasma cannot be evidenced by a decrease in the reflected laser intensity because it does not satisfy the resonance condition as discussed in Section 3.1. A possible explanation for the photoelectric emission enhancement is that the 20-nm thick gold film is thin enough that the evanescent field of the optical beam can penetrate into the gold-air interface and thus help electrons escape from the gold-air interface, enhancing the electron signal. Most

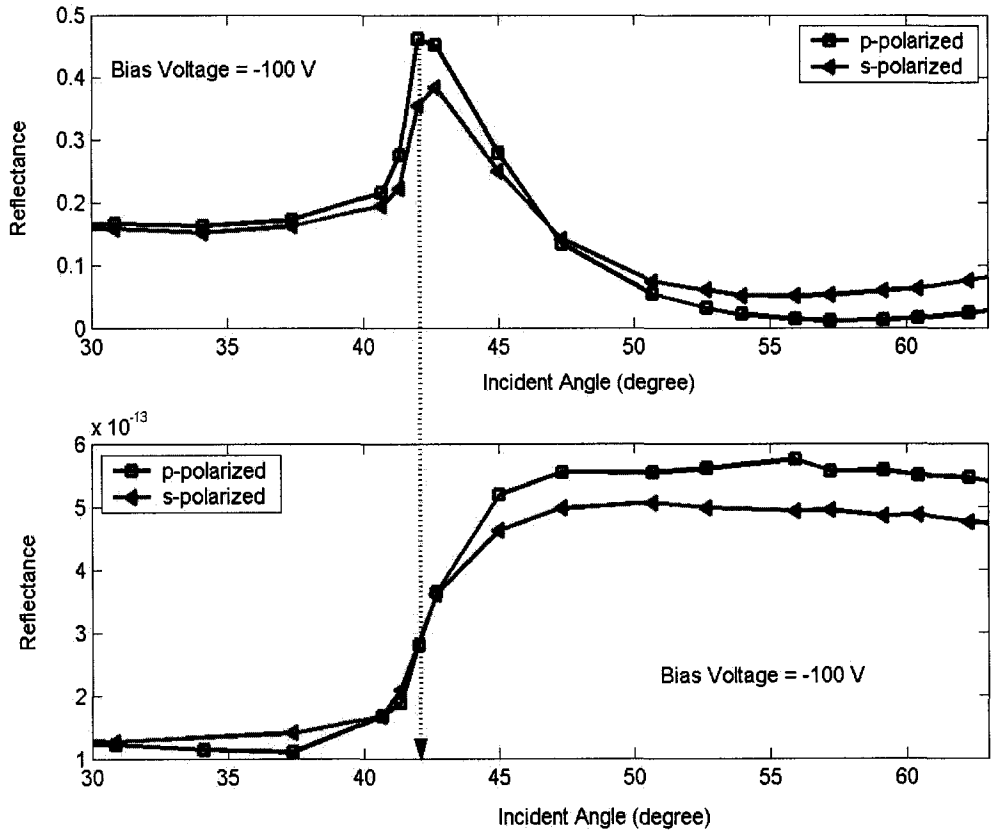

Figure 3.12. The upper figure shows the reflectance as a function of incident angle measured in the Kretschmann-Raether configuration with both s- and p-polarized 266 nm microlaser. The thickness of the gold film was 20 nm. The photoelelctron signal as a function of incident angle of the laser light for 20-nm gold film is in the lower figure. The arrow indicates the critical angle.

importantly, the 266-nm wavelength light raises interesting questions about the coupling between the surface and interface resonance as well as transport of electrons.

Figure 3.13 shows the influence of the bias voltage applied between the thin gold film and the collecting electrode, on the free electron signal, for angles of incidence above and below the critical angle, at constant nitrogen flow rate. This experiment was conducted with the same setup as that in Section 2.3.2. A 500 mL/min nitrogen flow rate was initiated several minutes before data collection began in order to remove the contaminants in the tubing system. Eleven 50-shot average waveforms were acquired at voltage settings of 0 V, - 50 V, - 100 V, - 200 V, - 300 V, - 400 V, - 500 V, - 600 V, 700 V, - 800 V, and - 900 V. Voltages were measured with a digital multimeter. The number of photoelectrons calculated by integrating the free electron current appears in Figure 3.13. The curve indicated with circles is the variation of the number of photo-emitted electron with bias voltage beyond the critical angle while the dot-square curve reveals how the number of photo-emitted electrons changed with bias voltage before the critical angle.

Figure 3.13 also demonstrates that the photo-emitted electron signals captured by the collecting electrode at the angle of 47.3 ° (greater than the critical angle) is about 5 times those at the angle of 37.4 ° (less than the critical angle) at each bias voltage. Although the reason for this enhancement is unknown, a possible explanation, as discussed above, might be due to the penetration depth of the evanescent wave into the metal, that is about 25 nm in the gold film, to assist the electrons to escape.

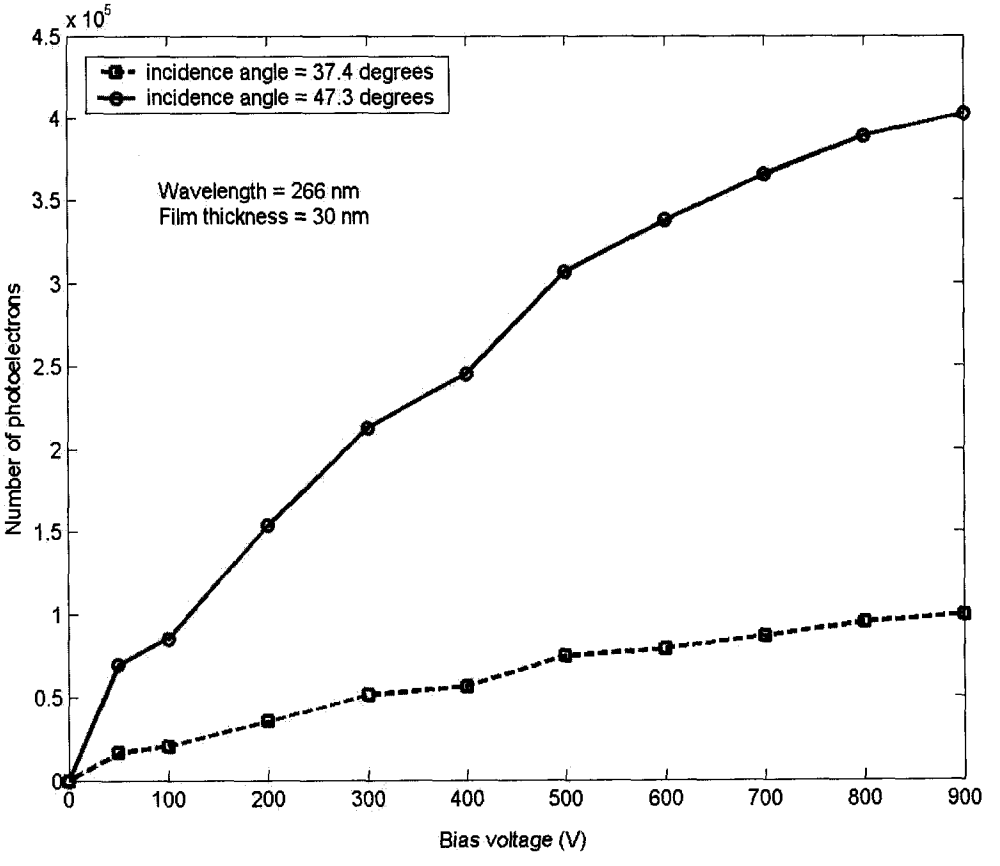

Figure 3.13. Photoelectron signal received by the detector as a function of bias voltage.

The final experiment examined the effect of different drift gases on the electron signal and was performed by the previous experimental system. Figure 3.14 shows that the photo-emitted charge with the argon drift gas is 2.5 times as much as that obtained using nitrogen as the drift gas, and thus, using argon gas as a drift gas might be a better option in terms of the sensitivity of IMS. On the other hand, the experiments in Chapter 4 will show that, in order to get a better separation of IMS spectra, the bias voltage applied to the drift tube is in the range of from - 2000 V to - 2500 V. When the bias voltage increased to - 1500 V, there was arcing between the thin gold film and the collecting electrode with the argon drift gas. Therefore, argon gas is not used as a drift gas in this work.

It is worth pointing out that, in this study, the 532-nm wavelength laser irradiated a thin gold film, but no electron emission signal was detected. The work function of Au is about 4.2 eV;[82] theoretically, a two-photon process is adequate to eject an electron from a thin gold film by using a 532 nm laser.

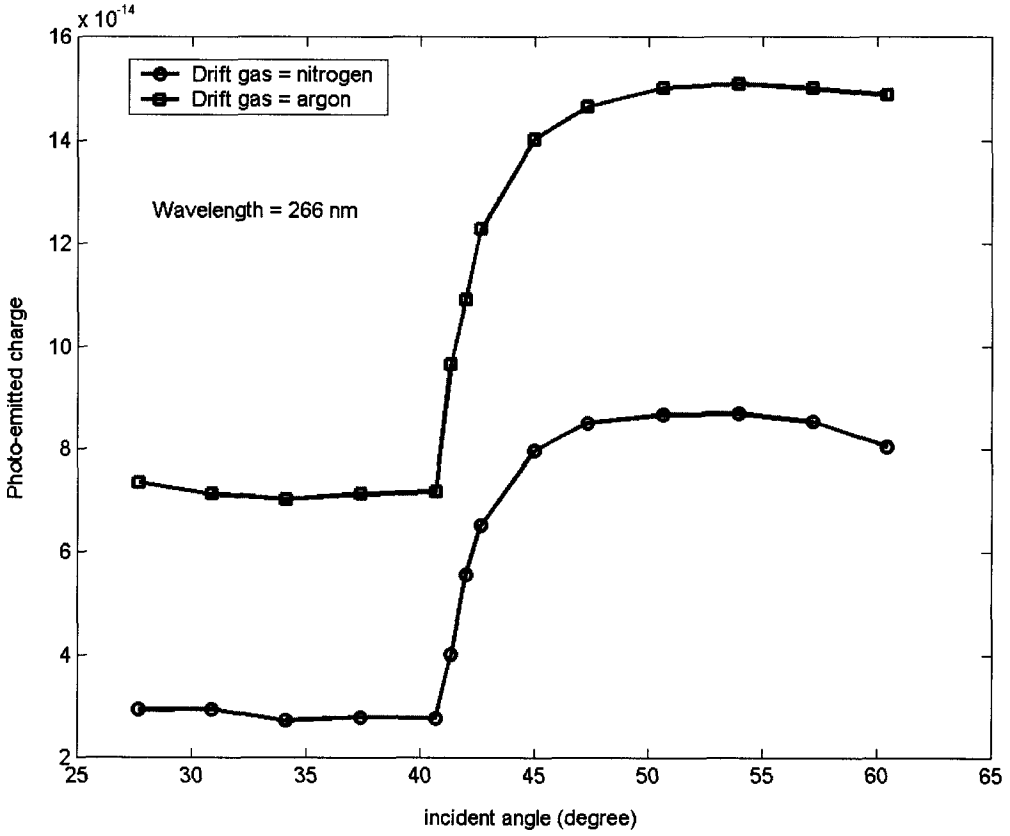

Figure 3.14. Total photoelectrons emitted by the 20-nm thick gold film collected as a function of incident angle in nitrogen and argon at a flow rate of 900 mL/min.

CHAPTER 4

DETECTION OF CHLORIDE IONS AND NITRO-ORGANICS IN AMBIENT AIR

4.1. IMS Instrumentation

A schematic diagram of our experimental apparatus is shown in Figures 4.1 and 4.2. The IMS system is comprised of three main parts: (1) a photoemissive ionization source, for generation of free electrons; (2) a drift tube, for separation of ions; and (3) the aperture grid and collecting electrode for detection of ions. Each of these components is described in detail below. A brief overview of the experimental sequence is as follows.

The photoemissive source was a gold-coated fused silica window mounted in a window holder. The fused silica window was a circular disk that is 12.7 mm in diameter and 2 mm in thickness, or a 12.7 mm × 12.7 mm × 12.7 mm equilateral prism (ESCO Products, Inc., Oak Ridge, NJ). The 25.1 mm diameter by 5.1 mm thick window holder was fabricated by machining either a central square-shaped 12.7 mm × 12.7 mm or circular 12.7 mm diameter hole to hold the windows as shown in Figure 4.3. The window was held in place with a setscrew. The electrical contact between the window holder and the gold coating was made with indium soldering. The thickness of the thin gold film used was 20 nm. The photoemissive ionization source was mounted on the front end of the cell housing the drift tube as shown in Figure 4.1. Free photoelectrons were produced by back-side illumination of the gold surface with ultraviolet light as shown in Figure 4.4. When a bias voltage was applied between the thin gold film and the first electrode of the drift tube, free electrons moved towards the drift tube and had a huge number of collisions with the air molecules.

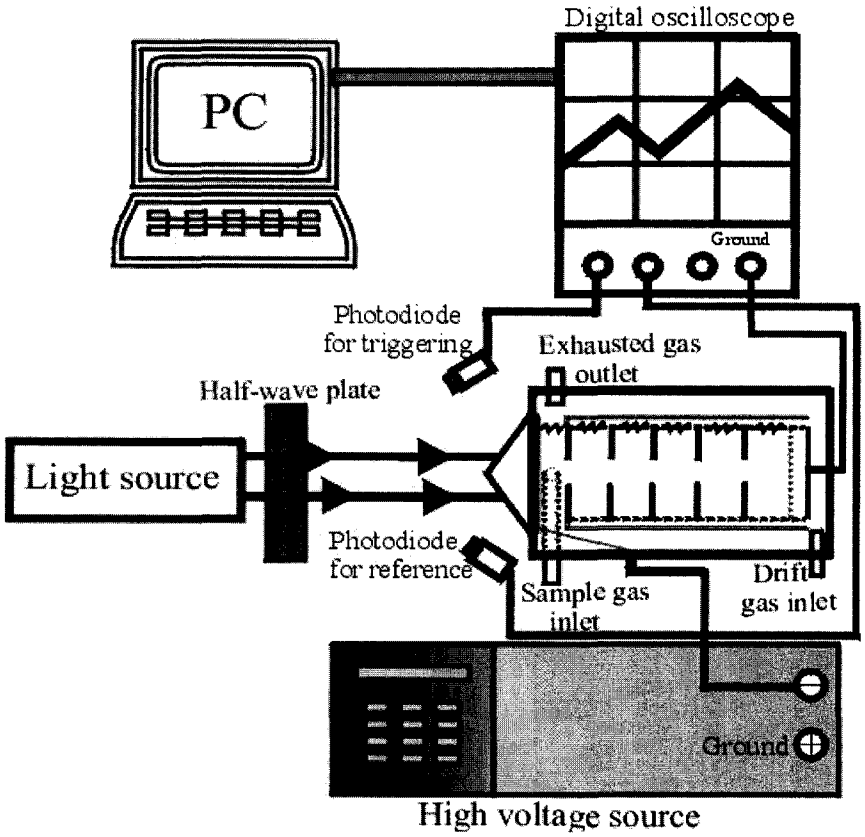

Figure 4.1. A schematic of IMS experimental setup.

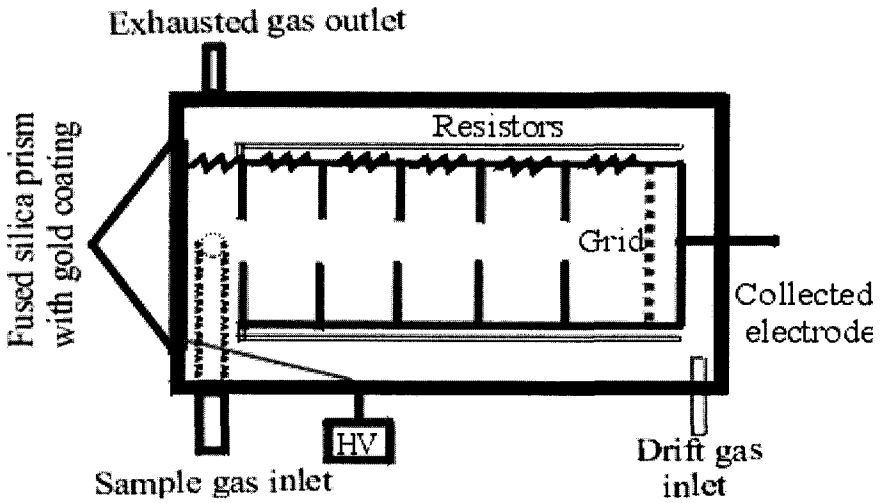

Figure 4.2. A schematic of the cell housing the drift tube.

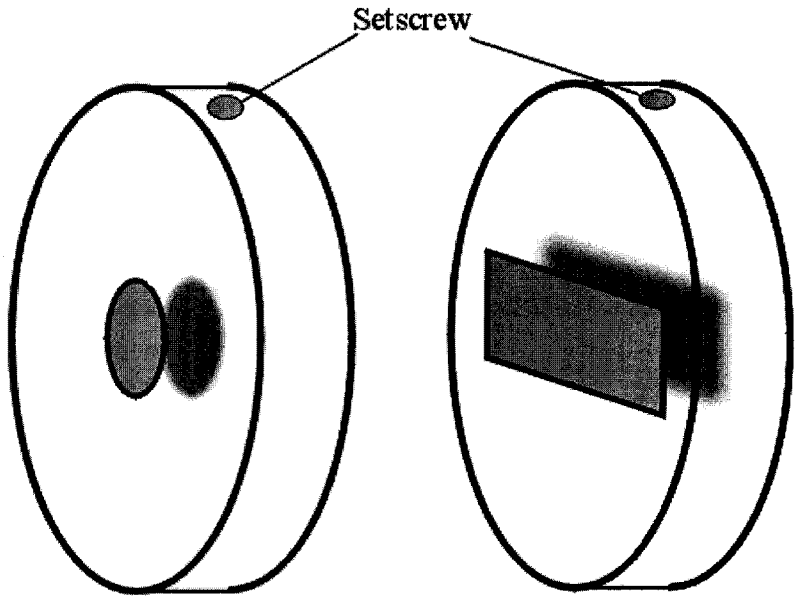

Figure 4.3. A schematic of window holders.

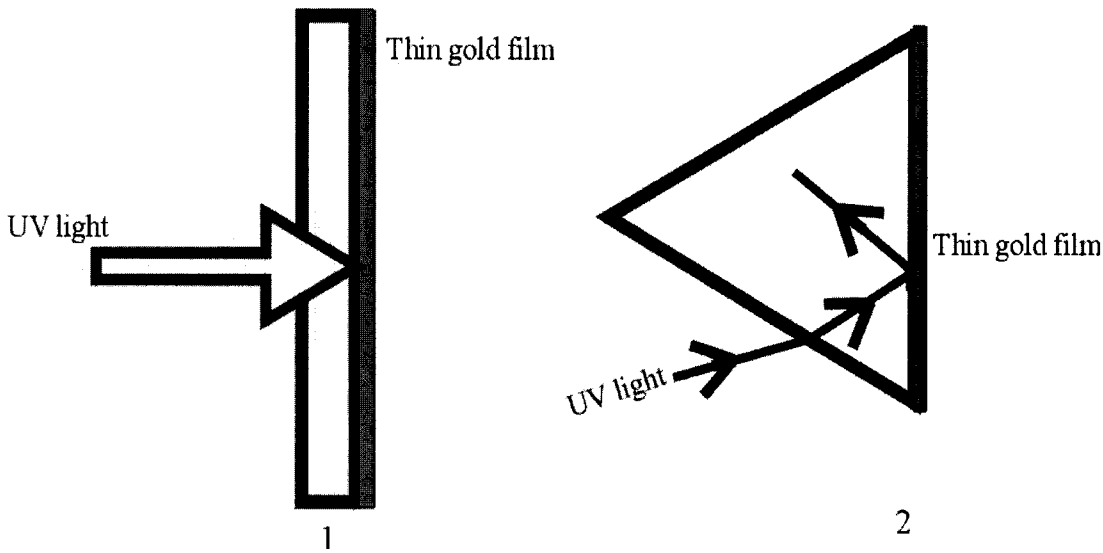

Figure 4.4. The back-side illumination by ultraviolet light on (1) a circular flat fused silica window and (2) an equilateral prism.

Ions were created by free electron attachment to neutral molecules. The product ions depended on the drift gas.[16,83,84] The drift gas was either ultra pure nitrogen gas or breathing-grade air. If ultra pure nitrogen gas was used as the drift gas, the product ions were low-energy free electrons obtained from photoemission; otherwise, they were oxygen molecular ions.

The drift tube shown in Figure 4.5 was composed of a stack of brass guard rings, and the total length of the drift tube was 3.59 cm. A uniform electric field was generated along the axis of the drift tube by five 0.3-mm thick brass drift guard rings separated by 0.717-cm thick ceramic spacers. Three holes distributed equatorially about the axial aperture were used to mount the guard rings on 3/16-inch glass rods. A commercial aperture grid (Graseby Dynamics, Ltd., Watford, UK) was separated in a ceramic mount by 0.82 mm from the 2-cm diameter copper anode. The drift axis was aligned with the center of the photoemissive surface. The drift tube was sealed in a 31.0-mm diameter and 152.8-mm long cylindrical, stainless steel tube in order to contain the drift gas. The output of a Fluke 412B high voltage supply connected directly to the photoemissive source at the front of the drift tube through a 2.0-m long cable is shown in Figure 4.1. The PE source, the drift tube, and oxygen-free high-conductivity (OFHC) copper collector electrode were housed in the 2.75-inch stainless steel conflat flange-90° mitred elbow.

A voltage divider consisting of a chain of 360-kΩ resistors provided the potentials for the drift guard rings. At the end of the drift tube was a collector electrode separated from the aperture grid by 0.082 cm. The separation between the first guard ring of the drift tube and the thin gold film was 0.45 cm. After traveling through the drift tube, ions exit through the aperture grid and then strike the OFHC copper collecting electrode.

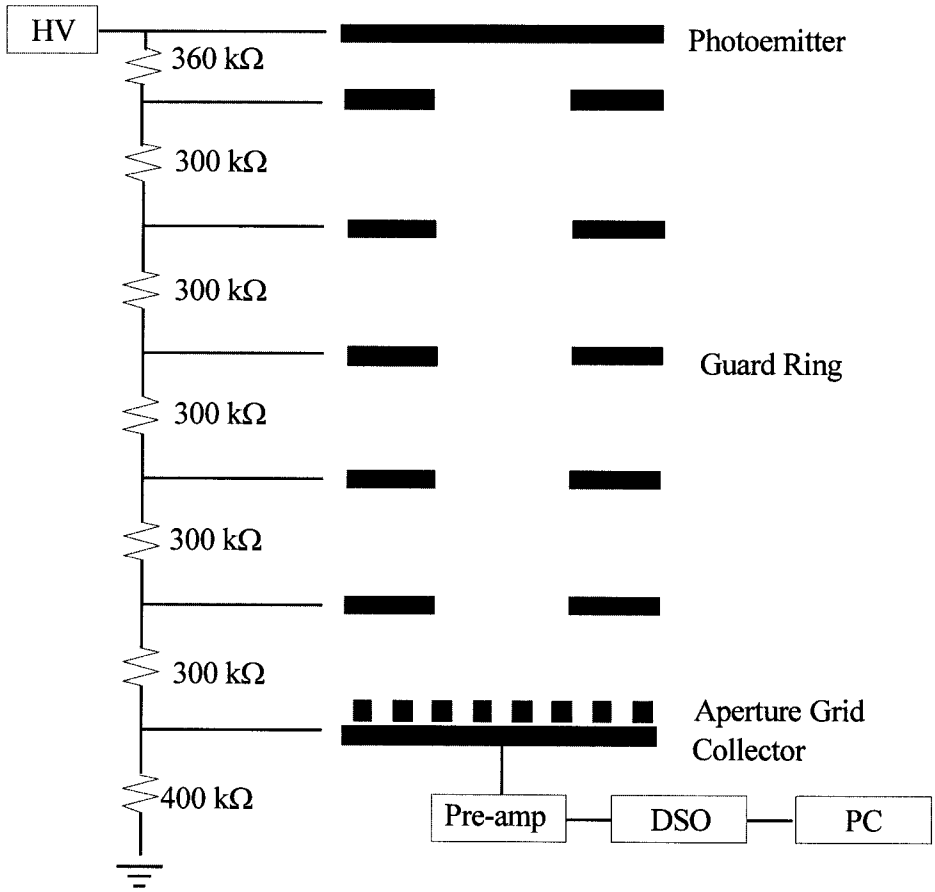

Figure 4.5. A schematic diagram of the drift tube.

There were two different configurations carrying sample gases into the PE-IMS system. In detecting TCE or methylene chloride in air or nitrogen, a long stainless steel tube delivered carrier gas (nitrogen or air) to the bottom of a sealed 5-L, round-bottomed glass flask while a shorter tube extracted mixed gas from the center of the flask. A gas mixture of known analyte concentration was prepared by injecting a known volume of analyte liquid into a sealed 5-L, round-bottomed glass flask with a 50 μL or 10 μL syringe.

Alterations to the gas supply line were necessary to deliver vapors of nitroaromatic compounds (explosives), solids of very low vapor pressure at room temperature at ambient pressure, to the PE-IMS. A 0.25-inch Swagelok tee was placed in the gas delivery line, and a Swagelok cap on the base of the tee served as the sample vessel as shown in Figure 4.6. Several granules of the analyte solid sample (p-nitrotoluene; 2, 4-dinitrotoluene; or 2, 6-dinitrotoluene) were placed in the Swagelok cap. The cap with an analyte or several analytes was attached to the bottom of the tee. The cap was lowered into a beaker containing 800 mL of softly boiling water to melt the solid and increase its vapor pressure. The carrier gas, ultra pure nitrogen gas, or breathing-grade compressed air was flowed through the tee, carrying the gas-phase analyte molecules to the ionization region of the PE-IMS.

The fourth harmonic of a Continuum Nd:YAG Surelight II laser was delivered onto the thin gold film to produce free electrons. The laser was operated at a 10 Hz repetition rate to deliver pulses of approximately 5-ns temporal width. The pulse energy was about 230 μJ. A Tektronix TDS 620A digital storage oscilloscope was triggered by a photodiode that monitored scattered laser light. Pulse energy data were acquired using a Molectron pyroelectric detector (J9LP-1) at the beginning of the experiment. Prior to data acquisition,

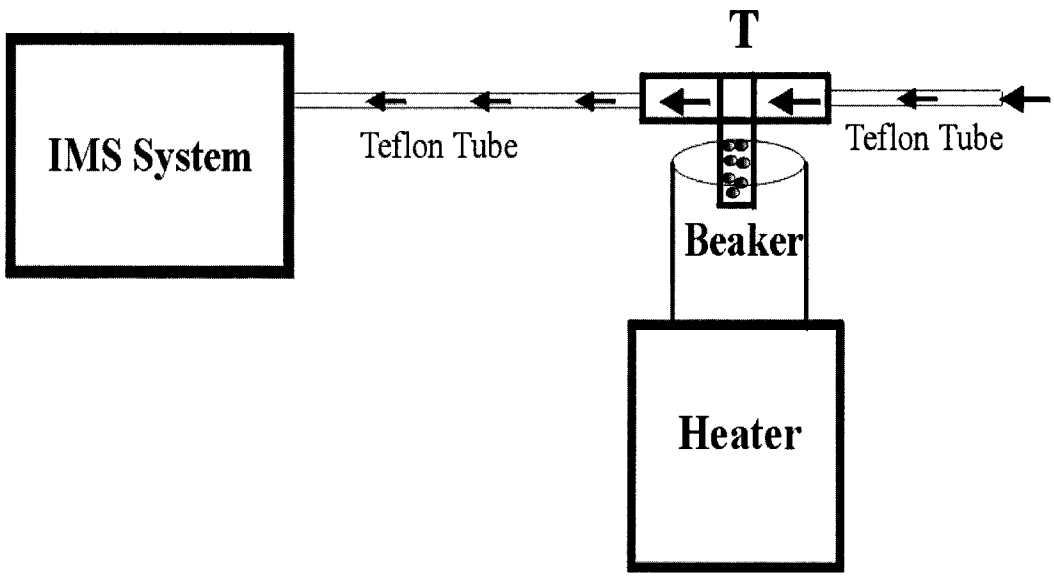

Figure 4.6. A schematic of tee configuration.

the Nd:YAG laser was warmed for about 60 min while ultra pure nitrogen gas was flushing the tubing system and drift tube to remove contaminants.

In all configurations, the current due to the movement of ions in the volume between the aperture grid and the collecting electrode was amplified 10^8 $V \cdot A^{-1}$ by a pre-amplifier and then fed into a Tektronix TDS 540 or 620A digital storage oscilloscope as shown in Figure 4.1. An HCA-10M-100k-C model high speed amplifier with 10^5 V/A amplification was substituted for the pre-amplifier to detect the free electron waveforms. A program written in C++ controlled data acquisition, downloaded binary waveforms from the Tektronix TDS 620A digital storage oscilloscope through a GPIB card, translated binary data to ASCII data, and then saved the data as files in the controlling computer. Nd:YAG laser energy was measured by using the Molectron pyroelectric detector at the beginning of the experiment. To compensate for the large electrical noise and the large fluctuations in laser output, acquisition averaging at least 20 and as many as 125 laser shots with the record length of 500 sample points was required.

4.2. Chemicals and Solvents

The chemicals used in this study were 2, 4-dinitrotoluene (2, 4-DNT); 2, 6-dinitrotoluene (2, 6-DNT); p-nitrotoluene (p-MNT); and m-dinitrobenzene purchased from Chem Service Company (West Chester, PA). Solvents used were methylene chloride, photometric grade TCE (Aldrich), and spectrophotometric grade cyclohexane; and were purchased from Aldrich Chemical Company, Inc. (Milwaukee, WI). One microliter neat liquid TCE or methylene chloride were diluted with 1 mL HPLC grade non-electronegative cyclohexane solvent.

4.3. Calculations

4.3.1. Reduced Ion Mobility

All reduced ion mobility values, K_0, were calculated using Eq. 4.1 [85,86] as follows:

$$K_0 = \frac{v}{E} \times \left(\frac{p}{760}\right) \times \left(\frac{273}{T}\right) = \frac{L}{E \times t} \times \left(\frac{p}{760}\right) \times \left(\frac{273}{T}\right), \qquad (4.1)$$

where L is the length of the drift tube (3.59 cm), E is the magnitude of the drift field (372.4 V/cm), t is the drift time, v is the drift velocity, K_o is reduced ion mobility in $cm^2 \cdot v^{-1} \cdot s^{-1}$, p is atmospheric pressure (750 torr), and T is the temperature of the drift tube (298 K). The length, L, was measured from the first electrode of the drift tube to the collector.

When -2000 V was applied to the PI source, the resistors maintained a 372.4 V/cm electric field along the axis of the drift tube, a 4341 V/cm electric field magnitude between the aperture grid and the collector electrode, and a 712 V/cm electric field magnitude between the first ring and the thin gold film.

4.3.2. Relationship Between Concentration and Dilution Time

The concentrations of both methylene chloride and TCE in the carrier gas (ultra pure nitrogen gas) slowly decrease by exponential dilution with time. The concentration of analyte in the gas exiting the 5 L flask is given by [87]

$$\log(c) = \log(c_0) - \left[\frac{t \times Q}{2.303V}\right], \qquad (4.2)$$

where c is the analyte concentration in the exiting gas, c_0 is the initial analyte concentration, V is the volume of the flask, Q is the constant flow rate of gas through the chamber, and t is the duration of the gas flow.

4.3.3. Integrating an Ion Current over Time

Integration of an ion current over time was done to calculate the number of ions reaching the collecting electrode. This integration was performed using Matlab software to sum discrete current values and then multiply by the time increment between data points in the waveform of the ion current:

$$Q = \left(\sum I_n\right)\Delta t \quad , \qquad (4.3)$$

where Q is the total charge in Coulombs; Δt is the time increment; and $\sum I_n$ is the sum of current values, I_n, between times t_i and t_f of the ion current waveform.

4.4. Procedures

The gas-phase analytes were carried by a carrier gas (either ultra pure nitrogen or breathing air) to the ionization region in the PE-IMS to be ionized. Under the influence of the electric field, the negative ions resulting from low-energy electron attachment or interaction between reactant anions and the sample vapors traveled through the drift tube, passed through the aperture grid, and then struck the collector electrode. Because the separation between the aperture grid and the collector electrode was very small (The distance between the aperture grid and the collector electrode is 0.082 cm.), a sharp, induced current peak was created. Measurements of the drift times of the anions formed upon low-energy electron attachment permitted the identification of individual species. At ambient pressure in air or nitrogen, ions obtained stable, characteristic drift velocities due to collisions with gas molecules. If instrument resolution was sufficient, these packets of single ion species arrived separately at the collector electrode.

In order to increase the resolution of ion mobility spectra, counterflowing drift gas that limited analyte vapor to the space immediately before the ionization source was used. Because counterflowing drift gas effectively confined all ionization chemistry to the start of the drift tube, it prevented broadening of signatures and signature overlap that could occur due to the presence of analyte ion and oxygen ion production throughout the drift space. The PE-IMS was operated at room temperature and atmospheric pressure.

Prior to introduction of analyte vapor into the IMS system, the ion mobility cell was flushed with slowly flowing nitrogen at the flow rate of 300 mL/min in order to keep the drift tube and tubing system from being contaminated, and at the same time, the 5 L flask was evacuated for an hour to remove the residual gas mixtures in the flask. The rate of the counter-flowing gas traveling through the drift tube was set to be about 900 mL/min. The counter-flowing gas used was ultra pure nitrogen gas. Each of these tubes was fitted outside the flask with valves such that the chamber can be isolated during preparation of the gas mixture.

Either ultra pure nitrogen or breathing-grade air flowed into the 5 L flask until it was full, and then, the two valves of the flask were closed. A certain amount of an analyte was injected to the flask. After completely mixing, carrier gas flowed at a constant flow rate through the flask into the PE-IMS system.

4.5. Results and Discussion

4.5.1. Comparison of the Free Electron and Ion Signals Before and After the Critical Angles

Figure 4.7 compares the photoelectrical signal that was generated from a 20-nm gold film irradiated with the fourth harmonic of a 10 Hz Nd:YAG laser (266-nm) at an incident angle of 37.4° (less than the critical angle of 41.8°) with that at an incident angle of 47.2°

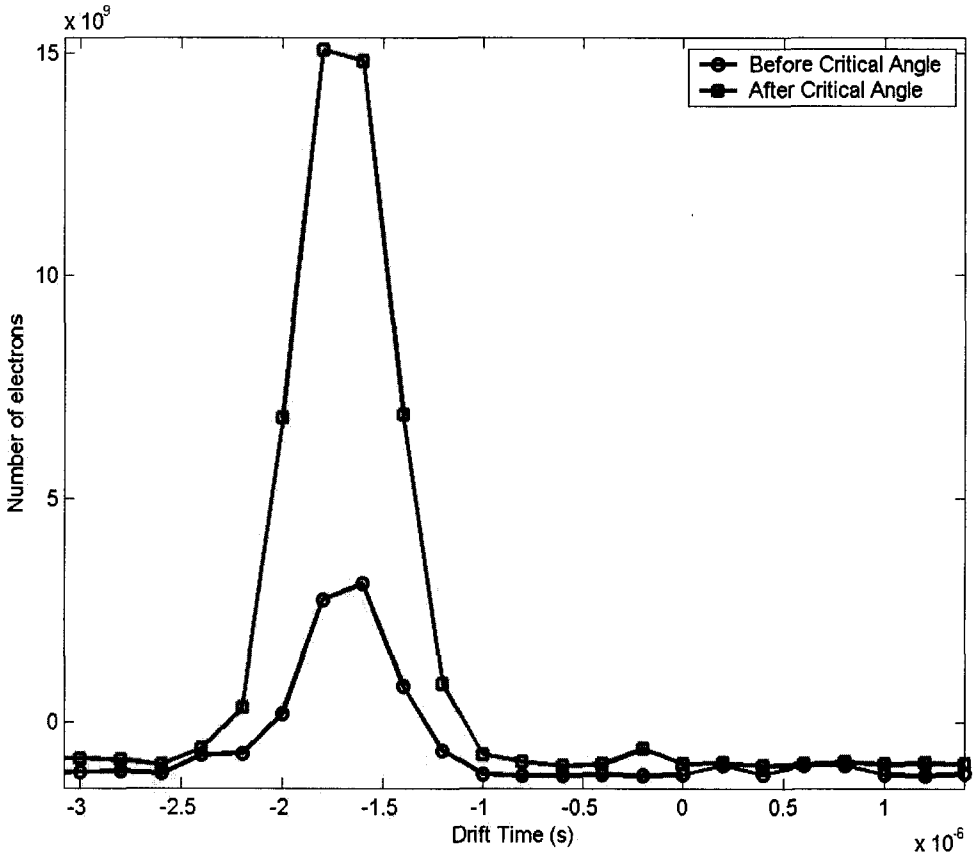

Figure 4.7. The photoelectric yield before and after the critical angle.

(greater than the critical angle). The drift gas was ultra pure nitrogen (Praxair, Inc.), and the flow rate was 900 mL/min. Integrating the area under the peaks gives a quantitative answer that the number of the free electrons at the incident angle of 47.2° is 4.93 times that at the incident angle of 37.4°. Beyond the incident angle of 47.2°, the number of free electrons stays almost the same as that at 47.2° shown in Figure 3.15.

A plot of IMS spectra generated by the low-energy electron attachment to nitrobenzene and TCE at room temperature and atmospheric pressure in air appears in Figure 4.8. This figure shows that the ion signal at 47.2° is about 5 times that at 37.4°.

From Figure 4.8, it is also seen that the nitrobenzene ion current (associative electron attachment to nitrobenzene molecules to form the parent negative ions) appears at the incidence angle of 47.2° while the nitrobenzene ion signal is not detectable above the noise level at 37.4°. In other words, changing the angle of ultraviolet light incident on the gold-coated surface beyond the critical angle causes a large enhancement of the number of photo-emitted electrons. This enhancement provides more opportunities for gas-phase analyte molecules to capture electrons to form negative ions and, therefore, increases IMS sensitivity.

4.5.2. Detection of TCE and Methylene Chloride Vapors in Nitrogen and Air

Extensive studies of electron attachment phenomena and the mechanism of how a single low-energy electron attaches to a TCE as well as a methylene chloride molecule giving rise to a chloride ion and a neutral molecule already exist. These previous results showed that, as a class, chlorinated aliphatic compounds undergo dissociative capture of slow electrons to yield the chloride ion, Cl^-, and a molecular neutral fragment.[88]

$$e^- + CH_2Cl_2 \rightarrow Cl^- + CH_2Cl\,. \qquad (4.4)$$

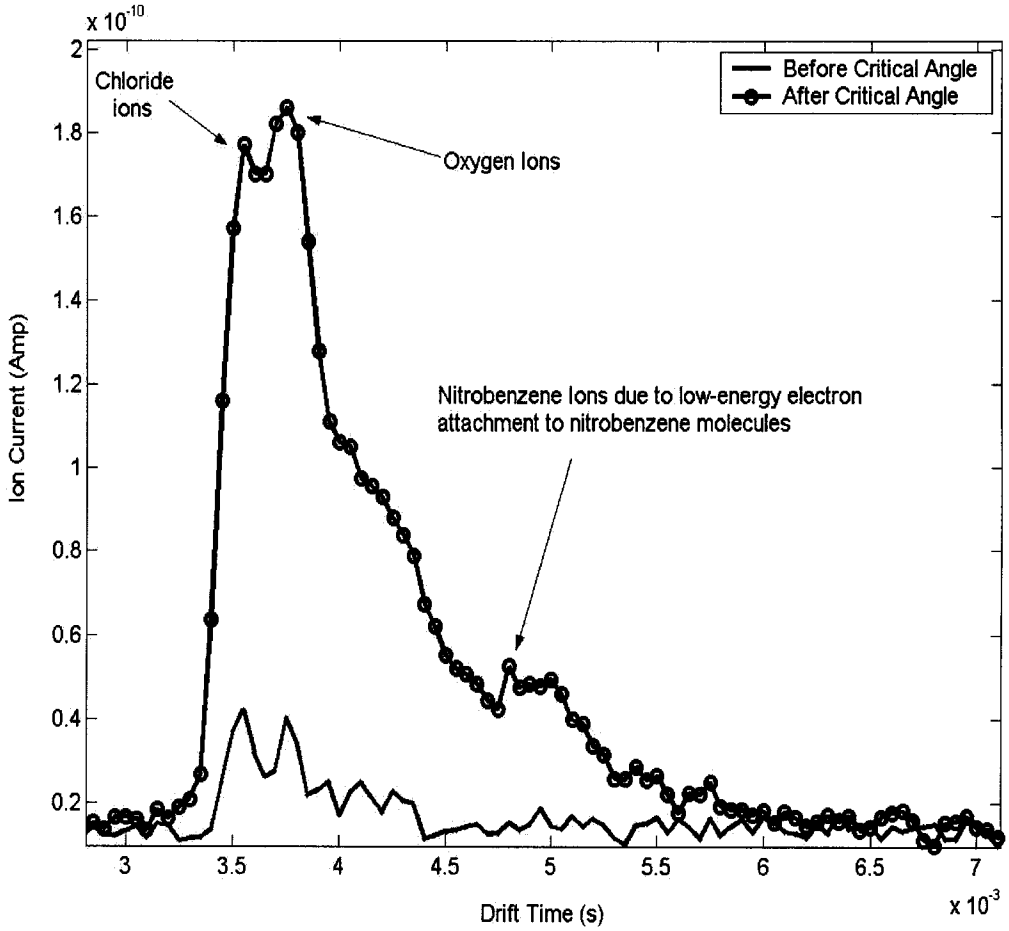

Figure 4.8. IMS spectra of a TCE and nitrobenzene mixture gas resulting from electron attachment in air generated at the incident angles of 37.4° (less than the critical angle) and 47.2° (greater than the critical angle).

4.5.2.1. TCE and Methylene Chloride Concentration Plots

The response of the PE-IMS to TCE and methylene chloride embedded in ultra pure nitrogen carrier gas was evaluated. An exponential dilution mixture of either methylene chloride or TCE in nitrogen was used to supply a range of TCE or methylene chloride concentrations to the sensor. Exponential dilution is a convenient, straightforward method for producing the range of analyte concentrations necessary to find the limitation of the IMS. A gas mixture of known analyte concentration was prepared by injecting a known volume of analyte liquid or vapor into a 5 L flask containing an inert carrier gas (diluent gas). After complete mixing, additional diluent gas was flowed steadily through the chamber, causing the analyte concentration in the gas exiting the chamber to fall exponentially with time.

The 5 L flask filled with only ultra pure nitrogen gas was first analyzed by the IMS system to ensure that it contained an acceptably low amount of contaminants in the flask and tubing system. A 10-μL neat methylene chloride or 200-μL diluted TCE liquid sample was injected with a 50-μL liquid syringe into the 5 L flask filled with ultra pure nitrogen. After a 1-hour delay to allow evaporation and mixing of the analytes, diluted ultra pure nitrogen gas was flowed through the flask at the rate of 28 mL/min, and PE-IMS was initiated. Data collection began immediately. Single 50-shot average waveforms were collected at timed intervals at nearly 2 hours for methylene chloride and about 1.5 hours for TCE while maintaining a constant flow rate of both the carrier and the drift gases (ultra pure nitrogen, 28 mL/min). The number of chloride ions detected versus dilution time is presented in Figures 4.9 and 4.10. An exponential fit was done on the collected data and is also plotted.

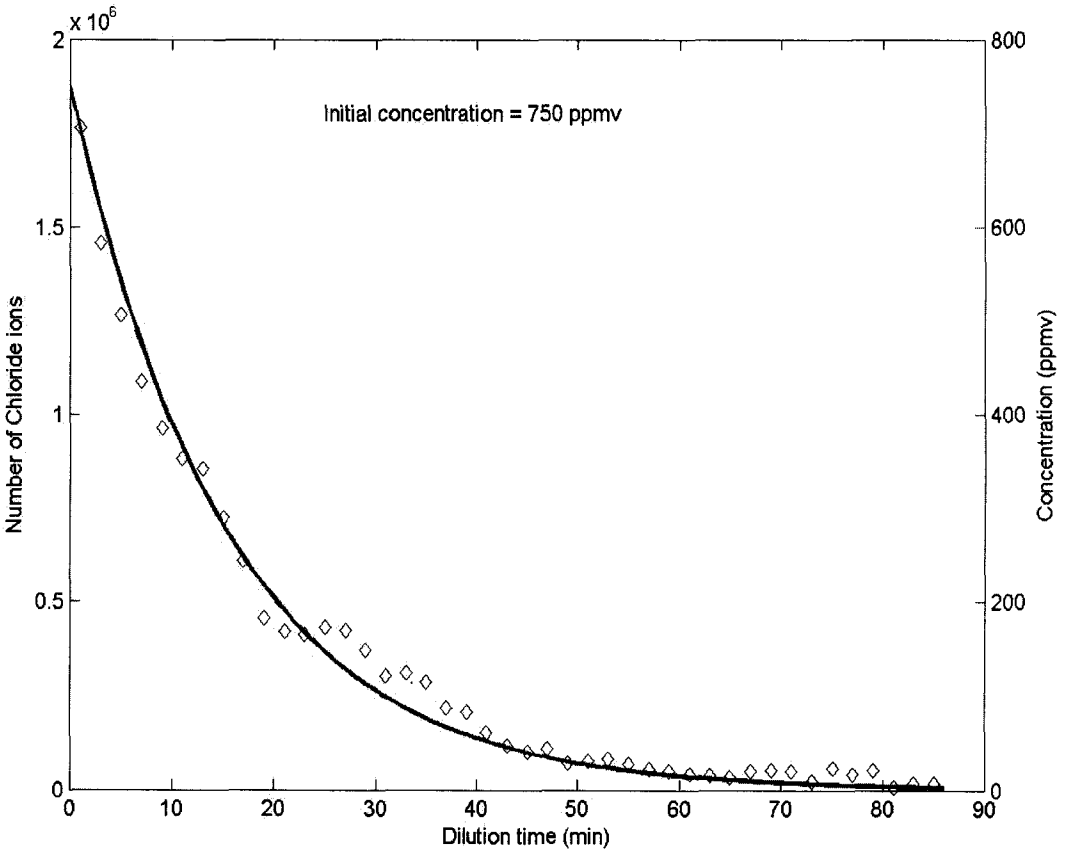

Figure 4.9. Curve of methylene chloride concentration versus time during exponential dilution of a 5 L mixture of 750 ppmv methylene chloride in nitrogen at a dilution flow rate of 28 mL/min of nitrogen.

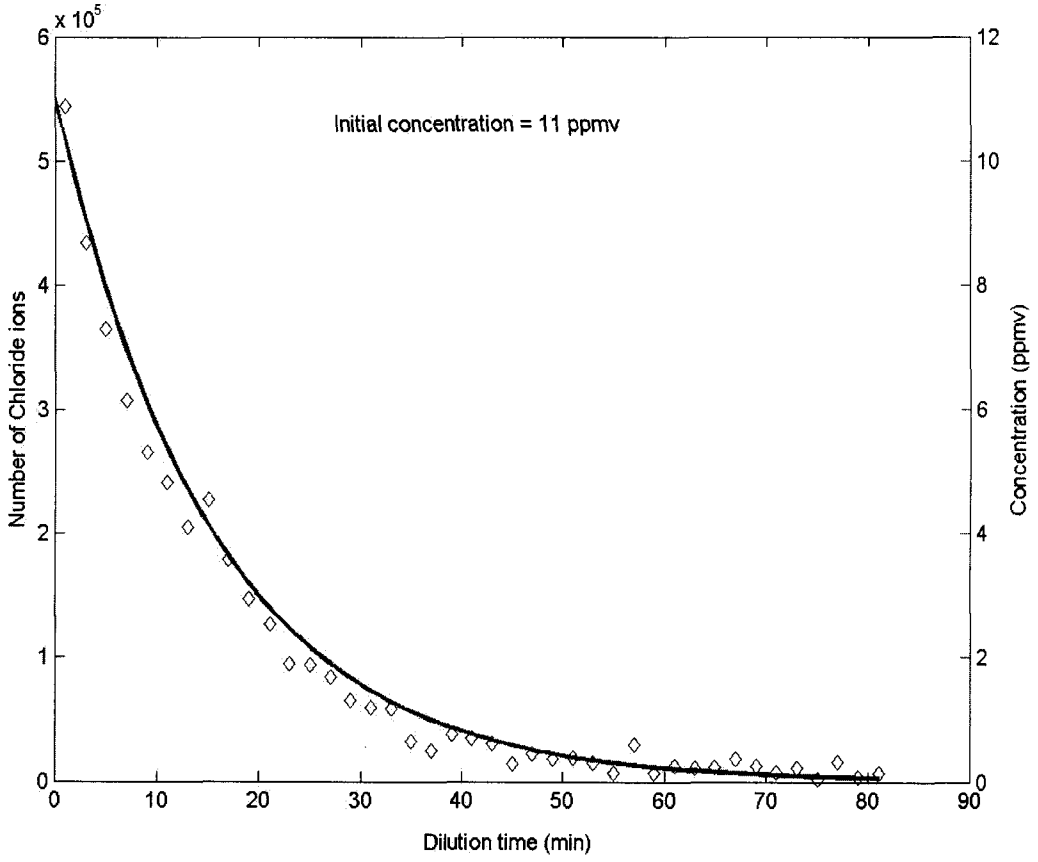

Figure 4.10. Curve of TCE concentration versus time during exponential dilution of a 5 L mixture of 11 ppmv TCE in nitrogen at a dilution flow rate of 28 mL/min of nitrogen.

The final experiment in this section measured how the free electron signal in nitrogen changed with the dilution time due to the electron attachment to TCE. As the experiment was run immediately after the previous experiment, the system was completely warmed and conditioned. The bias voltage remained at - 2000 V. The flow rates of the drift gas (nitrogen) and the carrier gas (nitrogen) were 900 mL/min and 28 mL/min, respectively. The number of free electrons collected versus the dilution times appears in Figure 4.11. The data show that the free electron signal area increases exponentially with the dilution time.

4.5.2.2. Ion Mobility Spectra of TCE and Methylene Chloride in Nitrogen and Air

The ECD (electron capture detector) strongly responds to vapors of chlorinated species, such as methylene chloride and trichloroethylene (TCE),[88,89] that release chloride ions upon attachment of low-energy free electrons. Experiments were performed to detect TCE and methylene chloride at room temperature and ambient pressure in air. Neat methylene chloride in the amount of 10 μL was injected with a 50 μL syringe. An amount of 200 μL diluted TCE liquid was injected using a 50 μL syringe and allowed to mix with either breathing-grade air or ultra pure nitrogen gas in the 5 L flask while the inlet and outlet valves on the flask were closed. After 60 min for the methylene chloride or TCE to evaporate and mix evenly with the carrier gas, a series of three 50-shot averaged waveforms were collected in succession by the Tektronix 620 oscilloscope.

Figures 4.12 and 4.13 show the ion mobility spectra of 750 ppmv methylene chloride and 11 ppmv TCE in air compared with those of the same amounts of methylene chloride and TCE in ultra pure nitrogen. The electron capture events of either methylene chloride or TCE occur near the photoemitter.

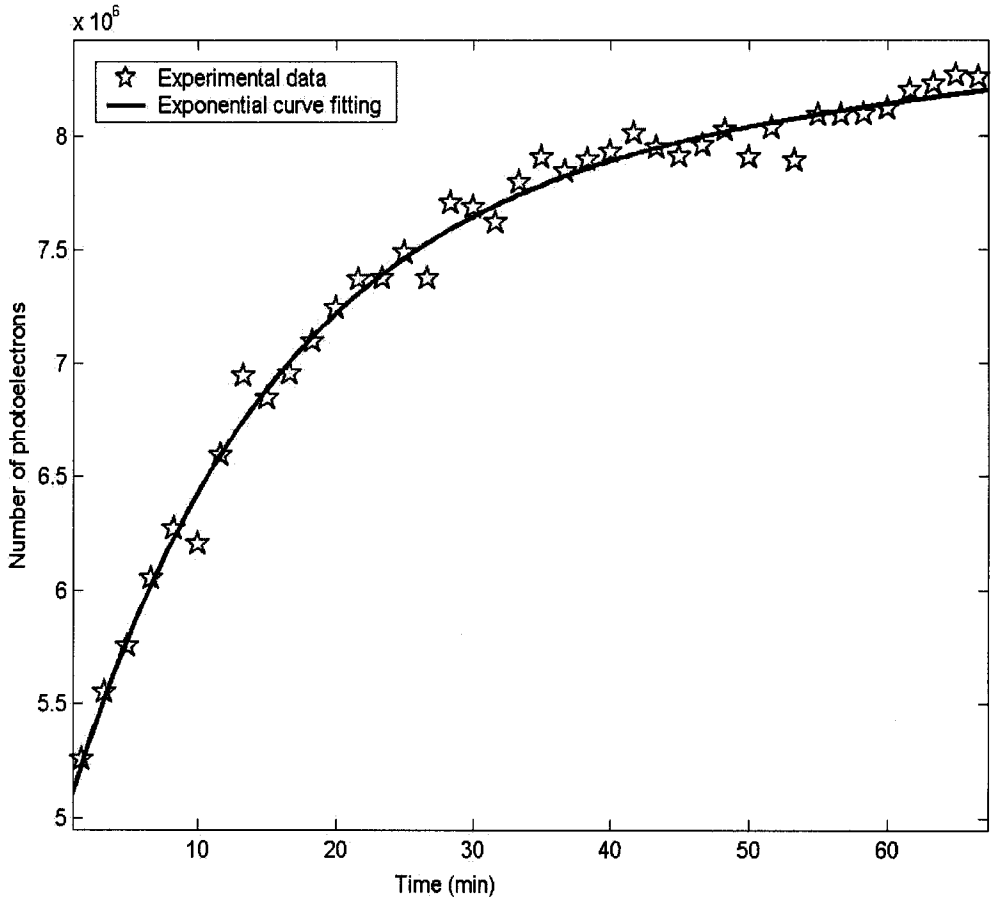

Figure 4.11. Curve of the number of free electrons versus time during exponential dilution of a 5 L mixture of 11 ppmv TCE in nitrogen at a dilution flow rate of 28 mL/min of nitrogen.

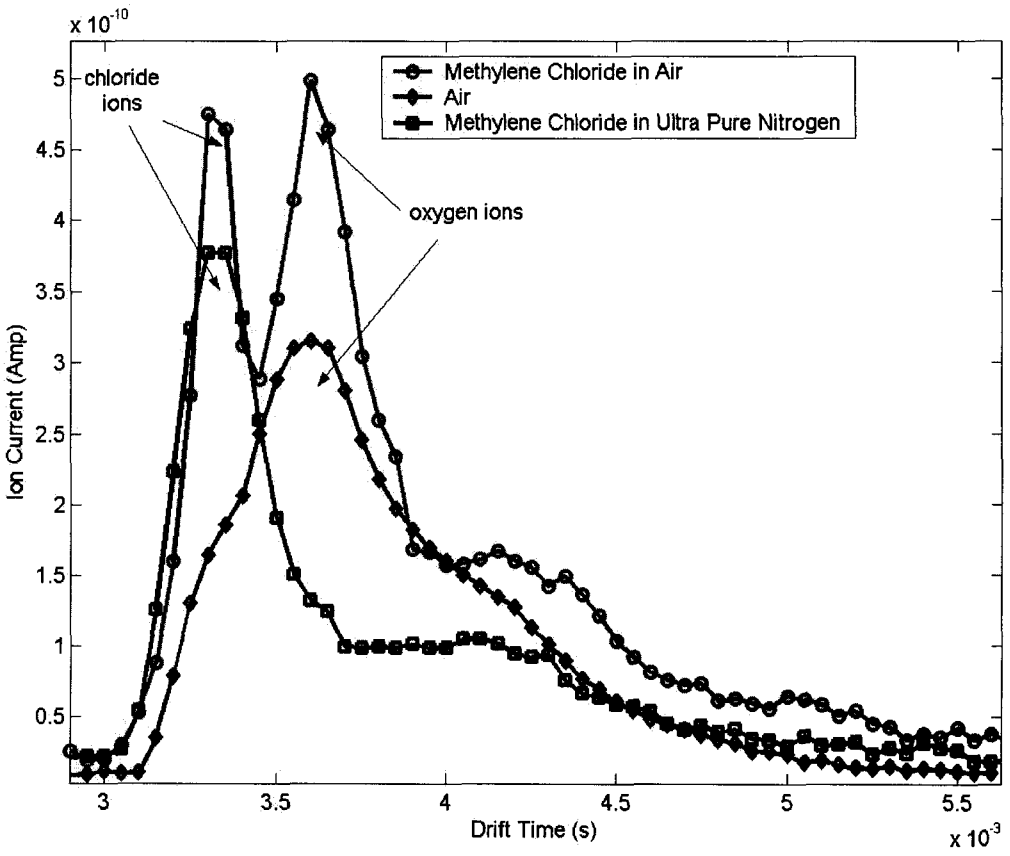

Figure 4.12. Ion mobility spectra of methylene chloride generated from 750 ppmv methylene chloride in either nitrogen or air.

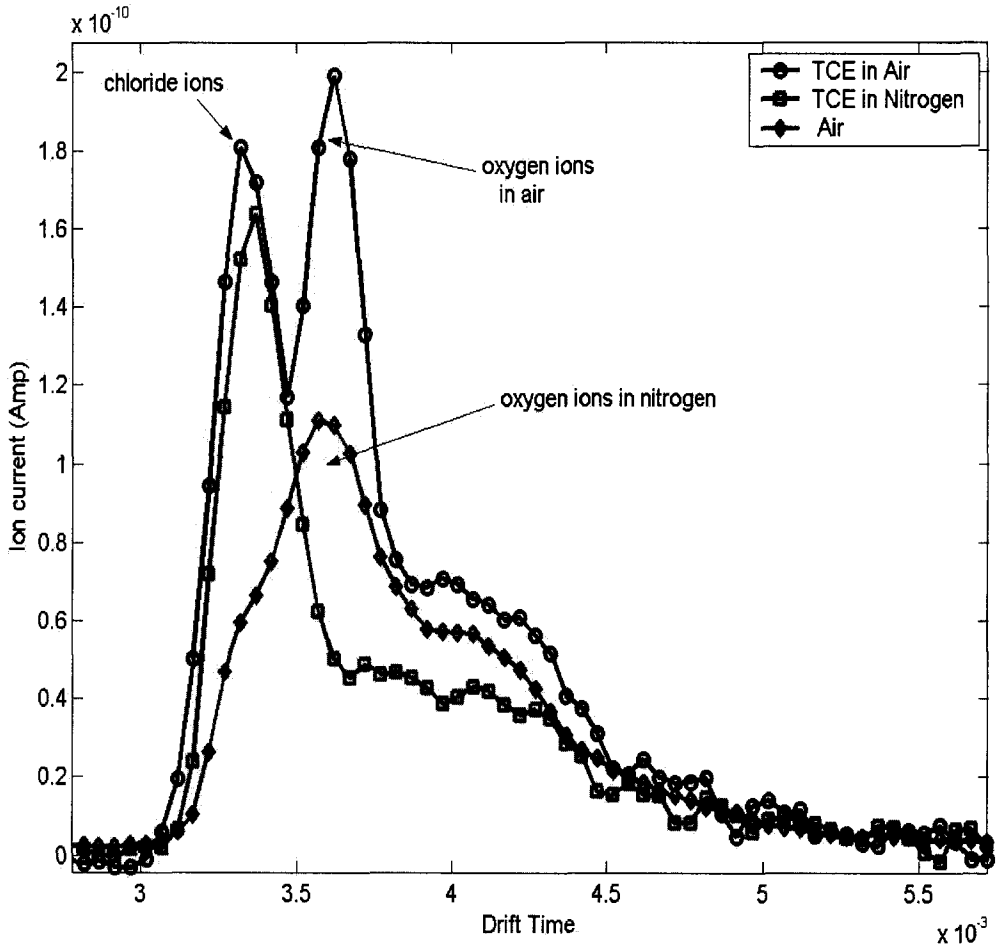

Figure 4.13. Ion mobility spectra of chloride and oxygen ions generated from 11 ppmv TCE in either nitrogen or air.

Eq. 4.1 leads to reduced ion mobilities (K_0) of 2.45 $cm^2 V^{-1} s^{-1}$ and 2.64 $cm^2 V^{-1} s^{-1}$ for the oxygen ion peak and chloride ion peak shown in Figures 4.12 and 4.13. These two values are lower than literature values of 2.5 $cm^2 V^{-1} s^{-1}$ (oxygen ions) and 2.94 $cm^2 V^{-1} s^{-1}$ [90] for the mobilities of molecular oxygen and chloride anions in air, but are reasonable considering the strong possibility of extensive clustering of oxygen and chloride anions in the drift volume, resulting in the decrease of reduced ion mobilities of oxygen as well as chloride ions. In addition, in Figures 4.12 and 4.13, the chloride ion signals contain back shoulders. Reasons for the back shoulders are not known for sure but may be related to clustering of oxygen ions with water molecules.[91]

Figures 4.14 and 4.15 show how the ion mobility spectra of methylene chloride and TCE change with dilution time at room temperature in air, respectively. The initial concentrations of methylene chloride and TCE in the flask were 750 ppmv and 11 ppmv, respectively. The flow rate of the drift gas, ultra pure nitrogen gas, was about 900 mL/min, and the dilution rate (Diluent gas is breathing-grade air.) was 28 mL/min. It is clear that, at the concentration of 5.6 ppmv (dilution time about 72 min), methylene chloride molecules can be identified, but below 5.6 ppmv, they are not recognized at all. At dilution times less than 63 min, corresponding to a concentration of 0.18 ppmv, TCE molecules can be recognized, but beyond 63 min dilution time, they are not identified. Figures 4.14 and 4.15 also indicate that the chloride ion signals due to low-energy electron attachment to methylene chloride and TCE consist of ion currents extending from about 3.0 ms to terminate beyond 5.0 ms of drift time.

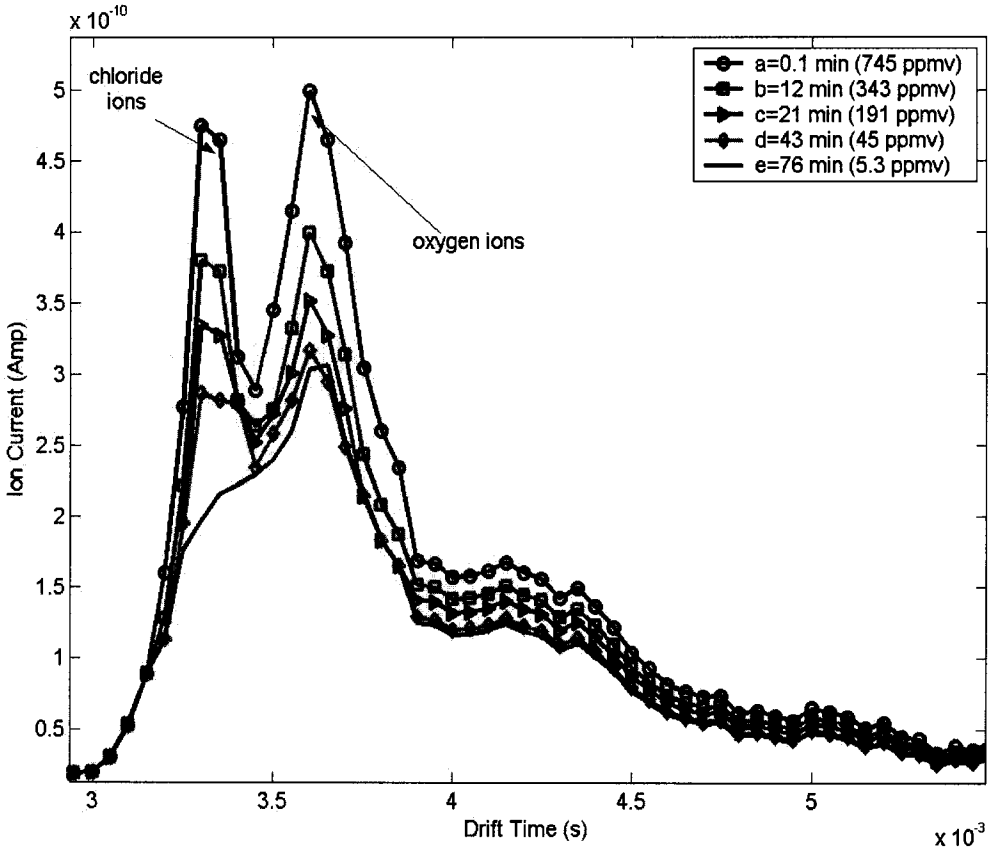

Figure 4.14. Chloride ion current due to low-energy electron attachment to methylene chloride as a function of drift time at acquisition times (a) 0.1 min, (b) 12 min, (c) 21 min, (d) 43 min, and (e) 76 min, corresponding to estimated concentrations of 745, 343, 191, 45, and 5.3 ppmv methylene chloride, respectively, at ambient pressure in air.

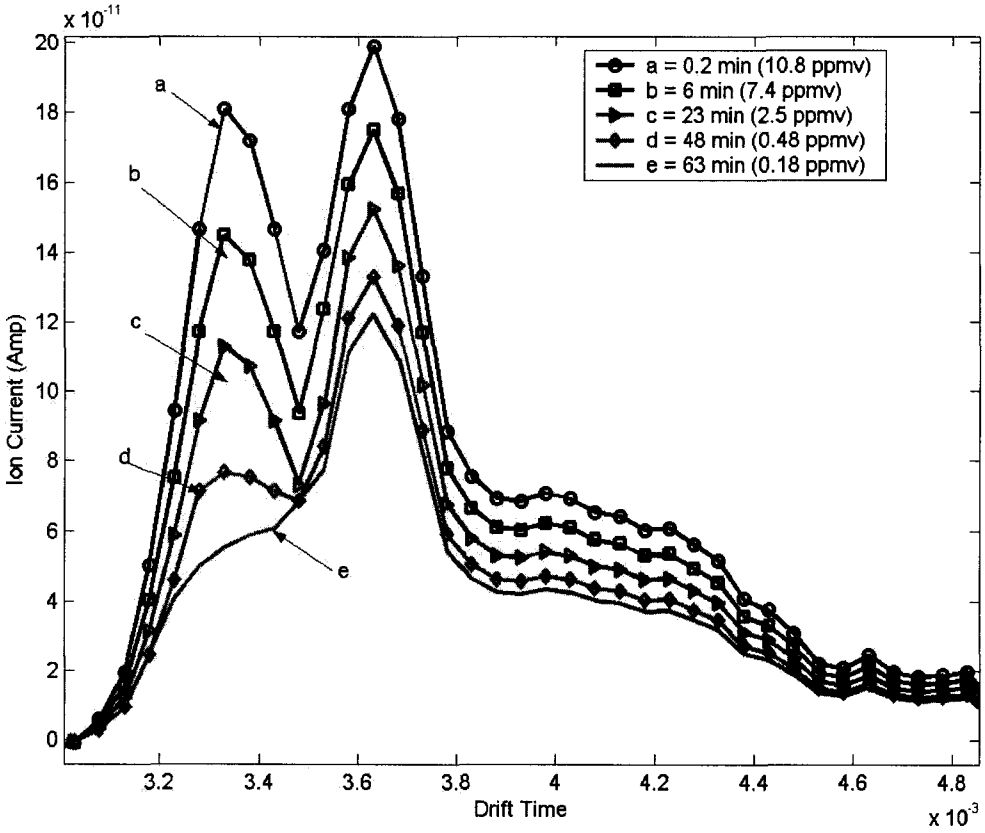

Figure 4.15. Chloride ion current due to low-energy electron attachment to TCE as a function of drift time at acquisition times (a) 0.2 min, (b) 6 min, (c) 23 min, (d) 48 min, and (e) 63 min, corresponding to estimated concentrations of 10.8, 7.4, 2.5, 0.48, and 0.18 ppmv TCE, respectively, at ambient pressure in air.

The negative ion mobility spectra obtained for a mixture of TCE and nitrobenzene in breathing-grade air are displayed in Figure 4.16. The ion mobility spectrum for TCE in the amount of 3.8 ppmv and 15 ppmv nitrobenzene in air, which appears in Figure 4.16, shows that collected chloride ions and nitrobenzene ions[46] are well separated from oxygen ions because of low-energy electron attachment to TCE, nitrobenzene, and oxygen molecules forming anions. For comparison, spectra for 3.8 ppmv TCE in nitrogen and 15 ppmv nitrobenzene in nitrogen are also plotted. Three ion mobility peaks are observed with reduced mobilities of 2.40 $cm^2\ V^{-1}\ s^{-1}$, 2.60 $cm^2\ V^{-1}\ s^{-1}$, and 1.85 $cm^2\ V^{-1}\ s^{-1}$ obtained from calculation by using the definition of reduced ion mobility via length of the drift tube, the drift time, and magnitude of the electric field shown in Eq. 4.1. Even though those values of reduced ion mobilities are lower than values found in the literature for the ion mobilities of bare molecular oxygen (2.5 $cm^2\ V^{-1}\ s^{-1}$), chloride (2.94 $cm^2\ V^{-1}\ s^{-1}$),[88] and nitrobenzene (1.74 $cm^2\ V^{-1}\ s^{-1}$)[89] anions, it might be due to the strong possibility of extensive clustering of anions in the drift volume and measurement error (or measurement precision).

S. N. Lin studied halogenated benzenes, nitromethane, nitrobenzene, and other nitro compounds in an ion mobility spectrometer (IMS).[46] His experimental results have shown that, in the IMS spectrum of nitromethane, 2 peaks were observed while, in the case of nitrobenzene, only the parent negative ion was observed at atmospheric pressure and 310 K in agreement with the present results in Figure 4.16.[46]

Since the vapor pressure of nitrobenzene liquid is very low, the nitrobenzene gas-phase molecules stick to the wall of 5 L flask, the inside surface of the cell housing the drift tube, and the Teflon drift tubing. Therefore, even though the initial concentration of

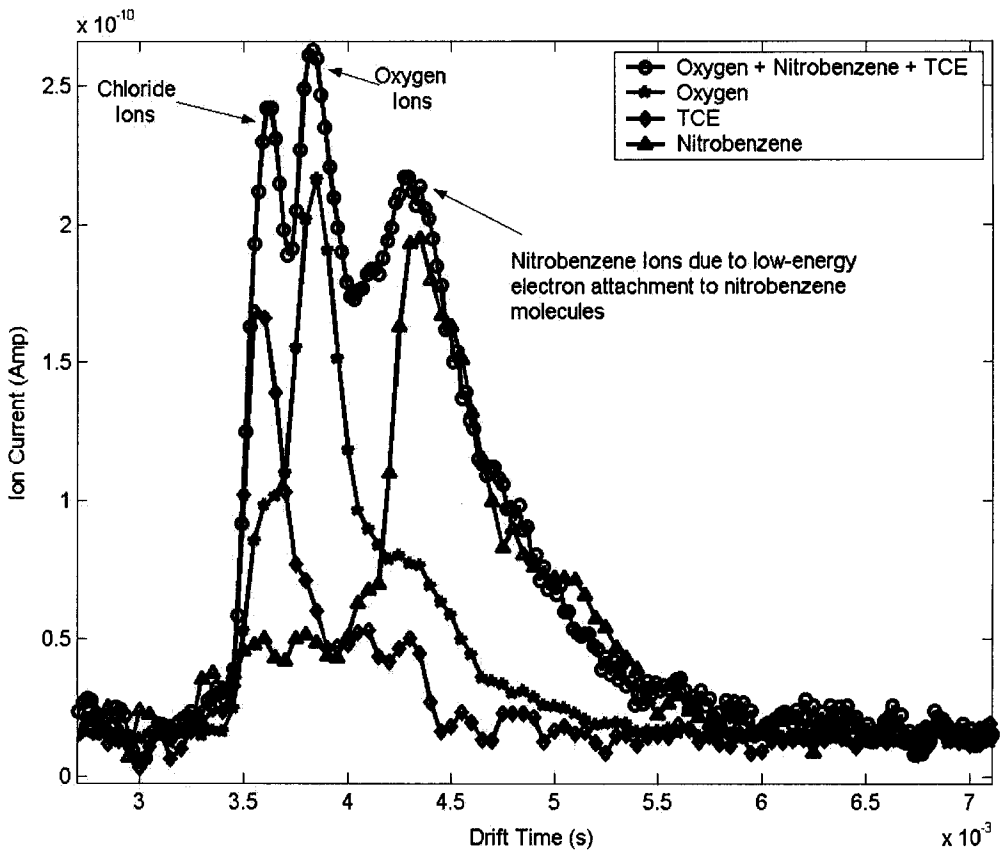

Figure 4.16. Ion mobility spectra of TCE and nitrobenzene in breathing-grade air.

nitrobenzene in the 5 L flask full of breathing-grade air is known, it is difficult to calculate the nitrobenzene vapor concentration reaching the PE-IMS.

It should be pointed out that, in the presence of nitrogen carrier gas, the reactant ions are low-energy electrons while the reactant ions are negative oxygen ions with a carrier gas of the breathing-grade air.[16,46,83] If breathing-grade air is used as a carrier gas, low-energy electrons emitted by the thin gold film attached to abundant oxygen molecules to form negative oxygen ions called reactant ions. The oxygen anions collide with the TCE or methylene chloride molecules, resulting in chloride anions.[24] The production of chloride anions is confirmed by the fact that the position of the chloride ion peak in ultra pure nitrogen is the same as that of the chloride ion peak in air.

The separation of ion mobility spectra was very sensitive to the position of the end of the Teflon carrier gas tube placed in the space between the photoemitter and the first guard ring of the drift tube. When the end of the carrier gas tube was moved close to the first guard ring, the separation was better while, when it was located outside the diameter of the drift tube, the ion signal was large and broad. The broadening and increase of ion signal occurred due to oxygen ion production throughout the drift space that resulted in signal overlap. Therefore, the stainless steel tube to seal the drift tube was added to prevent gas flow into the drift space from the sides of the drift tube. If the end of the carrier tube was next to the photoemitter, the ion signal was not detectable. It was also observed that a large number of electrons emitted by the gold film were unattached to either oxygen molecules or other molecules of interest. A large number of unattached electrons indicates that only a small amount of oxygen molecules in air captured electrons to form oxygen ions for the configuration that gave the best separation of ion peaks.

4.5.3. Detection of p-nitrotoluene; m-dinitrotoluene; 2,4-dinitrotoluene; and 2,6-dinitrotoluene Vapors at Ambient Pressure in Air

The gas lines and the PE-IMS were flushed for 1 hour at 300 mL/min with ultra pure nitrogen gas to eliminate contamination. A single vapor or a mixture of vapors was then delivered to the PE-IMS in either ultra pure nitrogen or breathing-grade air carrier gas flowing at 900 mL/min through the tee.

Nitro-organic explosives have relatively high electronegativities and, thus, favor the formation of stable, negative gas-phase ions via atmospheric pressure chemical ionization reactions (APCI).[16] Previous studies suggested that the ionization of nitro-organic explosive compounds in an electron capture detector IMS depended on the carrier gas composition.[16,92] Spangler and Lawless[92] investigated the ion-molecule chemistry for the negative ionization of nitroaromatic compounds, such as mono-nitrotoluenes; 2, 4-DNT; and 2, 6-TNT, in air as well as in nitrogen and found that the dominant ions created with nitrogen as a carrier gas were M^- via electron attachment at 166 °C at atmospheric pressure. However, the main ions generated in air carrier gas, with O_2^- as a reactant ion produced from electron attachment to oxygen molecules, were $(M-H)^-$ resulting from proton abstraction for every nitroaromatic compound of interest except m-MNT, which remained as M^- as shown Eqs. 4.5 and 4.6. [16]

$$e^- + M \rightarrow M^- \qquad (4.5)$$

$$X^- + M \rightarrow M \cdot X^- \xrightarrow{Heat} (M-H)^- + HX \qquad (4.6)$$

$$X^- + M \rightarrow M \cdot X^- \xrightarrow{Heat} M^- + X\,, \qquad (4.7)$$

where e^- is an electron in nitrogen and X^- is O_2^- or Cl^- with an acidic proton in air.

Eq. 4.5 represents the reaction between reactant ions, free electrons, and sample molecules in nitrogen (associative electron attachment), and Eq. 4.6 denotes the reaction in air. At the same time, minor fragments were observed and were identified as $(M-OH)^-$ and $(M-NO)^-$, and loss of NO_2 was seen only with MNT and only in small amounts. Spangler and Lawless's experimental data[92] indicated that the proportion between M^- and $(M-OH)^-$ was quantitatively controlled by the amount of O_2 in nitrogen which worked as a carrier gas. These reactions were confirmed later by Lubman, Huang, and Kolaitis,[83] who found that the DNT (dinitrotoluene) gave M^- in nitrogen for the three isomers (2,4-; 3,4-; and 2,6-DNT) at $50^\circ C$. The addition of air resulted in the formation of the proton abstracted species $(M-H)^-$ for all species except the 3, 4-isomer (3, 4-DNT only exhibited M^- even in air).[16]

In summary, APCI reactions of nitrotoluene compounds with IMS methods produce M^- ions when only thermal electrons are present by using nitrogen as a carrier gas, to which photoemiited electrons do not attach. In the presence of O_2^- ions resulting from free electron attachment to oxygen molecules, proton abstraction occurs to yield $(M-H)^-$. Curves showing the M^- or $(M-H)^-$ anion captured by using either the ultra pure nitrogen or the breathing-air carrier gas are shown in Figures 4.17, 4.18, 4,19, and 4.20 for 2, 4-dinitrotoluene; 2, 6-dinitrotoluene; and p-nitrotoluene, respectively.

The negative ion mobility spectra recorded for 2,4-DNT; 2, 6-DNT; and p-MNT are displayed in Figures 4.17, 4.18, and 4.20. They were taken in the presence of either nitrogen or air carrier gas with nitrogen drift gas at atmospheric pressure and room

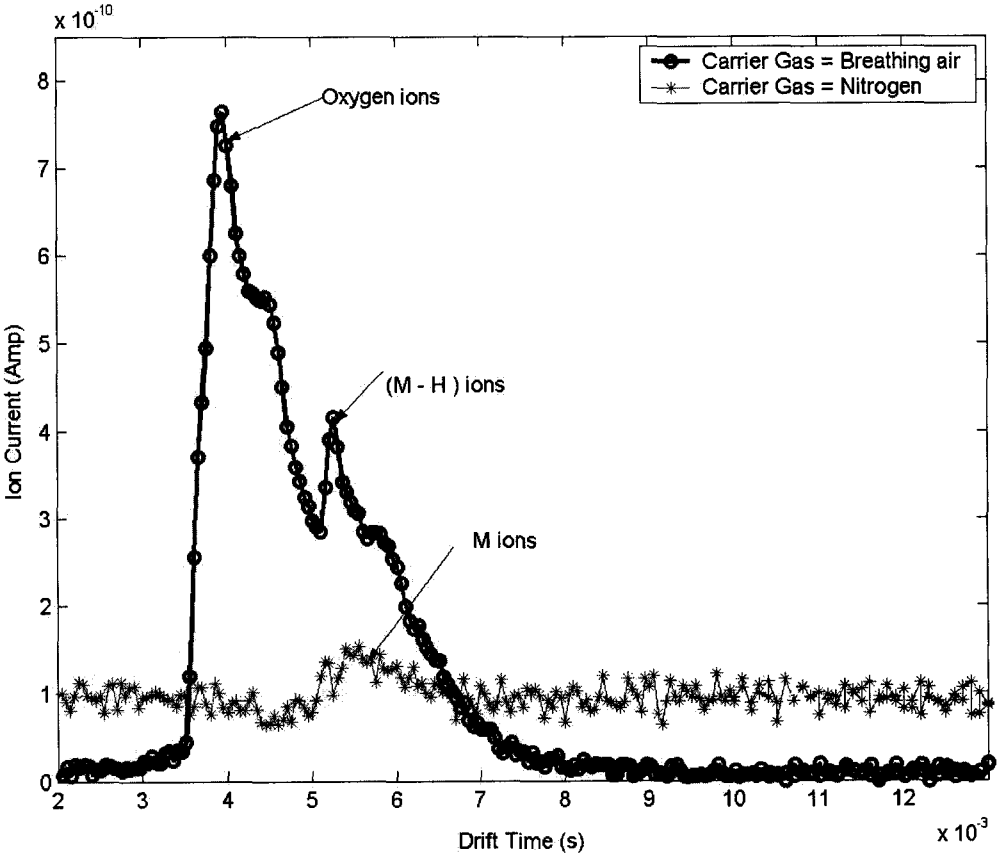

Figure 4.17. Comparison of 2, 4-dinitrotoluene ion mobility spectra between using the breathing-grade compressed air and ultra pure nitrogen gas as carrier gases. The drift gas in these two cases is the same gas, ultra pure nitrogen.

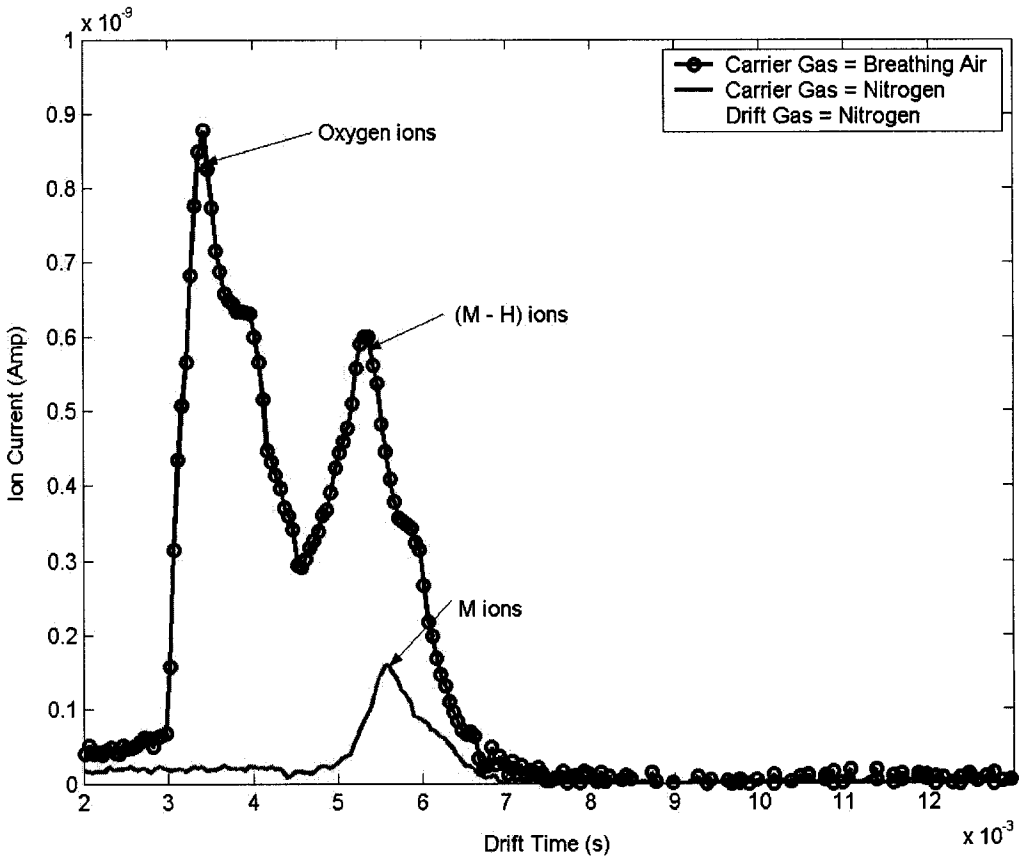

Figure 4.18. Comparison of ion signals, due to electron attachment to 2, 6-dinitrotoluene, between using the breathing-grade compressed air and ultra pure nitrogen gas as carrier gases. The drift gas in these two cases is the same gas, ultra pure nitrogen.

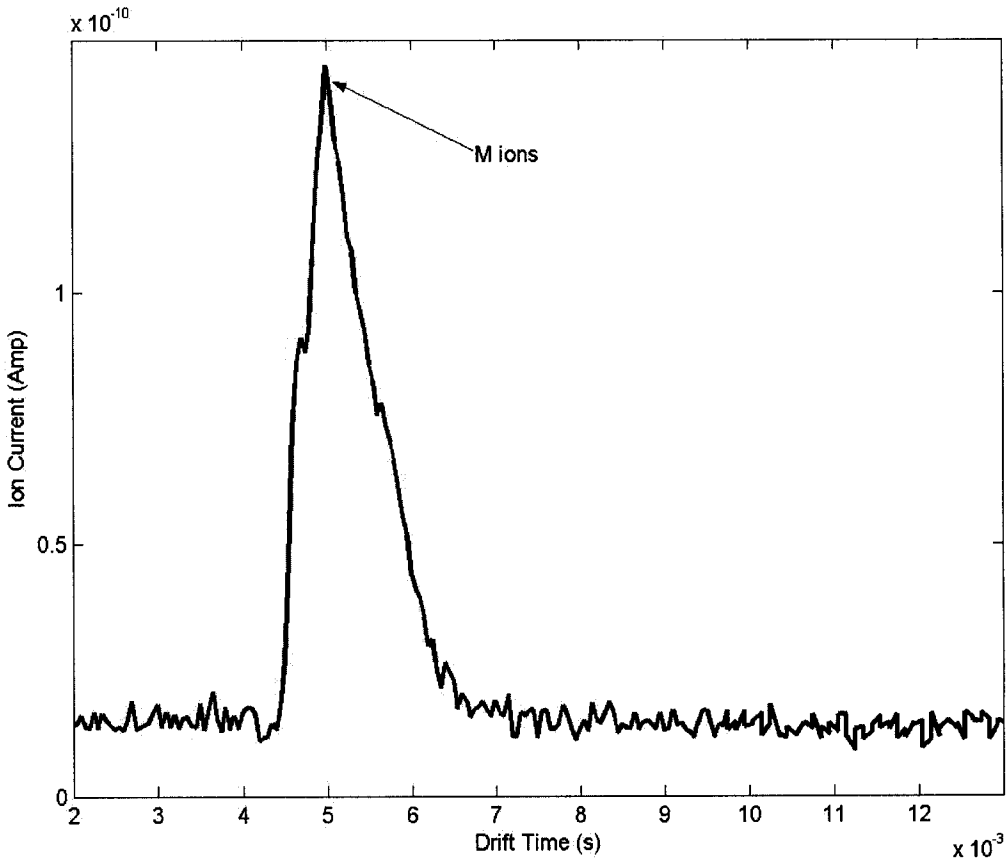

Figure 4.19. Ion current signal resulting from low-energy electron attachment to p-nitrotolurene versus drift time with the drift gas of ultra pure nitrogen and the carrier gas of ultra pure nitrogen.

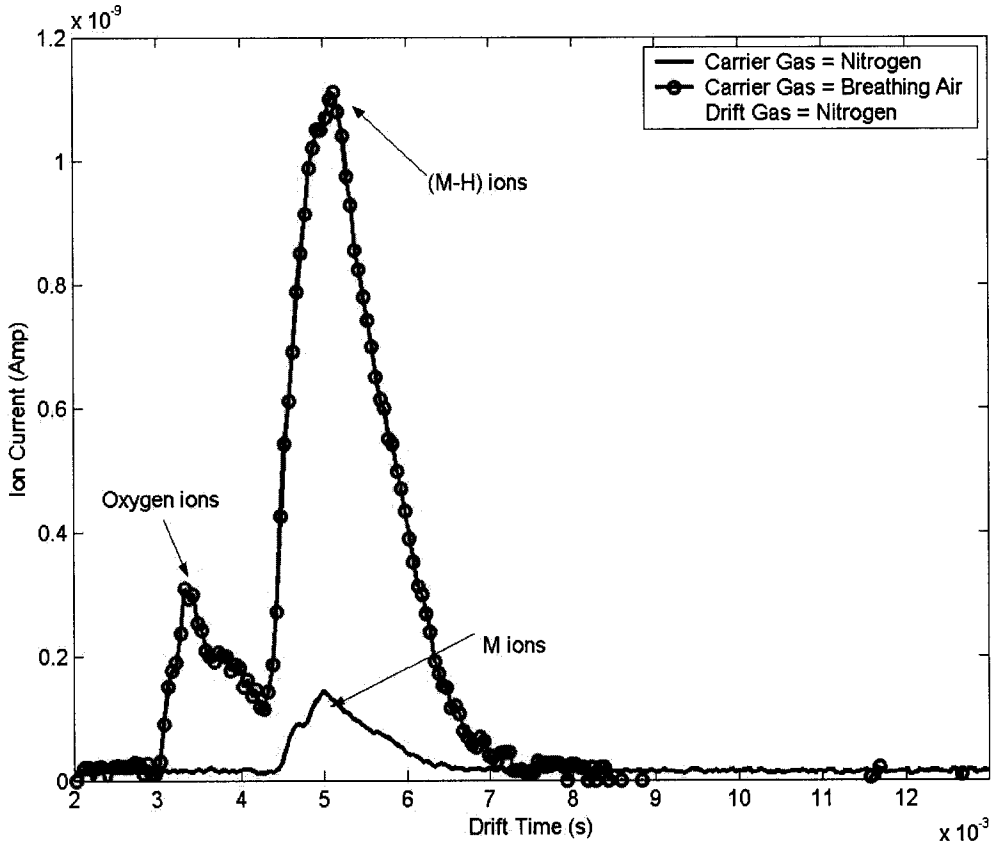

Figure 4.20. Comparison of ion signals, due to electron attachment to p-nitrotoluene, between using the breathing-grade compressed air and ultra pure nitrogen gas as carrier gases. The drift gas in these two cases is the same gas, ultra pure nitrogen.

temperature. From Figures 4.17, 4.18, and 4.20, the reduced ion mobility values of 2, 4-DNT; 2, 6-DNT; and p-MNT can be calculated in the presence of either air or nitrogen carrier gas with nitrogen drift gas at room temperature based on the IMS spectra by using Eq. 4.1. Two characteristic ion mobility species of 2, 6-DNT in air were observed with reduced mobilities of 2.58 $cm^2\ V^{-1}\ s^{-1}$ and 1.61 $cm^2\ V^{-1}\ s^{-1}$ while there was only a single 1.58 $cm^2\ V^{-1}\ s^{-1}$ peak in nitrogen. Similarly, for 2, 4-dinitrotoluene, two different types of molecular anions were the prominent 2.33 $cm^2\ V^{-1}\ s^{-1}$ and 1.66 $cm^2\ V^{-1}\ s^{-1}$ ion species observed in the presence of air carrier gas despite the fact that there was only one 1.68 $cm^2\ V^{-1}\ s^{-1}$ anion peak in the IMS spectrum by using nitrogen carrier gas. For p-MNT, two anion peaks rose from 2.62 $cm^2\ V^{-1}\ s^{-1}$ and 1.77 $cm^2\ V^{-1}\ s^{-1}$ ions with air carrier gas, but there was one 1.84 $cm^2\ V^{-1}\ s^{-1}$ ion peak in IMS spectrum in the presence of nitrogen carrier gas.

The reduced ion mobility values measured for 2,4-DNT; 2,6-DNT; and p-MNT show satisfactory consistency with the literature values obtained at 50 °C, 250 °C, or 166 °C listed in Table 2. In Table 2, the units of reduced ion mobility are $cm^2\ V^{-1}\ s^{-1}$. The similarity of measured values of reduced ion mobilities to the literature values at 50 °C, 250 °C, or 166 °C indicates a possible formation of $(M-H)^-$ ions in air but M^- ions in nitrogen.

Table 4.1. PE-IMS of 2,4-DNT; 2,6-DNT; and p-MNT in the nitrogen or air drift gas[16,83]

Compounds	Carrier/drift gas	Species	K_0 Literature Values ($cm^2/V\,s$)	T ($^{\circ}C$)	K_0 Measured values ($cm^2/V\,s$)	T ($^{\circ}C$)
2,4-DNT	N_2/N_2	M^-	1.61	50	1.68	25
2,4-DNT	Air/N_2	$(M-H^-)$	1.62 (1.67)	250 (50)	1.66	25
2,6-DNT	N_2/N_2	M^-	1.52	50	1.58	25
2,6-DNT	Air/N_2	$(M-H^-)$	1.61	50	1.65	25
p-MNT	N_2/N_2	M^-	1.79	250	1.84	25
p-MNT	Air/N_2	$(M-H^-)$	1.74	166	1.77	25

In Figures 4.17, 4.18, and 4.20, the IMS spectra of 2,4-DNT, 2,6-DNT, and p-MNT are shown where oxygen-free nitrogen carrier gas was used and oxygen-containing air was present in the carrier gas. The peak heights and areas are enhanced by the presence of oxygen at room temperature. It is known that the sensitivity of the IMS equipped with a ^{63}Ni ionization source to certain explosives can be enhanced by adding chlorinated reactants to the carrier gas.[88] In 1970, Dennis A. Miller and Eric P. Grimsrud[93,94] demonstrated that the large enhancement of response to 32 simple chlorinated molecules of a constant-current electron capture detector (ECD), which detected the electron loss reaction to gas-phase molecules, was achieved by the addition of oxygen to its carrier gas. As early as 1974, the intense response to 1-10 ng of TNT in a mobility spectrometer was reported for negative ions by Karasek and Denney.[95,96] It was noted that the carrier gas

affected the mobility spectrum (i.e., ions formed) and that the sensitivity of response was increased with oxygen.

Moisture has been seen to alter drift times of ions by expanding hydration shells and making ions larger and mobilities lower. In Figures 4.17, 4.18, and 4.20, it appears that the analyte ion signals contain back shoulders. The back shoulders are due to clustering of analyte and oxygen ions with water molecules.

Figure 4.21 indicates the ion mobility spectrometric separation of a gas mixture that contained oxygen (because air is the carrier gas); 2, 4-DNT; m-dinitrobenzene; and 2, 6-DNT molecules as well as the IMS spectra separately recorded for an individual gas with the breathing-grade air as the carrier gas and the ultra pure nitrogen gas as the drift gas at ambient pressure at room temperature. Oxygen anions have the largest reduced ion mobility value (measured value: 2.53 $cm^2\ V^{-1}\ s^{-1}$) and, thus, arrived before 2,4-DNT; m–dinitrotoluene; and 2,6–DNT. In addition, the IMS spectra reveal that the ion current peak of 2,4-DNT overlapped with that of 2,6-DNT because of the similarity of their reduced ion mobilities (1.66 $cm^2\ V^{-1}\ s^{-1}$ and 1.65 $cm^2\ V^{-1}\ s^{-1}$) in the presence of air carrier gas with nitrogen drift gas. From Figure 4.21, it is also seen that, since the reduced ion mobilities of 2,4-DNT and 2,6-DNT are lower compared with that of m-dinitrobenzene, m-dinitrobenzene arrived after 2,4-DNT and 2,6-DNT. In the mixture, since vapor pressures of 2,4-DNT; 2,6-DNT; and p-nitrotoluene are very low at room temperature, and thus absorb on the Teflon tube surfaces, the concentrations of 2,4-DNT; 2, 6-DNT; and p-MNT in the IMS are unknown.

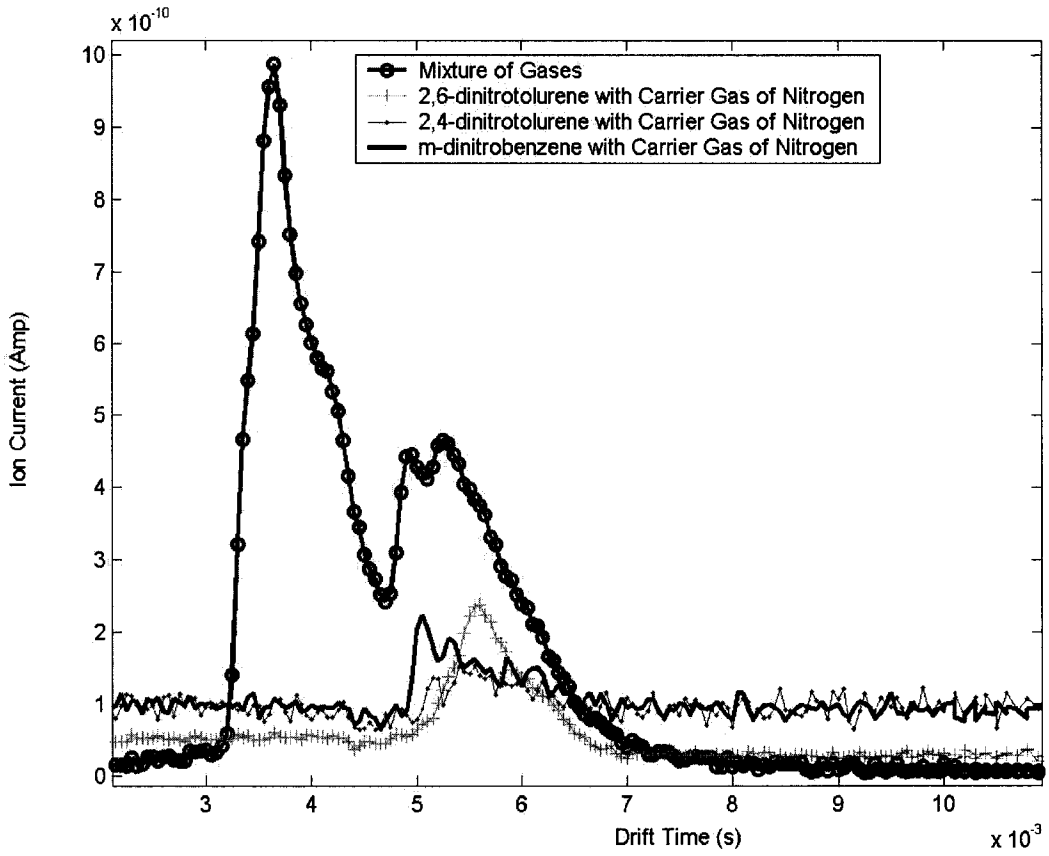

Figure 4.21. IMS spectra recorded for coexistence of 2, 4-dinitrotoluene; m-dinitrobenzene; and 2, 6-dinitrotoluene with the drift gas of ultra pure nitrogen gas at the flow rate of 900 mL/min and the carrier gas of the breathing-grade compressed air at room temperature in ambient air. The flow rate of the carrier gas is 28 mL/min.

CHAPTER 5

CONCLUSION AND FUTURE WORK

5.1. CONCLUSIONS

Although the ^{63}Ni ionization source is currently the ionization source of choice for most commercial IMS instruments, a photoemissive ionization source was demonstrated to be a stable, sensitive, selective, and reliable ionization source for IMS detection of electronegative vapor samples, such as explosives at ambient pressure at room temperature in air.

In the theoretical part of this work, an overview of both volume and surface plasmons in a metal as well as at a metal/medium interface was given. The focus of the theoretical analysis was on the surface plasmons at the metal/air interface for different wavelengths (632.8 nm, 532 nm, and 266 nm), and the incident angles causing a resonant excitation of the surface plasma have been calculated. Theoretical results have indicated that 632.8 nm and 532 nm light excite the surface plasmons resonantly for gold films' thicknesses in the range from 20 nm to 50 nm. Moreover, we have found that 266 nm light was unable to excite surface plasmons because it cannot satisfy the resonance condition (Eq. 4.2).

In the experimental part of this work, the results of reflectance versus incident angle were compared to those calculated by the three-layer system Fresnel's equations. For 532 nm and 632.8 nm, experimental measurements and theoretical predictions were in good agreement for both s- and p-polarized light. However, for 266 nm, the measured reflectance matched that computed by Fresnel's equation for p-polarized light while the measured reflectance was not in agreement for s-polarized light. Most importantly,

one photon-like photoemission from a 20-nm thick gold film sputter-coating on a fused silica prism was found when the film was irradiated by a 266-nm Nd:YAG or microchip laser with 230-μJ and 100-nJ pulse energy, respectively. By monitoring the free electron current signal generated by both s- and p-polarized laser beams and the corresponding reflectance simultaneously, we have shown that the photo-emitted electron signals were enhanced about five times for angles of incidence beyond the critical angle. After passing the critical angle, the photoemission stayed approximately the same as shown in Figure 3.15. It was also discovered that photoemission peaked at a different incident angle than that registered by the reflectance spectra by 3°.

This enhancement after passing the critical angle was not due to resonant excitation of the surface plasmons because 266 nm light cannot satisfy the resonant condition. The reasons for enhancement were not known; however, it might result from the penetration of the evanescent wave into the gold-air interface which helps electrons escape from the surface. Furthermore, beyond the critical angle, the 266-nm light cannot be transmitted into the ionization region between the thin gold film and the first electrode of the drift tube in the IMS system because of total internal reflection. Thus, no transmitted 266-nm light removed the possibility of photo-dissociative fragmentation of the vapor explosive molecules. In other words, not only was an increase of IMS sensitivity attained by enhancing the photoemission with the 266-nm Nd:YAG laser at ambient pressure in air by 5 times after passing the critical angle, but no photo-dissociation happened in the ionization region simply because no 266-nm light beam can be transmitted due to total internal reflection. This feature was very important to improve detection limits of IMS by limiting

fragmentation of ions.[16] Anion current variations with thickness of the thin gold film were also experimentally established.

In addition, the PE-IMS detector at room temperature can ionize and detect chloride ions from chlorinated aliphatic compounds including TCE and methylene chloride. Chlorinated aliphatic compounds were easily detected in the presence of other electron-attaching species, such as oxygen molecules, at ambient temperature in air. As demonstrated in this study, IMS equipped with a photoemissive ionization source had the capability to rapidly detect gaseous-phase nitro-organic compounds (explosives) such as 2,4-DNT; 2,6-DNT; and p-nitrotoluene at atmospheric pressure and room temperature in air. While these studies were limited to three nitro-organic molecules, the analytical principles demonstrated in this study are expected to be applicable to a wide range of electronegative compounds, in particular common explosives such as TNT and RDX.

A 532 nm Nd:YAG laser was used to illuminate the 20-nm thick gold film, and no photoelectron signal was detected with either s- or p-polarized laser. Although the incident angle for 532 nm was adjusted to the angle at which the incident light can resonantly excite the surface plasmons at the air-gold interface based on the theoretical calculation (detailed in Appendix B), no photoemission signal was observed.

5.2. Future Work

5.2.1. Improvement of IMS Resolution

There are possible further improvements of the IMS resolution by optimizing three parameters: bias voltage, temperature of the drift gas, and length of the drift tube. IMS experiments for detecting chlorinated and nitro-organic compounds were conducted at room temperature. Heating the detectors may provide instant improvements to detection of

chlorinateds and nitroaromatics in air by means of reduction of clustering that affects ion drift times and broadens ion signatures. On the other hand, as described by Revercomb and Mason[97] in 1974, the resolving power is given approximately by

$$\frac{t_d}{\Delta t} = \frac{L \times E \times z \times e}{\sqrt{16 k_B T \ln 2}} = \frac{V \times z \times e}{\sqrt{16 k_B T \ln 2}}, \quad (5.1)$$

where t_d is the drift time, Δt is the ion pulse duration at the detector measured at half of the maximal intensity, L is the length of the drift tube, V is the voltage drop across the drift tube, ze is the charge on the ion, T is the temperature of the drift gas in Kelvin, k_B is Boltzmann's constant, and E is the electric field along the drift tube. It is apparent from the above expression that the decrease of temperature enhances the resolving power, but it might result in an increase of clustering (water molecules) that affects ion drift times and broadens ion signals. It is clear that there is an optimum temperature of the drift gas.

In addition, in order to increase the resolving power, it is necessary to increase the drift field, E, or increase the length, L, of the drift tube. If the drift field is increased, there must be a corresponding increase in the length of the drift tube at atmospheric pressure. There are several reasons why increasing the resolving power by increasing its voltage also requires making the drift tube longer.[98] First, increasing the voltage applied to the drift tube eventually results in electrical breakdown. Second, it has generally been considered important to operate in the low-field regime in which the ion velocity remains proportional to E. The low-field regime requires that IMS experiments be performed with an $\frac{E}{N}$ ratio no

more than 1 to 2×10^{-7} V cm^2, where N is the number density of the drift gas (in cm^{-3}).[85] Thus, for atmospheric pressure conditions, the typical E values are between 246 V/cm and 493 V/cm.[98] At this point, an increase of both bias voltage and length of the drift tube contributes to the increase of IMS resolution; however, if the length of the drift tube is increased, the ion spectra become broader because of the diffusion effect. Therefore, the length needs to be optimized.

5.2.2. Laser-Induced Desorption

There are quite a few techniques to desorb a solid or liquid sample into the gas phase, such as field desorption,[99] laser desorption,[83, 100] plasma desorption,[101] etc. A means of vaporizing these samples has remained an important issue, which determines the degree of fragmentation of vapor sample molecules (break molecules into parts), in ion mobility spectrometry. The typical approach to desorbing samples is thermal desorption in which a sample is placed on a desorber which is maintained at a fixed temperature, typically 200° C to 300° C, to thermally vaporize the sample into the gas phase. However, the main disadvantage of this approach is that most explosive compounds are thermally unstable upon heating; that is, these compounds easily decompose into fragments as the temperature is increased. Limiting fragmentation is very important to improve the detection limits of IMS.[16]

The principal advantage of pulsed laser desorption would be to minimize thermally induced fragmentation and enhance vaporization of the solid explosive sample, resulting in a larger gas phase sample available for ionization; that is, pulsed-laser desorption could produce gas phase intact neutrals of explosive compounds of interest. The most important

characteristic of pulsed-laser induced heating of metal surfaces is that heating and cooling times are on the time scale of nanoseconds and, thus, the rate of heating is on the order of 10^{10} K/s .[102] The rate of heating achievable with nanosecond laser pulses is sufficiently high that the time for molecules on the surface to desorb is much shorter than the time available for decomposition or some other chemical reactions. Therefore, the surface molecules desorb into the gas phase before decomposition happens. Lubman demonstrated that there was no fragmentation with desorption of a pulsed laser.[83,103] It was also shown that the fourth harmonic of the Nd:YAG laser at 266 nm worked as well as 532 nm did. In addition, his work showed that a CO_2 laser was preferred for desorption more than the 532 nm from the Nd:YAG laser.

Since laser parameters, such as output intensity, pulse width, wavelength, etc., and surface characteristics will greatly influence the degree of fragmentation, laser parameters and surface material need to be chosen carefully.

5.2.3. Photoemission

The photoelectron signals were enhanced about five times for incidence angles after passing the critical angle. This significant enhancement is not due to resonant excitation of the surface plasmons on the metal-air interface because 266 nm light cannot satisfy the resonant condition. The reasons for enhancement are not known and need to be established. It was also observed that the introduction of chemical vapors, such as oxygen, water, and cyclohexene, influenced the work function of gold. Further work should include the effect of chemical vapors on work function at ambient pressure.

REFERENCES CITED

[1] K. J. Castle, James E. Abbott, X. Peng, and W. Kong, *Journal of Physical Chemtry A,* **104**, 10419-10425, 2000.

[2] S. Zabarnick, J. W. Fleming, and A. P. Baronavski, *Journal of Chemical Physics*, **85**, 3395-3400, 1986.

[3] A. C. Gonzalez, C. W. Larson, D. F. McMillen, and D. M. Golden, *Journal of Physical Chemistry,* **89**, 4809, 1985.

[4] W. Tsang, D. Robaugh, and W. G. Mallard, *Journal of Physical Chemistry,* **90**, 5968-5973, 1986.

[5] J. Shao and T. Baer, *International Journal of Mass Spectrometry and Ion Processes*, **86**, 357-367, 1988.

[6] F. W. Karasek and D. W. Denney, *Journal of Chromatography*, **93**, 141-147, 1974.

[7] G. E. Spangler and P. A. Lawless, *Analytical Chemistry*, **50**, 884-892, 1978.

[8] G. E. Spangler, J. P. Carrico, and D. N. Campbell, *Journal of Testing and Evaluation*, **13**, 234-240,1985.

[9] A. H. Lawrence and P. Neudorfl, *Analytical Chemistry*, **60**, 104-109, 1988.

[10] D. D. Fetterolf and T. D. Clark, *Journal of Forensic Sciences*, **38**, 28-39, 1993.

[11] R. G. Ewing and C. J. Miller, *Field Analytical Chemistry and Technology*, **5**, 215-221, 2001.

[12] M. Tam and H. H. Hill, Jr., *Analytical Chemistry,* **76**, 2741-2747, 2004.

[13] I. A. Buryakov, *Journal of Chromatography, B: Analytical Technologies in the Biomedical and Life Sciences*, **800**, 75-82, 2004.

[14] C. Wu, W. F. Siems, and H. H. Hill, Jr., *Analytical Chemistry*, **72**, 396-403, 2000.

[15] D. W. Hannum and J. E. Parmeter, *Survey of Commercially Available Explosives Detection Technologies and Equipment for the National Law Enforcement and Corrections Technology Center*, a Program of the National Institute of Justice, U.S. Department of Justice, September 1998, http://www.dtic.mil/ndia/security2/parmeter.pdf, December 2003.

[16] R. G. Ewing, D. A. Atkinson, G. A. Eiceman, and G. J. Ewing, *Talanta*, **54,** 515–529, 2001.

[17] J. I. Baumbach and G. A. Eiceman, *Applied Spectroscopy*, **53**, 338A-355A, 1999.

[18] C. Wu and H. H. Hill, Jr., *Analytical Chemistry*, **71**, 273-278, 1999.

[19] A. H. Lwarence, P. Neudorfl, and J. A. Stone, *International Journal of Mass Spectrometry*, **209**, 185-195, 2001.

[20] C. J. Proctor and J. F. J. Todd, *Analytical Chemistry*, **56**, 1794-1797, 1984.

[21] G. A. Eiceman, D. Preston, G. Tiano, J. Rodriguez, and J. E. Parmeter, *Talanta*, **45**, 57-74, 1997.

[22] J. P. Davies, L. G. Blackwood, S. G. Davis, L. D. Goodrich, and R. A. Larson, *Analytical Chemistry,* **65**, 3004-3009, 1993.

[23] K. A. Daum, D. A. Atkinson, and R. G. Ewing, *Talanta*, **55**, 491-500, 2001.

[24] P. Begley, R. Corbin, B. E. Foulger, and P. G. Simmonds, *Journal of Chromatography,* **588**, 239-249, 1991.

[25] P. G. Simmonds, *Journal of Chromatography*, **399**, 149-146, 1987.

[26] U. A. Mirza, S. L. Cohen, and B. T. Chait, *Analytical Chemistry*, **65**, 1, 1993.

[27] D. S. Gross, P. D. Schnier, S. E. Rodriguez-Cruz, C. K. Fagerquist, and E. R. Williams, *Proceedings of the National Academy of Sciences,* USA, **93**, 3143, 1996.

[28] H. Borsdorf, H. Schelhorn, J. Flachowsky, H. R. Döring, and J. Stach, *Analytica Chimica Acta*, **403**, 235–242, 2000.

[29] B. T. Chait and S. B. H. Kent, *Science*, **257**, 1885, 1992.

[30] C. B. Shumate and H. H. Hill, Jr., *ACS Symposium Series*, **508**, 192-205, 1992.

[31] S. Sielemann, J. I. Baumbach, and H. Schmidt, *International Journal for Ion Mobility Spectrometry*, **5**, 143-148, 2002.

[32] S. K. Chowdhury, V. Katta, and B. T. Chait, *Journal of the American Chemical Society*, **112**, 9012, 1990.

[33] GE Ion Track, technical paper, *The Science Behind the Technology: Ion Trap Mobility Spectrometry*, 2003, http://www.newenglandertrading.com/IonTrack/down%20loads/ITMS_Tech_Paper.pdf, November 2003.

[34] L. B. Linford, *Reviews of Modern Physics*, **5**, 34-60, 1933.

[35] T. Smith, *Journal of Applied Physics*, **64**, 1553-1558, 1970.

[36] R. A. Millikan, *Physics Review*, **34**, 68, 1912.

[37] R. P. Winch, *Physics Review,* **29**, 451, 1927; **31**, 236, 1928.

[38] L. A. Dubridge, *Physics Review*, **37**, 1269, 1931.

[39] R. P. Winch, *Physics Review*, **37**, 1269, 1931.

[40] S. Dushman, *Reviews of Modern Physics*, **2**, 415, 1930.

[41] K. H. Kingdon, *Physics Review*, **24**, 510, 1924.

[42] W. B. Hales, *Physics Review*, **32**, 950, 1928.

[43] H. P. Bonzel and G. Pirug, *Physical Review Letters*, **58**, 2138, 1987.

[44] K. Inumaru, Y. Okuba, T. Fujii, and S. Yamanaka, *Physical Chemistry Chemical Physics*, **2**, 3681-3685, 2000.

[45] T. Kendelewicz, P. Liu, G. E. Brown, Jr., E. J. Nelson, and P. Pianetta, *Surface Science,* **352-354**, 451-456, 1996.

[46] E. C. M. Chen and E. S. Chen, *International Journal of Ion Mobility Spectrometry*, **3**, 11-14, 2000.

[47] Technotrade International, Inc., *Instruction Manual of SCD 030,* 7 Perimeter Road, Manchester, NH.

[48] L. Maissel and R. Glang, *Handbook of Thin Film Technology*, McGraw-Hill, New York, 1970.

[49] D. Statas, *Coatings Technology Handbook*, Marcel Dekker, Inc., New York, 1991.

[50] CERAC, Inc., Technical Publications, Mitchell C. Colton, Editor, December 1998, http://www.cerac.com/pubs/cmn/, September 2003.

[51] P. P. Herrmann and H. Staehli, *Journal of Physics E: Scientific Instruments*, **16**, 1072-1075, 1983.

[52] G. L. Weissler, "Photoionization in Gases and Photoelectric Emission from Solids", Springer-Verlag, Berlin, Germany, S. Fliigge (ed.): *Handbuch der Physik*, Band XXI *Elektronen-Emission, Gasentladungen I*, page 342, 1956.

[53] J. E. Lovelock and S. R. Lipsky, *Journal of the American Chemical Society,* **82**, 431, 1960.

[54] P. G. Simmonds, D. C. Fenimore, and B. *C*. Pettitt, and J. E. Lovelock, *Analytical Chemistry,* **39**, 1428, 1967.

[55] J. G. Dillard, *Chemical Reviews*, **73**, 589-644, 1973.

[56] J. H. Bowie, *Mass Spectrometry Reviews,* **3**, 161-207, 1984.

[57] E. A. Stemmler and R. A. Hites, *Biomedical and Environmental Mass Spectrometry,* **17**, 311-328, 1988.

[58] R. C. Dougherty and C. R. Weisenberger, *Journal of the American Chemical Society,* **90**, 6570-6571, 1968

[59] J. A. Laramée, B. C. Arbogast, and M. L. Deinzer, *Analytical Chemistry,* **58**, 2907-2912, 1986.

[60] D. H. Williamson, W. B. Knighton, and E. P. Grimsrud, *International Journal of Mass Spectrometry,* **195/196**, 481-489, 2000.

[61] I. Ogawa, N. Noda, and T. Sugiyama, *Proceedings of the US-Japan Seminar, Gas Breakdown and Its Fundamental Processes,* Tokyo, 23-31, 1973.

[62] R. H. Ritchie, *Surface Science*, **34**, 1-19, 1973.

[63] D. Bohm and D. Pines, *Phys. Rev.*, **92**, 609, 1953.

[64] D. Pines, *Physics Review,* **92**, 626, 1953.

[65] D. Pines, *Reviews of Modern Physics*, **28**, 184-199, 1956.

[66] D. Pines, *Physics Review*, **85**, 338-353, 1952.

[67] A. R. Melnyk and M. J. Harrison, *Physics Review B*, **2**, 835-850, 1970.

[68] P. A. Wolff, *Physics Review*, **92**, 18-23, 1953.

[69] J. S. Blakemore, *Solid State Physics*, 2d ed., Saunder, Philadelphia, 1974.

[70] H. Raether, *Surface Plasmons on Smooth and Rough Surfaces and on Gratings*, Springer, Herdelberg, Germany, 1988.

[71] R. A. Ferrell, *Physics Review*, **111**, 1214, 1958.

[72] R. A. Ferrel and E. A. Stern, *The American Journal of Physics*, **30**, 810, 1962.

[73] K. Johansen, H. Arwin, I. Lundstrom, and B. Liedberg, *Review of Scientific Instruments*, **71**, 3530-3538.

[74] H. J. Simon, D. E. Mitchell, and J. G. Watson, *The American Journal of Physics*, **43**, 630-636, 1975.

[75] B. Hecht, H. Bielefeldt, L. Novotny, Y. Inouye, and D. W. Pohl, *Physical Review Letters,* **77**, 1889-1892, 1996.

[76] E. Kretschmann, *Z. Phys.*, **241**, 313, 1971.

[77] F. L. Pedrotti and L. S. Pedrotti, *Introduction to Optics*, 2d ed., A Simon and Schuster Company, Englewood Cliffs, NJ, 1993.

[78] J. E. Sipe and J. Becher, *Journal of the Optical Society of America*, **71**, 1286-1288, 1981.

[79] J. G. Endriz, *Physics Review,* **B7**, 3464-3481, 1973.

[80] T. A. Callcott and E. T. Arakawa, *Physics Review*, **B11**, 2750-2758, 1975.

[81] E. D. Palik ed. *Handbook of Optical Constants of Solids II*, Academic Press Handbook Series, New York, 1985.

[82] T. Tsang, T. Srinivasan-Rao, and J. Fischer, *Bulletin of the American Physical Society*, **35**, 1535, 1990.

[83] S. D. Huang, L. Kolaitis, and D. M. Lubman, *Applied Spectroscopy*, **41**, 1371-1376, 1987.

[84] G. A. Eiceman, J. F. Bergloff, J. E. Rodriguez, W. Munro, and Z. Karpas, *Journal of American Society for Mass Spectrometry*, **10**, 1157–1165, 1999.

[85] E. Nasser, *Fundaments of Gaseous Ionization and Plasma Electronics*, John Wiley and Sons, Inc., New York, 1971.

[86] W. E. Steiner, B. H. Clowers, K. Fuhrer, M. Gonin, L. M. Matz, W. F. Siems, A. J. Schultz, and H. H. Hill, Jr., *Rapid Communications in Mass Spectrometry*, **15**, 2221-2226, 2001.

[87] J. J. Ritter and N. K. Adams, *Analytical Chemistry,* **48**, 612-619, 1976.

[88] L. M. Matz, P. S. Tornatore, and H. H. Hill, *Talanta*, **54**, 171-179, 2001.

[89] H. Sohn and J. Steinhanses, *International Journal for Ion Mobility Spectrometry*, **1**, 1-14, 1998.

[90] P. Dwivedi, L. M. Matz, D. A. Atkinson, and H. H. Hill, Jr., *Analyst*, **129**, 139-144, 2004.

[91] K. A. Daum, D. A. Atkinson, and R. G. Ewing, *Talanta*, **55**, 491-500, 2001.

[92] G. E. Spangler and P. A. Lawless, *Analytical Chemistry*, **50**, 884-892, 1978.

[93] D. A. Miller and E. P. Grimsrud, *Analytical Chemistry*, **51**, 851-859, 1979.

[94] D. A. Miller and E. P. Grimsrud, *Analytical Chemistry*, **50**, 1141-1145, 1978.

[95] F.W. Karasek, *Research/Development,* **25** 32–36, 1974.

[96] F.W. Karasek and D.W. Denney, *Journal of Chromatography*. **93**, 141–147, 1974.

[97] H. W. Revercomb and E. A. Mason, *Analytical Chemistry,* **47**, 970, 1975.

[98] C. Wu, W. F. Siems, G. R. Asbury, and H. H. Hill, Jr., *Analytical Chemistry,* **70**, 4929-4938, 1998.

[99] H. D. Beckey, *International Journal of Mass Spectrometry and Ion Physics*, **2**, 500, 1969.

[100] R. J. Cotter, *Analytical Chemistry*, **52**, 1770, 1980.

[101] R. D. MacFariane, D. Vemura, K. Veda, and Y. Hirata, *Journal of the American Chemical Society*, **102**, 875, 1980.

[102] L. Hanley, O. Kornienko, E. T. Ada, E. Fuoco, and J. L. Trevor, *Journal of Mass Spectrometry*, **34**, 705-723, 1999.

[103] L. Kolaitis and D. M. Lubman, *Analytical Chemistry*, **58**, 2137-2142, 1986.

APPENDIX A

CALCULATIONS OF THE WAVE VECTOR AND RESONANT CONDITION OF SURFACE PLASMONS

A.1. Computation of the Real and Imaginary Parts of the Wave Vector of Surface Plasmons

The wave vector, k_{sp}, of a surface plasmon, which propagates parallel to the interface and is exponentially attenuated in the normal direction, on a dielectric bounded by a dielectric medium such as air is given by Eq. 3.31 in Chapter 3

$$k_{sp} = \frac{\omega}{c}\sqrt{\frac{\varepsilon_1\varepsilon_2}{\varepsilon_1+\varepsilon_2}} \quad , \qquad (A.1)$$

where ε_2, $\varepsilon_2 = \varepsilon_2' + i\varepsilon_2''$, is the complex dielectric function of a metal; ε_1, a positive real number, is the dielectric function of a medium; ω is the angular frequency of the incident radiation; and c is the speed of light.

Since ε_2 is the complex dielectric function of a metal, Eq. A.1 becomes

$$k_{sp} = \frac{\omega}{c}\sqrt{\frac{\varepsilon_2\varepsilon_1}{\varepsilon_2+\varepsilon_1}} = k_{sp}' + ik_{sp}'' \quad , \qquad (A.2)$$

where k_{sp}' is the real part and k_{sp}'' is the imaginary part.

$$\sqrt{\frac{\varepsilon_2\varepsilon_1}{\varepsilon_2+\varepsilon_1}} = \sqrt{\frac{\varepsilon_1(\varepsilon_2'+i\varepsilon_2'')}{(\varepsilon_2'+\varepsilon_1)+i\varepsilon_2''}} = \sqrt{\frac{\varepsilon_1(\varepsilon_2'+i\varepsilon_2'')(\varepsilon_2'+\varepsilon_1-i\varepsilon_2'')}{(\varepsilon_2'+\varepsilon_1)^2+(\varepsilon_2'')^2}}$$

$$= \sqrt{\frac{\varepsilon_1\left[(\varepsilon_2')^2+\varepsilon_2'\varepsilon_1+(\varepsilon_2'')^2\right]+i\varepsilon_2''(\varepsilon_1)^2}{(\varepsilon_2'+\varepsilon_1)^2+(\varepsilon_2'')^2}}$$

$$= \sqrt{\frac{\varepsilon_1[(\varepsilon_2')^2 + \varepsilon_2'\varepsilon_1 + (\varepsilon_2'')^2]}{(\varepsilon_2' + \varepsilon_1)^2 + (\varepsilon_2'')^2}} \sqrt{1 + \frac{(\varepsilon_2' + \varepsilon_1)^2 + (\varepsilon_2'')^2}{\varepsilon_1[(\varepsilon_2')^2 + \varepsilon_2'\varepsilon_1 + (\varepsilon_2'')^2]} \frac{i\varepsilon_1''(\varepsilon_2)^2}{(\varepsilon_2' + \varepsilon_1)^2 + (\varepsilon_2'')^2}}$$

$$= \sqrt{\frac{\varepsilon_1[(\varepsilon_2')^2 + \varepsilon_2'\varepsilon_1 + (\varepsilon_2'')^2]}{(\varepsilon_2' + \varepsilon_1)^2 + (\varepsilon_2'')^2}} \sqrt{1 + \frac{i\varepsilon_2''(\varepsilon_1)^2}{\varepsilon_1[(\varepsilon_2')^2 + \varepsilon_2'\varepsilon_1 + (\varepsilon_2'')^2]}} \quad . \qquad \text{(A.3)}$$

Recall the binomial series

$$(1+x)^\alpha = 1 + \alpha x + \frac{\alpha(\alpha-1)}{2!}x^2 + \cdots + \frac{\alpha(\alpha-1)\cdots(\alpha-n+1)}{n!}x^n + \cdots, \; x^2 \le 1 \; .$$

Let $X = \sqrt{1 + \frac{i\varepsilon_2''(\varepsilon_1)^2}{\varepsilon_1[(\varepsilon_2')^2 + \varepsilon_2'\varepsilon_1 + (\varepsilon_2'')^2]}}$

$$X = 1 + \frac{1}{2}\frac{\varepsilon_2''(\varepsilon_1)^2}{\varepsilon_1[(\varepsilon_2')^2 + \varepsilon_2'\varepsilon_1 + (\varepsilon_2'')^2]}i + \frac{\frac{1}{2}\times(\frac{1}{2}-1)}{2}\left\{\frac{\varepsilon_2''(\varepsilon_1)^2}{\varepsilon_1[(\varepsilon_2')^2 + \varepsilon_2'\varepsilon_1 + (\varepsilon_2'')^2]}i\right\}^2$$

$$+ \frac{\frac{1}{2}\times\left(\frac{1}{2}-1\right)\times\left(\frac{1}{2}-2\right)}{3\times 2\times 2}\left\{\frac{\varepsilon_2''(\varepsilon_1)^2}{\varepsilon_1[(\varepsilon_2')^2 + \varepsilon_2'\varepsilon_1 + (\varepsilon_2'')^2]}i\right\}^3 + \ldots$$

$$= 1 + \frac{1}{2}\frac{\varepsilon_2''(\varepsilon_1)^2}{\varepsilon_1[(\varepsilon_2')^2 + \varepsilon_2'\varepsilon_1 + (\varepsilon_2'')^2]}i + \frac{1}{8}\frac{(\varepsilon_2'')^2(\varepsilon_1)^4}{(\varepsilon_1)^2[(\varepsilon_2')^2 + \varepsilon_2'\varepsilon_1 + (\varepsilon_2'')^2]^2}$$

$$- \frac{1}{16}\frac{(\varepsilon_2'')^3(\varepsilon_1)^6}{(\varepsilon_1)^3[(\varepsilon_2')^2 + \varepsilon_2'\varepsilon_1 + (\varepsilon_2'')^2]^3}i + \cdots \quad . \qquad \text{(A.4)}$$

By substituting Eqs. A.4 and A.3 into Eq. A.2, we can obtain

$$k_{sp}' = \frac{\omega}{c}\sqrt{\frac{\varepsilon_1[(\varepsilon_2')^2 + \varepsilon_2'\varepsilon_1 + (\varepsilon_2'')^2]}{(\varepsilon_2' + \varepsilon_1)^2 + (\varepsilon_2'')^2}}\left[1 + \frac{1}{8}\frac{(\varepsilon_2'')^2(\varepsilon_1)^4}{(\varepsilon_1)^2[(\varepsilon_2')^2 + \varepsilon_2'\varepsilon_1 + (\varepsilon_2'')^2]^2} + \cdots\right],$$

or

$$k_{sp}'' = \frac{\omega}{c}\sqrt{\frac{\varepsilon_1[(\varepsilon_2')^2 + \varepsilon_2'\varepsilon_1 + (\varepsilon_2'')^2]}{(\varepsilon_2' + \varepsilon_1)^2 + (\varepsilon_2'')^2}} \times$$

$$\left\{\frac{1}{2}\frac{\varepsilon_2^{''}(\varepsilon_1)^2}{\varepsilon_1[(\varepsilon_2^{'})^2+\varepsilon_2^{'}\varepsilon_1+(\varepsilon_2^{''})^2]}-\frac{1}{16}\frac{(\varepsilon_2^{''})^3(\varepsilon_1)^6}{(\varepsilon_1)^3[(\varepsilon_2^{'})^2+\varepsilon_2^{'}\varepsilon_1+(\varepsilon_2^{''})^2]^3}+\cdots\right\},$$

or

$$k_{sp}^{'}=\frac{\omega}{c}\sqrt{\frac{\varepsilon_1[(\varepsilon_2^{'})^2+\varepsilon_2^{'}\varepsilon_1+(\varepsilon_2^{''})^2]}{(\varepsilon_2^{'}+\varepsilon_1)^2+(\varepsilon_2^{''})^2}}\left[1+\frac{1}{8}\frac{(\varepsilon_2^{''})^2(\varepsilon_1)^2}{[(\varepsilon_2^{'})^2+\varepsilon_2^{'}\varepsilon_1+(\varepsilon_2^{''})^2]^2}+\cdots\right],$$

or

$$k_{sp}^{''}=\frac{\omega}{c}\sqrt{\frac{\varepsilon_1[(\varepsilon_2^{'})^2+\varepsilon_2^{'}\varepsilon_1+(\varepsilon_2^{''})^2]}{(\varepsilon_2^{'}+\varepsilon_1)^2+(\varepsilon_2^{''})^2}}\times$$

$$\left\{\frac{1}{2}\frac{\varepsilon_2^{''}\varepsilon_1}{[(\varepsilon_2^{'})^2+\varepsilon_2^{'}\varepsilon_1+(\varepsilon_2^{''})^2]}-\frac{1}{16}\frac{(\varepsilon_2^{''})^3(\varepsilon_1)^3}{[(\varepsilon_2^{'})^2+\varepsilon_2^{'}\varepsilon_1+(\varepsilon_2^{''})^2]^3}+\cdots\right\}.$$

Let us consider two extreme cases; if $|\varepsilon_2^{'}|>>|\varepsilon_2^{''}|$, then $k_{sp}^{'}$ and $k_{sp}^{''}$ are approximately equal

to

$$k_{sp}^{'}\approx\frac{\omega}{c}\sqrt{\frac{\varepsilon_1[(\varepsilon_2^{'})^2+\varepsilon_2^{'}\varepsilon_1]}{(\varepsilon_2^{'}+\varepsilon_1)^2}}\left[1+\frac{1}{8}\frac{(\varepsilon_2^{''})^2(\varepsilon_1)^2}{(\varepsilon_2^{'})^2[\varepsilon_2^{'}+\varepsilon_1]^2}+\cdots\right]$$

$$\approx\frac{\omega}{c}\sqrt{\frac{\varepsilon_1\varepsilon_2^{'}[\varepsilon_2^{'}+\varepsilon_1]}{(\varepsilon_2^{'}+\varepsilon_1)^2}}=\frac{\omega}{c}\sqrt{\frac{\varepsilon_1\varepsilon_2^{'}}{\varepsilon_2^{'}+\varepsilon_1}}$$

and

$$k_{sp}^{''}\approx\frac{\omega}{c}\sqrt{\frac{\varepsilon_1\varepsilon_2^{'}}{\varepsilon_2^{'}+\varepsilon_1}}\left\{\frac{1}{2}\frac{\varepsilon_2^{''}\varepsilon_1}{[(\varepsilon_2^{'})^2+\varepsilon_2^{'}\varepsilon_1]}-\frac{1}{16}\frac{(\varepsilon_2^{''})^3(\varepsilon_1)^3}{(\varepsilon_2^{'})^3[\varepsilon_2^{'}+\varepsilon_1]^3}+\cdots\right\}$$

$$\approx\frac{\omega}{c}\sqrt{\frac{\varepsilon_1\varepsilon_2^{'}}{\varepsilon_2^{'}+\varepsilon_1}}\left\{\frac{1}{2}\frac{\varepsilon_2^{''}\varepsilon_1}{\varepsilon_2^{'}(\varepsilon_2^{'}+\varepsilon_1)}\right\}=\frac{\omega}{c}\left[\frac{\varepsilon_1\varepsilon_2^{'}}{\varepsilon_2^{'}+\varepsilon_1}\right]^{\frac{3}{2}}\frac{\varepsilon_2^{''}}{2(\varepsilon_2^{'})^2},$$

or

$$\begin{cases} k'_{sp} \approx \dfrac{\omega}{c}\sqrt{\dfrac{\varepsilon_1 \varepsilon'_2}{\varepsilon'_2 + \varepsilon_1}} \\ k''_{sp} \approx \dfrac{\omega}{c}\left[\dfrac{\varepsilon_1 \varepsilon'_2}{\varepsilon'_2 + \varepsilon_1}\right]^{\frac{3}{2}} \dfrac{\varepsilon''_2}{2(\varepsilon'_2)^2} \end{cases} \quad . \qquad |\varepsilon'_2| >> |\varepsilon''_2| \qquad \text{(A.5)}$$

If $|\varepsilon'_2| << |\varepsilon''_2|$, then k'_{sp} and k''_{sp} are approximately equal to

$$k'_{sp} = \frac{\omega}{c}\sqrt{\frac{\varepsilon_1[(\varepsilon'_2)^2 + \varepsilon'_2\varepsilon_1 + (\varepsilon''_2)^2]}{(\varepsilon'_2 + \varepsilon_1)^2 + (\varepsilon''_2)^2}}\left[1 + \frac{1}{8}\frac{(\varepsilon''_2)^2(\varepsilon_1)^2}{(\varepsilon_1)^2[(\varepsilon'_2)^2 + \varepsilon'_2\varepsilon_1 + (\varepsilon''_2)^2]^2} + \cdots\right]$$

$$\approx \frac{\omega}{c}\sqrt{\frac{\varepsilon_1[\varepsilon'_2\varepsilon_1 + (\varepsilon''_2)^2]}{2\varepsilon'_2\varepsilon_1 + (\varepsilon_1)^2 + (\varepsilon''_2)^2}}\left[1 + \frac{1}{8}\frac{(\varepsilon''_2)^2(\varepsilon_1)^2}{[\varepsilon'_2\varepsilon_1 + (\varepsilon''_2)^2]^2} + \cdots\right]$$

$$\approx \frac{\omega}{c}\sqrt{\frac{\varepsilon_1(\varepsilon''_2)^2}{(\varepsilon_1)^2 + (\varepsilon''_2)^2}}\left[1 + \frac{1}{8}\frac{(\varepsilon_1)^2}{(\varepsilon''_2)^2} + \cdots\right] \approx \frac{\omega}{c}\sqrt{\frac{\varepsilon_1(\varepsilon''_2)^2}{(\varepsilon_1)^2 + (\varepsilon''_2)^2}} \; . \qquad \text{(A.6)}$$

Now calculate k''_{sp}

$$k''_{sp} = \frac{\omega}{c}\sqrt{\frac{\varepsilon_1[(\varepsilon'_2)^2 + \varepsilon'_2\varepsilon_1 + (\varepsilon''_2)^2]}{(\varepsilon'_2 + \varepsilon_1)^2 + (\varepsilon''_2)^2}} \times$$

$$\left\{\frac{1}{2}\frac{\varepsilon''_2\varepsilon_1}{[(\varepsilon'_2)^2 + \varepsilon'_2\varepsilon_1 + (\varepsilon''_2)^2]} - \frac{1}{16}\frac{(\varepsilon''_2)^3(\varepsilon_1)^3}{[(\varepsilon'_2)^2 + \varepsilon'_2\varepsilon_1 + (\varepsilon''_2)^2]^3} + \cdots\right\}$$

$$\approx \frac{\omega}{c}\sqrt{\frac{\varepsilon_1(\varepsilon''_2)^2}{(\varepsilon_1)^2 + 2\varepsilon_1\varepsilon'_2 + (\varepsilon''_2)^2}}\left\{\frac{1}{2}\frac{\varepsilon''_2\varepsilon_1}{[\varepsilon'_2\varepsilon_1 + (\varepsilon''_2)^2]} - \frac{1}{16}\frac{(\varepsilon''_2)^3(\varepsilon_1)^3}{[\varepsilon'_2\varepsilon_1 + (\varepsilon''_2)^2]^3} + \cdots\right\}$$

$$\approx \frac{\omega}{c}\sqrt{\frac{\varepsilon_1(\varepsilon''_2)^2}{(\varepsilon_1)^2 + (\varepsilon''_2)^2}}\left\{\frac{1}{2}\frac{\varepsilon_1}{\varepsilon''_2} - \frac{1}{16}\frac{(\varepsilon_1)^3}{(\varepsilon''_2)^3} + \cdots\right\} \approx \frac{\omega}{c}\sqrt{\frac{\varepsilon_1(\varepsilon''_2)^2}{(\varepsilon_1)^2 + (\varepsilon''_2)^2}} \times \frac{\varepsilon_1}{2\varepsilon''_2} \; ,$$

or

$$\begin{cases} k_{sp}^{'} \approx \dfrac{\omega}{c}\sqrt{\dfrac{\varepsilon_1(\varepsilon_2^{"})^2}{(\varepsilon_1)^2+(\varepsilon_2^{"})^2}} \\ k_{sp}^{"} \approx \dfrac{\omega}{c}\sqrt{\dfrac{\varepsilon_1(\varepsilon_2^{"})^2}{(\varepsilon_1)^2+(\varepsilon_2^{"})^2}} \times \dfrac{\varepsilon_1}{2\varepsilon_2^{"}} \end{cases} \cdot \left|\varepsilon_2^{'}\right| << \left|\varepsilon_2^{"}\right| \qquad \text{(A.7)}$$

A.2. Calculation of the Resonant Excitation Condition of Surface Plasmons with the Wavelengths of 632.8 nm, 532 nm, and 266 nm

In Chapter 3, the dielectric functions of a gold metal at the wavelengths 632.8 nm, 532 nm, and 266 nm were

$$\begin{cases} \varepsilon_{266} \approx -0.79 + 5.52i \\ \varepsilon_{532} \approx -7.3 + 2.04i \\ \varepsilon_{632} \approx -9.9 + 1.05i \end{cases} . \qquad \text{(A.8)}$$

Eq. A.8 shows that the absolute values of the real parts of the dielectric function of Au at 632.8 nm and 532 nm wavelengths are greater than the absolute values of the imaginary parts (632.8 nm and 532 nm); however, at 266 nm, the absolute value of the imaginary part is much greater than the absolute value of the real part. For 532 nm and 632.8 nm, the resonant conditions in the Kretschmann-Raether configuration are

$$\begin{cases} \dfrac{\omega}{c}\sqrt{\varepsilon_{prism}^{532}}\sin\theta_{sp} = \dfrac{\omega}{c}\sqrt{\dfrac{\varepsilon_{532}^{'}\varepsilon_a}{\varepsilon_{532}^{'}+\varepsilon_a}} \\ \dfrac{\omega}{c}\sqrt{\varepsilon_{prism}^{633}}\sin\theta_{sp} = \dfrac{\omega}{c}\sqrt{\dfrac{\varepsilon_{633}^{'}\varepsilon_a}{\varepsilon_{633}^{'}+\varepsilon_a}} \end{cases}$$

or

$$\begin{cases} \sin\theta_{sp}^{532} = \sqrt{\dfrac{\varepsilon_{532}^{'}\varepsilon_a}{(\varepsilon_{532}^{'}+\varepsilon_a)\varepsilon_{prism}^{532}}} = \sqrt{\dfrac{-7.3}{(-7.3+1)\times 1.45\times 1.45}} = 0.7424 \\ \sin\theta_{sp}^{633} = \sqrt{\dfrac{\varepsilon_{633}^{'}\varepsilon_a}{(\varepsilon_{633}^{'}+\varepsilon_a)\varepsilon_{prism}^{633}}} = \sqrt{\dfrac{-9.9}{(-9.9+1)\times 1.45\times 1.45}} = 0.7274 \end{cases}$$

or

$$\begin{cases} \theta_{sp}^{532} = 47.94^\circ > 43.6^\circ = \theta_{critical} \\ \theta_{sp}^{633} = 46.67^\circ > 43.6^\circ = \theta_{critical} \end{cases} . \quad (A.9)$$

APPENDIX B

SOURCE CODE FOR COMPUTING REFLECTANCE VERSUS INCIDENT ANGLE BY THREE-LAYER FRENSEL'S EQUATION

This program is to simulate the condition of the surface plasmon resonance for s- and p-polarized light by calculating the reflectance, R, to find the minimal value corresponding to SPR.

```
format long
% constants used in this calculation
c = 2.99792458e+8;  % speed of light
hbar = 6.5822e-16;  %plank constant
%%%%%%%%%%%%% Air %%%%%%%%%%%%%%%%%%%%%
epsilon2 = 1.0;                          %permittivity of air, real number
%%%%%%%%%% Gold at 266nm, 532 nm or 632.8 nm %%%%%%%%%
%epsilon1 = -6.29 + 2.042i; %wavelength = 532nm
%epsilon1 = -9.8567 + 1.03i; %wavelength = 632.8nm
epsilon1 = -0.7796 + 5.6686i; % wavelength = 266nm
%n = 1.63;
%k = 1.784;
%RePart = n^2 - k^2;
%ImPart = 2*n*k;
%epsilon1=RePart + ImPart*i; %-0.7925+5.5161i; %(0.1726+3.4218i)^2;
%permittivity of gold, complex number -0.7925+5.5161i;
```

```
%%%%%%%Fused silica at 266nm, 532 nm, or 632.8 nm %%%%%%%%%
npr = 1.49968;%1.723; %1.5;        %refractive index of fused silica at 266nm
%npr = 1.46071; % 532nm or 632 nm
%%%%%%%%%%%%%%%% Critical angle %%%%%%%%%%%%%%%%%%%
critical_angle = asin(1/npr)*180/pi;
%%%%%%%%%%%%%%%% SPR angle %%%%%%%%%%%%%%%%%%%%%%%
spr_angle = asin(sqrt((epsilon1*epsilon2)/(npr^2 * (epsilon1 + epsilon2))))*180/pi;
%%%%%%%%%%%%%%%% Gold thickness %%%%%%%%%%%%%%%%%%%
d1 = 20.0e-9;   %gold film thickness (meter)
fukso = 1.0i;     % unit of imaginary part
%%%%%%%%%% Incident waveform %%%%%%%%%%%%%%%%%%%%%%%
lamd = 266e-9; % the wavelength of the incident laser
omega = 2.0*pi*c/lamd; %angular frequency
%%%%%%%%%%%% Angle scan %%%%%%%%%%%%%%%%%%%%%%%%%%%
ang0=10.0; %starting angle
ang1=80.0; %ending angle
for index = 1:1001
   delta_theta = (index-1)*((ang1-ang0)/1000.0);
   theta_plot(index) = ang0 + delta_theta;
   theta = (ang0 + delta_theta)*pi/180.0; %rad
   rpr1 = ( (cos(theta)/npr) - ...
            (sqrt(epsilon1 - (npr^2) * sin(theta)*sin(theta))/epsilon1) )/...
            ( (cos(theta)/npr) + ...
```

```
        (sqrt(epsilon1 - (npr^2) * sin(theta)*sin(theta))/epsilon1) );
  r12 =  ( (sqrt(epsilon1- npr^2 * sin(theta)*sin(theta))/epsilon1) -...
        (sqrt(epsilon2- npr^2 * sin(theta)*sin(theta))/epsilon2) )/...
        ( (sqrt(epsilon1- npr^2 * sin(theta)*sin(theta))/epsilon1) +...
        (sqrt(epsilon2- npr^2 * sin(theta)*sin(theta))/epsilon2) );
  alpha = (2.0*omega/c)*d1*sqrt(epsilon1 - (npr^2)*sin(theta)*sin(theta))*fukso;
  rpr12 = (rpr1 + r12*exp(alpha))/(1.0 + rpr1*r12*exp(alpha));
  rpr12c = conj(rpr12);
  ref = rpr12*rpr12c;
  theta_vector(index) = theta;
  ref_vector(index) = ref;
end
plot(theta_vector*180/pi,ref_vector,'r')
hold on
 %The following progrma is to calculate the three-layer system reflectance
 %with s-polarized light by using the Fresenel's equation
 for index = 1:1001
  delta_theta = index-1)*((ang1-ang0)/1000.0);
  theta_plot(index) = ang0 + delta_theta;
  theta = (ang0 + delta_theta)*pi/180.0; %rad
  rpr1 = (cos(theta)*npr - ...
        (sqrt(epsilon1 - (npr^2) * sin(theta)*sin(theta))))/...
        (cos(theta)*npr + sqrt(epsilon1 - (npr^2) * sin(theta)*sin(theta)));
```

```
    r12 = ( (sqrt(epsilon1- npr^2 * sin(theta)*sin(theta))) -...
          (sqrt(epsilon2- npr^2 * sin(theta)*sin(theta))))/...
          ( (sqrt(epsilon1- npr^2 * sin(theta)*sin(theta))) +...
          (sqrt(epsilon2- npr^2 * sin(theta))));
    alpha = (2.0*omega/c)*d1*sqrt(epsilon1 - (npr^2)*sin(theta)*sin(theta))*fukso;
    rpr12 = (rpr1 + r12*exp(alpha))/(1.0 + rpr1*r12*exp(alpha));
    rpr12c = conj(rpr12);
    ref = rpr12*rpr12c;
    theta_vector(index)=theta;
    ref_vector(index)=ref;
end
plot(theta_vector*180/pi,ref_vector,'.b')
```